# Control of Optically Induced Currents in Semiconductor Crystals

## Dissertation

zur
Erlangung des Doktorgrades
der Naturwissenschaften
(Dr. rer. nat.)

dem
Fachbereich Physik
der Philipps-Universität Marburg

vorgelegt von
**Kapil Kumar Kohli**
aus
Stuttgart

Marburg/Lahn, 2010

Vom Fachbereich Physik der Philipps-Universität Marburg
als Dissertation angenommen am: 20.05.2010

Erstgutachter: PD Sangam Chatterjee, PhD
Zweitgutachter: Prof. Dr. M. Kira

Tag der mündlichen Prüfung: 01.06.2010

# Zusammenfassung

Die technologische Entwicklung der Terahertz (THz)-Spektroskopie hat sich in den letzten Jahren so stark beschleunigt, dass es vermessen ist, immer noch von der THz-Lücke zu reden. Vor dem weitverbreiteten Einsatz von Ultrakurzzeit-Lasern klaffte im elektromagnetischen Spektrum tatsächlich eine Lücke zwischen dem Gigahertz (GHz) und dem Petahertz (PHz) Band, das weder mit optischen noch mit elektronischen Verfahren zu erreichen war. Erst durch den Einsatz von breitbandigen Lasern mit genügend hoher Intensität gelang es, durch Differenzfrequenzmischung in Kristallen, Frequenzen im THz-Bereich zu erzeugen und zu nutzen [1]. Es gibt eine Vielzahl von Einsatzmöglichkeiten für THz-Strahlung. Neben den vielfältigen Einsatzmöglichkeiten in der Industrie als kontaktlose und zerstörungsfreie in-situ-Analysemethode ist ihre niedrige Photonenenergie auch für die Restauration von Kunstwerken [2] oder als bildgebendes Verfahren, z.B. im Sicherheitsbereich nützlich [3, 4]. Besonders der Einsatz in den sog. Nacktscannern hat in den letzten Monaten für erhitzte Diskussion in Politik und Öffentlichkeit gesorgt.

In dieser Arbeit geht es um wissenschaftliche Fragestellungen, und auch hier ist die Strahlung im THz-Band sehr gefragt. Ihre geringe Photonenenergie ermöglicht die Untersuchung von Wechselwirkungen innerhalb der Energiebänder von Halbleitern [5, 6]. Mit geeigneter Feldstärke kann dies auch zur direkten Einflussnahme auf die Form der Bänder ausgenutzt werden [7–9].

Von besonderem Interesse für diese Arbeit ist der Zusammenhang zwischen der THz-Emission aus ZnTe- und GaAs-Kristallen und den zugrundeliegenden Prozessen der optischen Gleichrichtung (optical rectification current), bzw. der Verschiebeströme (shift current). Die THz-Strahlung dient als empfindlicher Sensor. Die Ströme entstammen einer Divergenz des Suszeptibilitätstensors 2. Ordnung $\chi^{(2)}$ für den Grenzfall, dass die Differenzfrequenz $\omega_1 - \omega_2 = \omega_D$ gegen Null geht [10, 11]. Aus der theoretischen Behandlung können Gleichungen hergeleitet werden, die das Verhalten der Ströme aus der Form des anliegenden Feldes beschreiben (Gleichung (2.98) & (2.99)). Als Effekt der Suszeptibilität ist das Verhalten der

Ströme abhängig von der Pulseinhüllenden, infolgedessen muss auch die emittierte THz-Strahlung eine solche Abhängigkeit aufweisen.

Diese wird in der vorliegenden Arbeit auf zweierlei Art nachgewiesen. Zum einen wird die Periode des elektrischen Felds frequenzabhängig verlängert (verkürzt). Dies wird als „zwitschern“ (engl. „chirp“) bezeichnet. Für die zweite Methode wird ein phasenstabiler zweiter Puls eingeführt. In dieser Superposition der Felder wird sich die absolute Phase, die „carrier envelope phase“ (CEP) als der entscheidende Parameter erweisen.

In Abschnitt 2.2 sind die Vorzüge der Kohärenten Kontrolle als Experimentiertechnik dargestellt. Ausgangspunkt dieser Experimente ist die kohärente Überlagerung von elektromagnetischen Feldern. Dadurch ergibt sich ein neuer Freiheitsgrad, der einigen Einfluss auf die messbaren Größen hat; es lassen sich gezielt Prozesse messen und steuern, die sich hinter dem sichtbaren Signal verstecken. In der Variante der Optimalen Kontrolle wird das Verfahren auch verwendet, um experimentell den Hamilton-Operator eines quantenmechanischen Systems durch ausprobieren zu lösen. Als Einflussmöglichkeiten stehen eigentlich alle Parameter eines Laserpulses einzeln, oder in Kombination zur Verfügung, z.B. die Phase, die CEP, die Intensität, die Polarisation, die Form der Einhüllenden oder der zeitliche Abstand in Pulszügen. Das Ziel im ersten Teil der Arbeit ist die Entwicklung eines kohärenten Kontroll-Mechanismus der die relative CEP eines Pulspaares verwendet.

Die Experimente werden in einem THz-Emissions-Aufbau, dem ein Pulsformer vorgeschaltet ist, durchgeführt. Der Pulsformer ist in einer 4f-Transmissionsgeometrie verwirklicht. Im Zentrum sitzt eine Flüssigkristallmaske, die durch Anlegen von Phasenmasken sowohl die Amplitude, als auch die Phase des Laserpulses manipulieren kann, in diesen Experimenten wird jedoch nur die Phase verwendet. Eine Einführung zum Einfluss der Phase auf den Puls findet sich in Abschnitt 2.4. Entwickelt man den Phasenterm im Frequenzraum in eine Taylorreihe, beschreibt der erste Term die absolute Phase, die CEP. Sie beschreibt die Verschiebung zwischen dem Feldmaximum und dem Maximum der Einhüllenden. Bei 800 nm beträgt die Periode des optischen Zyklus 2,76 fs, d.h., die Verschiebung wird erst bei Pulslängen im Bereich unterhalb von 10 fs, wichtig. Für Pulslängen von 100 fs wie sie hier verwendet werden, kann die CEP vernachlässigt werden. Wird jedoch ein zweiter, phasenstabiler Puls eingebracht, ist es durch Variation der CEP möglich, die Form der Einhüllenden zu kontrollieren.

Dies ist z.B. in Abbildung 4.14 für Verschiebeströme in GaAs und einem Zeitabstand von $\tau = 60fs$ gezeigt. Das periodische Verhalten der THz-Emission ist

Zeugnis der erfolgreichen Kontrolle der Einhüllenden. Hierbei passiert Folgendes: Obwohl die Position von Feldmaximum und dem Maximum der Einhüllenden relativ zueinander unbekannt ist, kann durch die CEP das Feld des zweiten Pulses verschoben und dadurch die Superposition der Felder gezielt gestört werden. Gleichungen (2.98) & (2.99) zeigen, wie direkt der Einfluss auf die Ströme ist. Verschiebeströme folgen der Einhüllenden direkt, während Gleichrichtungsströme der Ableitung der Einhüllenden folgen.

Zusätzlich zum Experiment, dass für beide Stromsorten an ZnTe (Gleichrichtungsstrom) und GaAs (Verschiebestrom) und für zwei verschiedene Zeitpunkte ($\tau = 60fs$ & $\tau = 200fs$) mit zwei verschiedenen Masken (2-Farbenmaske & Rechteckige Phasenmaske) durchgeführt worden ist, wurde ein Modell entwickelt, das die Ergebnisse, im Besonderen das THz-Emissionsmuster bei Variation der CEP bestätigt (Abbildung 4.19). Ausgangspunkt des Modells ist die direkte Beschreibung der Ströme mit den Gleichungen (2.98) & (2.99) und wird in Abschnitt 3.3 detailliert beschrieben. Der Vorteil, die Experimente mit dem Modell zu beschreiben, ist die Möglichkeit, die Verteilung der Stromdichte direkt zu sehen, wie sie in Abbildung 4.20 gezeigt ist. Die THz-Emission dient hier als Sensor, um das Verhalten der Stromdichte zu visualisieren. Ein Blick auf ausgewählte Spuren der Stromdichte (Abbildung 4.21) liefert die Erklärung, woher diese prägnanten Muster stammen. Gut zu sehen ist, wie sich die Einhüllende abhängig von der CEP-Variation verändert.

Für die Messung der THz-Emission wird ein indirektes Verfahren, das sogenannte elektro-optische Abtasten (engl. electro-optical sampling: EOS) verwendet. Dieses Vorgehen ermöglicht es, direkt das elektromagnetische Feld zu messen. Problematisch hierbei ist die begrenzte Bandbreite des Detektionskristalls, die zu Artefakten in der THz-Spur führt. Um die theoretisch und experimentell ermittelten Spuren vergleichen zu können, wurde dies berücksichtigt (Abschnitt 3.3). Es stellt sich heraus, dass die oszillierenden Nachschwinger eine direkte Folge der Detektionsmethode sind. Durch das zweite Feld ist es durch Manipulation des THz-Spektrums möglich, die THz-Spur zu formen, insbesondere ist es möglich, die Nachschwinger zu dämpfen.

Dies ist Thema des zweiten Teils dieser Arbeit. Ziel ist es, eine selbstlernende Maschine zu bauen, die eigenständig THz-Spuren in eine definierte Form bringt. Kernelement dieses Experiments ist ein genetischer Algorithmus, der Test, Selektion und Weiterentwicklung der Phasenmaske steuert und überwacht (Abschnitt 3.4). Getestet wird dies durch Herstellung einer THz-Spur, die nur über einen Zyklus verfügt, den sog. single-cycle THz-Puls. Verwendet wird hierfür die 2-Farbenmaske.

Der wichtige Parameter ist wieder die CEP, der Zeitabstand dagegen ist hier nicht wichtig und beträgt für diesen Teil wenige Femtosekunden. Der genetische Algorithmus erzeugt innerhalb weniger Generationen die gewünschte Pulsform (Abbildung 5.3) und auch die nächste Variante, die aus zwei aufeinander folgenden single-cycle-Pulsen besteht (double-cycle) bereitet ihm keine großen Probleme (Abbildung 5.8). Hier werden insgesamt 4 Pulse benötigt, zwei jeweils für den THz-Puls und die anderen beiden zur Dämpfung der Oszillationen. Es sind zehn Parameter nötig, um diese Maske zu definieren, sechs davon werden durch den Algorithmus gesteuert (Abbildung 5.7).

Die durchgeführten Experimente bieten einige Anknüpfpunkte für weitere Arbeiten. Das nächste Ziel für die selbstlernende Maschine ist die Herstellung eines THz-Pulses der nur aus einem halben Zyklus, engl. half-cycle, besteht. Zu diesem Zweck ist es sinnvoll, das Modell mit dem evolutionären Algorithmus zu koppeln, um ein Gefühl für die Form der Einhüllenden zu bekommen.

Das Themenfeld der kohärenten Kontrolle wird durch die Möglichkeit der Polarisationsformung neue Impulse bekommen. Es ist zunächst geplant, das Experiment mit gekreuzter Polarisation zu wiederholen.

In einem aktuell noch laufenden Projekt werden mit der Amplitudenmaske zwei schmale Streifen von 1 nm FWHM und 4 nm Abstand ausgeschnitten. Anschließend wird einer der beiden Pulse mit der 2-Farbenmaske verzögert. Im aufgenommenen Bild ist eine Signatur in den ersten zehn Femtosekunden sichtbar. In der Theoriegruppe von John Sipe aus Toronto wird gerade versucht, dies zu modellieren, um die Prozesse dahinter zu verstehen.

Der große Traum bleibt aber, diesen Aufbau mit einem CEP-stabiliserten Lasersystem betreiben zu können. Die Verwendung einer Phasenmaske als CEP-Verschieber wurde zwar schon gezeigt, aber ich bin mir sicher, dass hier noch nicht das ganze Potential ausgeschöpft worden ist [12].

# Literatur

[1] M. Bass, P. A. Franken, J. F. Ward und G. Weinreich. “Optical Rectification”. Physical Review Letters **9**, 446–448 (1962). url: `http://dx.doi.org/10.1103/PhysRevLett.9.446`. S. S. i.

[2] K. Fukunaga, Y. Ogawa, S. Hayashi und I. Hosako. “Terahertz spectroscopy for art conservation”. IEICE Electronics Express **4**, 258–263 (2007). url: `http://dx.doi.org/10.1587/elex.4.258`. S. S. i.

[3] M. C. Kemp u. a. “Security applications of terahertz technology”. Hrsg. von R. J. Hwu und D. L. Woolard. Terahertz for Military and Security Applications **5070**, 44–52 (2003). url: `http://dx.doi.org/10.1117/12.500491`. S. S. i.

[4] A. Semenov, H. Richter, U. Böttger und H. W. Hübers. “Imaging terahertz radar for security applications”. Hrsg. von J. O. Jensen, H. L. Cui, D. L. Woolard und R. J. Hwu. Terahertz for Military and Security Applications VI **6949**, 694902+ (2008). url: `http://dx.doi.org/10.1117/12.778477`. S. S. i.

[5] R. Huber u. a. “How many-particle interactions develop after ultrafast excitation of an electron-hole plasma”. Nature **414**, 286–289 (2001). url: `http://dx.doi.org/10.1038/35104522`. S. S. i.

[6] R. Huber u. a. “Femtosecond Formation of Coupled Phonon-Plasmon Modes in InP: Ultrabroadband THz Experiment and Quantum Kinetic Theory”. Physical Review Letters **94**, 027401+ (2005). url: `http://dx.doi.org/10.1103/PhysRevLett.94.027401`. S. S. i.

[7] J. R. Danielson u. a. “Interaction of Strong Single-Cycle Terahertz Pulses with Semiconductor Quantum Wells”. Physical Review Letters **99**, 237401+ (2007). url: `http://dx.doi.org/10.1103/PhysRevLett.99.237401`. S. S. i.

[8] A. Sell, A. Leitenstorfer und R. Huber. “Phase-locked generation and field-resolved detection of widely tunable terahertz pulses with amplitudes exceeding 100 MV/cm”. Opt. Lett. **33**, 2767–2769 (2008). url: `http://dx.doi.org/10.1364/OL.33.002767`. S. S. i.

[9] G. Gunter u. a. “Sub-cycle switch-on of ultrastrong light-matter interaction”. Nature **458**, 178–181 (2009). url: `http://dx.doi.org/10.1038/nature07838`. S. S. i.

[10] J. E. Sipe und A. I. Shkrebtii. “Second-order optical response in semiconductors”. Physical Review B **61**, 5337+ (2000). url: `http://dx.doi.org/10.1103/PhysRevB.61.5337`. S. S. i.

[11] F. Nastos und J. E. Sipe. “Optical rectification and shift currents in GaAs and GaP response: Below and above the band gap”. Physical Review B **74**, 035201+ (2006). url: `http://dx.doi.org/10.1103/PhysRevB.74.035201`. S. S. i.

[12] M. Kakehata, H. Takada, Y. Kobayashi und K. Torizuka. “Generation of optical-field controlled high-intensity laser pulses”. Journal of Photochemistry and Photobiology A: Chemistry **182**, 220–224 (2006). url: `http://dx.doi.org/10.1016/j.jphotochem.2006.05.025`. S. S. iv.

# Contents

# List of Figures

# 1 Introduction

There used to be a gap in the electromagnetic spectrum situated right between the electrical GHz and the optical PHz regimes and it was a challenge to generate radiation in the THz regime, which could not be achieved neither by electronic nor optical means. But now, while surveying all the applications and uses that have been found for THz radiation it is time to conclude: The infamous THz gap is now essentially closed, the use of THz radiation widespread, even in industrial settings as push button boxes. Times are interesting!

The variety of useful applications that use these so called T-Rays is impressive. An uncomprehensive survey of the published implementations yielded these examples: They are useful for the detection of foreign objects in chocolate [1], used in polymer production lines [2–4], in the life-sciences [5–8], and for art conservation [9]. Next generation telecom applications benefit from the higher bandwidth available in this regime [10–14]. The unique THz fingerprint is used to identify illicit drugs [15] and explosives [16], which excites law enforcement agencies, especially when available in integrated designs that have a small footprint [17]. The security applications, in particular the body imaging proposals for air travel [18, 19] recently, catapulted the technology into the political focus. THz imaging [20] and the progression into tomography [21, 22] and computed tomography [23] are very active fields themselves.

The sources that drive these applications are just as diverse. The technology has made a big leap from the first demonstration of a THz time-domain setup with a lithium tantalate crystal [24, 25]. Amongst the most interesting sources are Quantum Cascade THz Lasers (QCL) [26], integrated devices [27, 28], and very strong THz sources [29]. These strong fields are particularly interesting, as they enable a direct field-dependent manipulation of the band structure and establish the THz radiation in the field of extremely-nonlinear optics [30, 31].

The experiments presented in this text return to the fundamentals of the THz generation process in crystals. The understanding of this process has come a long way from its first observation [32]. Several models accurately describe the generation of the radiation [33–35]. Recent contributions relate the THz emission to divergences in the susceptibility tensor [36, 37]. Effects based on the second order susceptibility depend strongly on the shape of the pulse envelope. This should therefore also hold for the THz emission.

Using shaped pulse envelopes has introduced a novel way to control and manipulate optical processes [38–42]. Full control is achieved when amplitude and phase of the pulse are directly manipulated. In addition to these traditional parameters the polarization was introduced as a new degree of freedom [43]. A suitable tool for these techniques is a pulse shaper setup that incorporates a liquid crystal mask [44, 45], in combination with a feedback-loop, which transforms the setup into a self-learning machine capable of quickly finding optimal pulse shapes.

This is the vantage point for the experiments that are described in the following chapters. The goal is to efficiently control the THz emission in a coherent-control scheme. In an additional step, arbitrary shaped THz waveforms shall be generated with the help of an evolutionary algorithm at the center of the feedback-loop.

In chapter 2, the susceptibility tensor is introduced and the influence of the crystal structure is discussed. This is followed by a short overview of the coherent-control paradigm and some of the associated experiments. A summarized derivation of the relation between the susceptibility tensor and the current density that lies at the center of attention follows. This section concludes with an overview of the relevant experiments that relate to the injection, shift and rectification currents. The chapter ends with a section on the phase and some of its properties.

In chapter 3 the experimental fundamentals are introduced. The THz time-domain and the pulse shaper setups are established, followed by a presentation of the straightforward model of the current density and the emitted THz radiation. The chapter concludes with an introduction to the concept of evolutionary algorithms.

The experimental results are split into two chapters. The influence of the pulse shape on the THz emission is described in chapter 4, while chapter 5 contains the efforts to produce arbitrarily shaped THz traces. First, the pulse shaping properties of chirped laser pulses are discussed. Second, our implementation of the coherent-control paradigm follows which makes use of the relative Carrier Envelope Phase (CEP) of a pulse pair. A comparison of experimental and modeled results as well as the derivation of a coherent-control equation are included. The shaped THz waveforms are demonstrated by generation of a single-cycle and a double-cycle THz pulse.

Finally, this thesis ends with concluding remarks in chapter 6.

# 2 Higher-Order Effects, Coherent-Control, and the Phase

The interaction between light and matter is described by Maxwell's equations. Here, the relationship between the electric field and the polarization of matter is codified and reveals an intricate dependence on the specific properties of the material. The first discriminating traits here are density and organization.

Compare the situation between air and solid-state materials. Light propagates quasi-undamped through air, as the molecules are not organized as an entity but chaotically and lack any long range interaction. In contrast, the arrangement of atoms in solid-state materials is very organized and invokes far reaching forces. The makeup of the structure itself influences the interaction and produces new, crystal dependent, effects like birefringence, or the generation of new wavelengths.

In this chapter the theoretical framework of the periodic order of the crystal atoms is specified. The main focus lies on the susceptibility tensor. It will be shown, that it's the second order nonlinearities of the susceptibility tensor which generate radiation in the THz region. Following that, the coherent control technique is introduced and some of the relevant experiments are discussed. A slight detour explaining the different kinds of currents that are controllable, rounds up the section. The next section details a theoretical approach to explain the generation of ultrafast currents. The final section concludes the chapter with the phase, the often neglected but very intriguing parameter of the laser pulse.

## 2.1 The Susceptibility Tensor

The interaction between light and matter is determined by the properties of the proportionality factor that connects the electric field and the polarization. This section first expands the polarization into a power series to highlight the second-order contributions. A microscopic definition of the susceptibility is introduced that highlights how the crystal structure affects its properties.

### 2.1.1 Higher-Order Effects

The origins of the electric and magnetic fields are given by the four partial differential equations that constitute Maxwell's equations [46]:

$$\nabla \cdot \mathbf{D} = \rho, \tag{2.1}$$

$$\nabla \cdot \mathbf{B} = 0, \tag{2.2}$$

$$\nabla \times \mathbf{E} = -\frac{\partial \mathbf{B}}{\partial t}, \tag{2.3}$$

$$\nabla \times \mathbf{H} = \frac{\partial \mathbf{D}}{\partial t} + \mathbf{J}. \tag{2.4}$$

They are presented here in their differential form for free charge and free current. They are also known under independent names, which are from the top:

- Coulomb's law relates the electric displacement field **D** to the total charge density $\varrho$. It states that the charge density is the source of the displacement.
- Gauss's law for magnetism states, that there are no magnetic charges that act as the source for magnetism.
- Faraday's law is the first of the two relations that connect the electric and magnetic fields. It states, that a change of the magnetic field induces a current in a neighboring conductor loop.
- Ampere's law is the second relation to connect the two fields. It relates the magnetizing field **H** to the electric displacement field **D** and the total current density **J**. It states, that an electrical current or a change of the displacement field induces a magnetic field.

They are evaluated here under the boundary conditions, that there are no free charges and no free currents in the space, i.e. $\rho = 0$ and $\mathbf{J} = 0$. Without magnetization in the material the magnetic field is given by $\mathbf{B} = \mu_0 \mathbf{H}$. The polarization **P** is introduced by the displacement field

$$\mathbf{D} = \varepsilon_0 \mathbf{E} + \mathbf{P}, \tag{2.5}$$

and is defined by

$$\mathbf{P}(t) = \varepsilon_0 \chi \mathbf{E}(t). \tag{2.6}$$

The proportionality factor $\chi$ between the polarization and the electric field is the optical susceptibility. The formal derivation of this relation is given in the next section. The free space permittivity is a constant given by $\varepsilon_0 = 8.854 \times 10^{-12}\, F/m$, in the SI unit system. It is set to unity in the Gaussian unit system, $\varepsilon_0 = 1$.

For low intensity applications, the polarization directly follows the electric field and equation (2.6) holds. For high optical intensities the relationship is expanded into a power series, here initially written for scalar quantities $P$ and $E$

$$P(t) = \varepsilon_0 \left[ \chi^{(1)} E(t) + \chi^{(2)} E^2(t) + \chi^{(3)} E^3(t) + \ldots \right]. \tag{2.7}$$

This description holds for the instantaneous reaction of the medium to the electric field under the assumption that it is lossless and without dispersion. In addition to the linear term, the nonlinear higher-order terms rouse interest.

Consider a 2-color electric field

$$E(t) = E_1(t)\, \mathrm{e}^{-\mathrm{i}\omega_1 t} + E_2(t)\, \mathrm{e}^{-\mathrm{i}\omega_2 t} + \text{c.c.}, \tag{2.8}$$

and the consequence this has on the second order polarization [47]

$$\begin{aligned}
P^{(2)}(t) = \varepsilon_0 \chi^{(2)} \Big[ & E_1 E_1^* + E_2 E_2^* && \text{(OR)} \\
& + E_1^2\, \mathrm{e}^{-2\mathrm{i}\omega_1 t} + E_2^2\, \mathrm{e}^{-2\mathrm{i}\omega_2 t} && \text{(SHG)} \\
& + 2E_1 E_2\, \mathrm{e}^{\mathrm{i}(\omega_1+\omega_2)t} + 2E_1^* E_2^*\, \mathrm{e}^{-\mathrm{i}(\omega_1+\omega_2)t} && \text{(SFG)} \\
& + 2E_1^* E_2\, \mathrm{e}^{\mathrm{i}(\omega_1-\omega_2)t} + 2E_1 E_2^*\, \mathrm{e}^{-\mathrm{i}(\omega_1-\omega_2)t} \Big]. && \text{(DFG)}
\end{aligned} \tag{2.9}$$

The resulting expression is sorted into four similar looking groups of terms. The first line is termed optical rectification (OR). Excitation with a continuous wave (CW) source builds up a static electric field which does not radiate. Use of a fast pulsed laser source forces an oscillation of the static electric field, which radiates.

The second line describes second harmonic generation (SHG). This is a process in which the crystal creates new frequencies at $2\omega$ thus doubling the input frequency, i.e., halving the wavelength of the output beam.

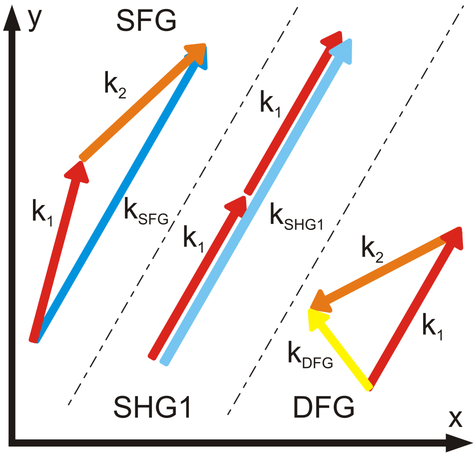

Figure 2.1: Visualization of the phase matching conditions for the frequency mixing processes. (From [48])

The third line is called sum-frequency generation (SFG) as the output beam emitts at the frequency $\omega = \omega_1 + \omega_2$. Difference-frequency generation (DFG) is a corresponding process that emits at $\omega = \omega_1 - \omega_2$, see line four.

All of these processes are routinely used, as they broaden the spectrum of the available spectroscopic frequencies. Widely used are the transformations into the UV, the NIR, or the IR, which are performed by mixing the signal beam with a conversion beam. SHG is especially useful as a pulse characteristic tool, as it inherently works with one color beams and is in fact used in autocorrelators. Additionally, a completely new regime opened up with the prevalence of ultrafast wideband pulsed laser sources. Using the DFG or the OR process and laser pulses with a spectral Full Width at Half Maximum (FWHM) of just 10 nm creates frequencies in the THz regime. These two nonlinear processes and the related effects are the main topic of this thesis.

One question remains. How to select the main radiating process? Each of these processes has a different relationship between the wavevectors **k**. This is set in the experiment by selecting the appropriate crystal orientation and input polarization of the laser pulse and is called phase matching, see Fig. 2.1. This organizes all the little radiation centers in the crystals into a single wavefront.

### 2.1.2 Formal Derivation

In the previous section, the susceptibility tensor appears out of thin air as a proportionality factor between the electric field and the polarization. This section will delve into the relationship and give a more detailed derivation.

In a three dimensional (3D) bulk structure, the crystal is composed of the crystal back-bone consisting of the ionized atoms, and a loosely bound electron. The atom loses it to the crystal due to the forces exerted through the long range organization. The electron is not completely free, but bound by harmonic forces in the harmonic oscillator model [49]. Depending on the energy of the excitation light, it will either free the electrons or lead to a microscopic field-driven movement. The combined movement per unit volume $V$ is called the polarization of the medium and is defined by

$$P = n_0 e x = n_0 d, \tag{2.10}$$

with the mean electron density per unit volume $n_0$ and the electron charge $e = 1.602 \times 10^{-19}\,C$. The displacement is labeled $x$ and is described by a driven Newtonian equation of motion

$$m_0 \frac{\mathrm{d}^2 x}{\mathrm{d}t^2} = -2 m_0 \gamma \frac{\mathrm{d}x}{\mathrm{d}t} - m_0 \omega_0^2 x + e\mathcal{E}(t), \tag{2.11}$$

with a monochromatic external field $\mathcal{E}(t) = \mathcal{E}(\omega)\,\mathrm{e}^{-\mathrm{i}\omega t}$ parallel to $x$. The mass of an electron is $m_0$. The sluggish movement of the ensemble is included in the damping factor $\gamma$ with a resonance frequency of $\omega_0$.

The differential equation is solved by the ansatz

$$x(t) = x(\omega) e^{-\mathrm{i}\omega t}, \tag{2.12}$$

and leads to

$$-e\mathcal{E}(\omega) = m_0 \left(\omega^2 + \mathrm{i}2\gamma\omega - \omega_0^2\right) x(\omega), \tag{2.13}$$

$$x(\omega) = -\frac{e\mathcal{E}(\omega)}{m_0 \left(\omega^2 + \mathrm{i}2\gamma\omega - \omega_0^2\right)}. \tag{2.14}$$

This is inserted back into equation (2.10) and yields the connection between the electric field and the polarization:

$$P(\omega) = -\frac{n_0 e^2}{m_0} \frac{1}{\omega^2 + \mathrm{i}2\gamma\omega - \omega_0^2} \mathcal{E}(\omega). \tag{2.15}$$

The susceptibility was introduced as the proportionality factor it is then expressed by

$$\chi(\omega) = -\frac{n_0 e^2}{2 m_0 \omega_0'} \left( \frac{1}{\omega - \omega_0' + \mathrm{i}\gamma} - \frac{1}{\omega + \omega_0' + \mathrm{i}\gamma} \right). \tag{2.16}$$

The denominator is given in the factorized version, which becomes possible through the introduction of the new resonance frequency $\omega_0'$ according to

$$\omega_0' = \sqrt{\omega_0^2 - \gamma^2}. \tag{2.17}$$

This approach incorporates the frequency shift due to the damping of the electron movement. The striking property of the optical susceptibility is the apparent divergence for

$$\omega = -\mathrm{i}\gamma \pm \omega_0'. \tag{2.18}$$

It is insignificant for values $\omega$ far away from $\omega_0'$. The second observation is that $\omega$ is a complex number, and not a scalar quantity. It is a tensor that couples the polarization to the electrical field.

Generally, the polarization is calculated in the time-domain by evaluation of the integral

$$P(t) = \int_{-\infty}^{\infty} \mathrm{d}t\, \chi(t) \mathcal{E}(t), \tag{2.19}$$

where the system response is collected in $\chi(t)$. But the polarization only depends on past events, which leads to the simplification

$$P(t) = \int_{0}^{\infty} \mathrm{d}\tau\, \chi(\tau) \mathcal{E}(t - \tau). \tag{2.20}$$

The history of the system is incorporated into the new time argument

$$\tau = t - t', \tag{2.21}$$

with $t > t'$. The state of the polarization is then only dependent on the time difference between excitation and probing.

In the frequency-domain, the polarization is reduced to a simple multiplication due to the convolution theorem

$$P(\omega) = \chi(\omega)\mathcal{E}(\omega), \tag{2.22}$$

with

$$\chi(\omega) = \int_0^\infty \mathrm{d}\tau\, \chi(\tau)\, \mathrm{e}^{\mathrm{i}\omega\tau}. \tag{2.23}$$

The optical susceptibility is a central concept for a few optical coefficients [49]. Take for example the displacement field $D(\omega)$:

$$\begin{aligned} D(\omega) &= \varepsilon_0\, \mathcal{E}(\omega) + P(\omega) \\ &= \varepsilon_0 \left[1 + \chi(\omega)\right] \mathcal{E}(\omega) \\ &= \varepsilon_0 \varepsilon(\omega) \mathcal{E}(\omega). \end{aligned} \tag{2.24}$$

This defines the optical susceptibility through

$$\varepsilon(\omega) = 1 + \chi(\omega). \tag{2.25}$$

Inserting the complex susceptibility tensor from above and splitting it into its real and imaginary terms

$$\varepsilon(\omega) = \varepsilon'(\omega) + \mathrm{i}\varepsilon''(\omega), \tag{2.26}$$

leads to expressions that describe the index of refraction $n(\omega)$ and the absorption coefficient $\alpha(\omega)$:

$$n(\omega) \simeq \sqrt{\varepsilon'(\omega)}, \tag{2.27}$$

$$\alpha(\omega) \simeq \varepsilon''(\omega). \tag{2.28}$$

Expressed here in the limit $|\varepsilon''(\omega)| << |\varepsilon'(\omega)|$, which is reasonable for semiconductors.

### 2.1.3 Crystal Symmetries

For a full description of the optical processes in a crystal the vector character of the electric field must be considered. It can be written as a sum

$$\mathbf{E}(\mathbf{r},t)=\sum_n \mathbf{E}(\omega_n)\,\mathrm{e}^{-\mathrm{i}\omega_n t}. \tag{2.29}$$

Accordingly, the polarization is given by

$$\mathbf{P}(\mathbf{r},t)=\sum_n \mathbf{P}(\omega_n)\,\mathrm{e}^{-\mathrm{i}\omega_n t}. \tag{2.30}$$

Here, the $\omega_n$ are a discrete number of frequency components. This turns the second-order nonlinear polarization into

$$P_i(\omega_n+\omega_m)=\varepsilon_0\sum_{jk}\sum_{(nm)}\chi^{(2)}_{ijk}(\omega_n+\omega_m;\omega_n,\omega_m)E_j(\omega_n)E_k(\omega_m). \tag{2.31}$$

In this expression the susceptibility is a tensor. The indices of $\chi^{(2)}_{ijk}$ encode the Cartesian coordinates. The $\omega_{n,m}$ denote the frequency components under consideration. The first variable of $\chi$ indicates the relation under which the $\omega_{n,m}$ are to be examined, it usually is $(\omega_n+\omega_m)$. The sum of equation (2.31) is evaluated for the variations of the $\omega_{n,m}$ that keep $(\omega_n+\omega_m=\text{const})$.

Counting the amount of numbers required to describe the full second order susceptibility tensor for the interaction of the 3 waves reveals: $3! = 6$ possible permutations of the $\omega$. This doubles to 12, as the substitution $\omega \rightarrow -\omega$ must be considered. Additionally, the indices $(ijk)$ are independent and can take on any value of $(xyz)$ creating $3^3 = 27$ combinations. The total amount of required numbers is given by the multiplication of these numbers and yields 324 complex numbers, for a totally nonsymmetric crystal. The complexity can be reduced to manageable numbers through exploitation of the crystal symmetries:

- **Fields are measurable quantities:** To be measurable, physical quantities must be real. As such, the susceptibility as a proportionality factor between two real fields cannot be complex. This yields

  $$\chi^{(2)}_{ijk}(-\omega_n-\omega_m;-\omega_n,-\omega_m)=\chi^{(2)*}_{ijk}(\omega_n+\omega_m;\omega_n,\omega_m). \tag{2.32}$$

- **Intrinsic symmetry:** The order of the electric fields in the derivation is arbitrary, so the interchange of the last two frequency arguments and

Cartesian indices will not change the optical susceptibility

$$\chi^{(2)}_{ijk}(\omega_n+\omega_m;\omega_n,\omega_m)=\chi^{(2)}_{ikj}(\omega_n+\omega_m;\omega_m,\omega_n). \tag{2.33}$$

- **Lossless media:** Loss-processes are usually included in the imaginary parts of an expression. In lossless media, the susceptibility is a real quantity. This enables the free interchange of the frequency arguments together with the corresponding Cartesian indices

  $$\chi^{(2)}_{ijk}(\omega_3;\omega_1,\omega_2)=\chi^{(2)}_{kji}(-\omega_2;\omega_1,-\omega_3). \tag{2.34}$$

  As a convention, the sign is inverted when the semicolon is crossed.

- **Kleinman’s symmetry:** If the medium is not only lossless but also possesses a negligible dispersion, the optical susceptibility will not depend on the frequency far away from its resonance frequency. This further softens the full permutation symmetry as the $(ijk)$ are now permutable without requiring a change of the frequency components

  $$\chi^{(2)}_{ijk}(\omega_3;\omega_1,\omega_2)=\chi^{(2)}_{kji}(\omega_3;\omega_1,\omega_2). \tag{2.35}$$

  This leads to a second simplification. The polarization can now be rewritten according to

  $$P_i(\omega_n+\omega_m)=\varepsilon_0\sum_{jk}\sum_{(nm)}2d_{ijk}E_j(\omega_n)E_k(\omega_m), \tag{2.36}$$

  with the new tensor

  $$d_{ijk}=\frac{1}{2}\chi^{(2)}_{ijk}. \tag{2.37}$$

  This leads to the contracted matrix $d_{il}$ that accounts for the symmetry of the last two indices

  | jk: | 11 | 22 | 33 | 23,32 | 31,13 | 12,21 |
  |---|---|---|---|---|---|---|
  | l: | 1 | 2 | 3 | 4 | 5 | 6 |

  This approach is particularly handy for considering crystal symmetries.

- **Crystal symmetries:** Group theory has identified seven unique crystal systems with 32 crystal classes where the cubic and isotropic materials are unsuitable for higher-order effects, as they are isotropic in their linear optical properties. Equally unsuitable for second-order effects are crystals with inversion symmetries, as the susceptibility vanishes identically. This is quickly demonstrated with a look at the second-order nonlinear polarization

$$P(t) = \varepsilon_0 \chi^{(2)} E^2(t), \tag{2.38}$$

with the field

$$E(t) = \mathcal{E} \cos \omega t. \tag{2.39}$$

A change of the sign of $E(t)$ causes a change in $P(t)$ because of inversion symmetry

$$E(t) \rightarrow -E(t) \tag{2.40}$$

$$P(t) \rightarrow -P(t) \tag{2.41}$$

$$\chi^{(2)} \rightarrow \chi^{(2)}. \tag{2.42}$$

This leads to

$$-P(t) = \varepsilon_0 \chi^{(2)} \Big[ -E(t) \Big]^2 \tag{2.43}$$

$$-P(t) = P(t), \tag{2.44}$$

which is only true for

$$\chi^{(2)} = 0. \tag{2.45}$$

Therefore crystals with anisotropies in their linear properties are very promising, as they exhibit birefringence.

These simplifications reduce the number of relevant components to manageable numbers. Considering the real field symmetry discards half of them, half of which are dismissed due to the intrinsic permutation symmetry, leaving 81 independent components. In lossless media full permutation symmetry reduces the number to 27 which are further decimated by consideration of the Kleinman symmetry and the contracted notation. The remaining ten independent components depend on the properties of the crystal structure. GaAs crystallizes in the zincblende structure which belongs to the crystal point group $\overline{4}3m$. The nonvanishing tensor elements are $xyz = xzy = yzx = yxz = zxy = zyx$. It has an unusually large second-order nonlinear susceptibility of $d_{36} = 370\,pm/V$ [47].

## 2.2 The Coherent-Control Paradigm

In the coherent-control paradigm an experiment is governed by the polarization of two pulses and their relative phase. The addition of the second pulse invokes the superposition principle of two electric fields, which provides new variables that are inherently linked to processes of the higher-order susceptibility. Examination of the current injection process reveals control over these selected properties [50]:

- **Direction of current:** A change of the polarization of the laser pulse, i.e., from left handed to right handed circularly polarized light reverses the direction of the current.
- **Magnitude of the current:** The relative phase between the two pulses controls the magnitude of the current.
- **Carrier velocity:** Carriers injected by coherent control mechanisms are not accelerated. They suddenly appear and possess high velocities. The crystal lattice supplies the momentum while the energy is provided by the electromagnetic field; momentum and energy conservation laws therefore are not violated. The velocity reaches several hundreds of km/s and is merely dependent on the amount of surplus energy that is added to the band gap energy of the material. This is set by the wavelength of the laser pulse.
- **Injection rate:** The irradiance of the light source is directly proportional to the amount of injected carriers.

This amount of control is difficult to achieve with traditional spectroscopic setups, where current injection involves several steps and does not produce these high velocities. First, carriers are generated by excitation with a laser pulse. Second, an external bias voltage is applied to avoid the isotropic evolution of the carrier distribution and guides the carriers into the desired direction for an effective current. This is either done through engineering of the crystal structure or by affixing electrodes onto the sample and applying a voltage. The time necessary to accelerate the carriers and the associated switch-on time is in the range of picoseconds. It is quasi-instantaneous for coherently-controlled currents, where it is only dependent on the pulse rise time. This opens up the possibility to use this process in optical switches.

The attraction of this technique is tainted by the additional experimental complexity required to keep the two fields and their relative phases stable. It is usually executed by incorporating a feedback loop into the setup.

### 2.2.1 Link to the Optical Susceptibility

The coherent-control paradigm is closely linked to the famous double slit experiment by Young [50]. The interference pattern emerges because the initial and final states are connected through several independent pathways. The full solution is thereby given by the superposition of the independent solutions.

The injection of ultrafast currents also known as QUantum Interference Currents (QUIC) is linked to the nonlinear $\chi_3$ process. It draws on the same principle as the slit experiment. The initial state in this case is an electron in the valence band that is transported to the conduction band, the final state. The two independent pathways are introduced through two phase stable laser pulses with different colors. The energy of the $2\omega$ beam directly transports the electron to the conduction band. Electrons excited by the $\omega$ beam can only reach the final state if a second $\omega$ photon is available at the right time to lift it from the virtual state in between the bands to the conduction band. The current is injected only through the interference term, as proven by theoretical considerations in [50]. It is controlled by the relative phase between the pulses. QUIC currents generally are $\chi_3$ processes and thus independent of the crystal structure in contrast to $\chi_2$ processes. This is exploited to inject currents into a variety of semiconductors, even into indirect bandgap materials [51, 52].

Calculations based on Fermi's golden rule [50, 53] generate expressions for the current injection rate for two-color and single-beam polarization control schemes. The current density is given by

$$\frac{\mathrm{d}J^a}{\mathrm{d}t} = \eta_3^{abc}(2\omega)E^b(-\omega)E^c(-\omega)E^d(2\omega) + c.c.\,. \tag{2.46}$$

This describes how the current density is controlled by the relative phase of the two beams in the two-color scheme

$$\frac{\mathrm{d}J^x}{\mathrm{d}t} = 2\mathrm{Im}\left(\eta_3^{xxxx}(2\omega)\right)\left|E^x(-\omega)\right|\left|E^x(\omega)\right|\left|E^x(2\omega)\right|\sin(\phi_{2\omega} - 2\phi_\omega). \tag{2.47}$$

Here, the beams are all identically polarized.

The single-color scheme is linked to the nonlinear $\eta_2$ process and therefore exists only in a selection of crystal geometries. Here, the polarization components of a single beam are used to control the current. The expression for the current density is

$$\frac{\mathrm{d}J^a}{\mathrm{d}t} = \eta_2(\omega)E^b(\omega)E^c(-\omega) + c.c., \tag{2.48}$$

which yields the coherent control equation

$$\frac{\mathrm{d}J^x}{\mathrm{d}t} = 2\mathrm{Im}\left(\eta_2^{xxz}(2\omega)\right)\left|E^x(-\omega)\right|\left|E^z(\omega)\right|\sin(\phi^x - \phi^z) + c.c.. \tag{2.49}$$

The current density is at maximum for a circularly polarized beam.

So far, scattering processes were ignored. This can be amended by introducing an additional term to the expressions (2.46) & (2.48) for the current density

$$-\frac{J^a_{\mathrm{e,h}}}{\tau_{\mathrm{e,h}}}. \tag{2.50}$$

This accounts for the scattering-induced momentum relaxation that reduces the current density. It is usually assumed, that the electron contribution dominates over the holes, so the holes are dropped from consideration. Though for the most part, scattering is neglected.

The following sections give a concise survey over the available current processes. Selecting the polarization of the excitation pulses, produces spin-unpolarized charge currents, spin-polarized currents or pure spin currents. Almost all of the presented experiments were performed on bulk GaAs, emphasizing once again, that these coherently-controlled currents do not require specially engineered crystals or different setups. Only experiments using a single-color scheme switch to the wurtzite crystal structure, as the second order nonlinearity $\eta_2$ does not exist in bulk GaAs.

### 2.2.2 Spin-Unpolarized Charge Currents

The case of parallel co-linearly polarized beams as shown in Figure 2.2 is discussed first. Here, the injection of currents in the plane of GaAs/(AlGa)As quantum wells is shown [54]. Experiments on bulk GaAs are presented in [55, 56].

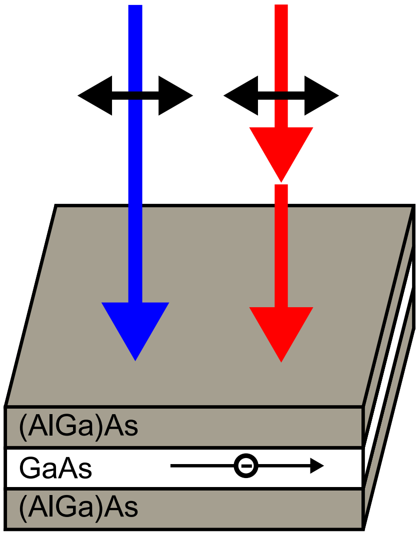

Figure 2.2: Configuration of the polarization for spin-unpolarized charge currents. (According to [54])

They all confirm the theoretical predictions from [50, 53] and show that the direction of the current as well as its sign and magnitude are coherently-controlled by the superposition of a two-color electric field.

The experimental work in [54] includes temporal and spatial information about the carrier movement. The pump-probe setup uses a Michelson interferometer

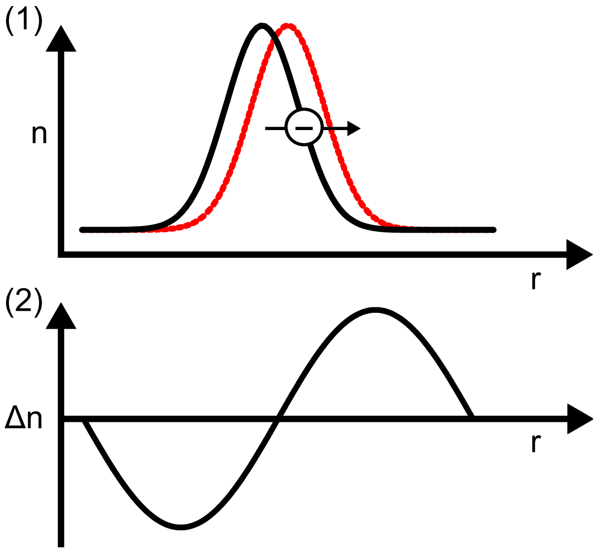

Figure 2.3: Spatial profile of the electron density $n$ and its expected movement, from the initial position (solid back line) to the final position (dashed red line) (1). Resultant change in electron density $\Delta n$ (2). (According to [54])

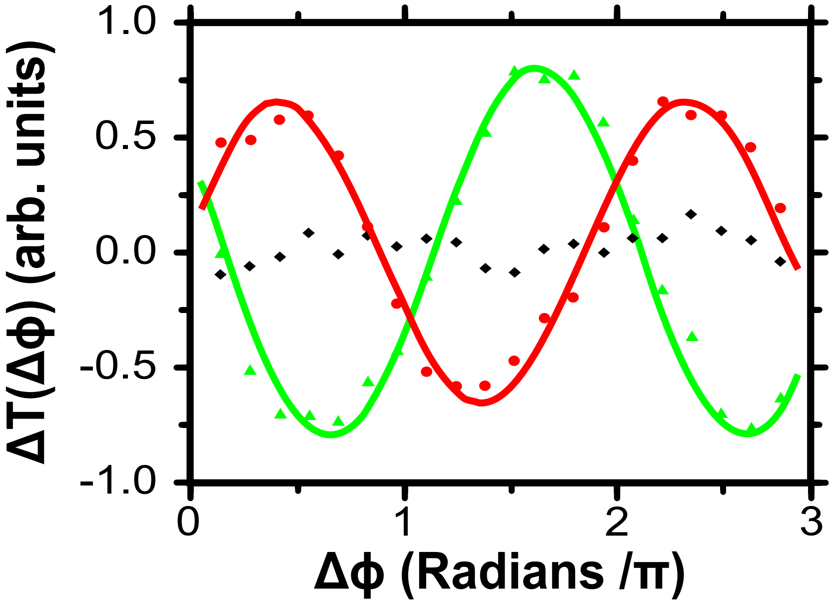

Figure 2.4: Differential transmission curves for the three probe positions $r = \pm 7.5\,\mu$m ((+) red dots and (-) green triangles) and $r = 0\,\mu$m (black diamonds). The phase dependence is clearly visible. The solid lines are sinusoidal fits to the data. (According to [54])

to split the two colors and control their relative phase. A linearly polarized probe beam is used to measure the differential transmission. Spatial information is gathered, by monitoring the movement of the Gaussian electron distribution of the injected ballistic carriers, see Fig. 2.3. This shapes the electron distribution depending on the $\Delta n(r)$ that approximates the spatial derivative of the original Gaussian profile $\partial n/\partial r$, if the movement is small.

The experiment was performed at $T = 80\,K$, an excess energy of $\sim 200\,meV$ and a carrier density of $\sim 1.6 \times 10^{17}/cm^3$. The expected shift of the electron distribution is only on the order of a few nm.

Fig. 2.4 reveals the phase dependence of the differential transmission for three different probe positions. The first is at the excitation spot, and the other two are set $\pm 7.5\,\mu$m apart from the excitation spot. The phase dependence manifests itself by the number of carriers moving in a given direction and the effect this has on the transmission of the probe light. At the probe position $r = 0$ the same number of carriers will move in the $\pm r$ directions and no phase dependence is observed. At $r = 7.5\,\mu$m ((+) red dots, (-) green triangles) the influence of the amount of carriers is apparent and is regulated by setting the relative phase, for $\Delta\phi \simeq \pi/2$ the carrier density increases in the $+\mathbf{r}$ direction which implies a movement in the same direction. The situation is reversed for $\Delta\phi \simeq 3/2\pi$. The behavior at $r = -7.5\,\mu\text{m}$ is exactly the same but phase shifted by $\pi/2$.

### 2.2.3 Spin-Polarized Currents

Spin-based electronic devices promise a slew of improvements over charge-based devices. They range from lower energy-requirements, over smaller structure sizes to faster switching times. Besides the electronic injection of spins as demonstrated in [57, 58] the all optical approach is very promising. It bridges the gap between the optical and the spin-based computational realms. Injection currents are uniquely suitable for this due to their independence of the crystal structure. To control the direction and magnitude of the spin and the, sometimes, accompanying electrical current, it is sufficient to control the optical polarization and the relative phase between the $\omega$ and $2\omega$ fields.

The optical selection rules state that, in general, excitation with circularly polarized light directly invokes the spin states and produces a carrier population with a net spin [59]. Analogous to the spin-unpolarized current case, this creates a symmetric distribution of spins in **k** space, and does not yet yield a net current, without an additional external bias.

Here, the superposition of the $\omega$ and $2\omega$ fields connects the valence and conduction bands through one- and two-photon absorption processes. This quantum interference generates a ballistic electrical current that is asymmetric in **k**-space.

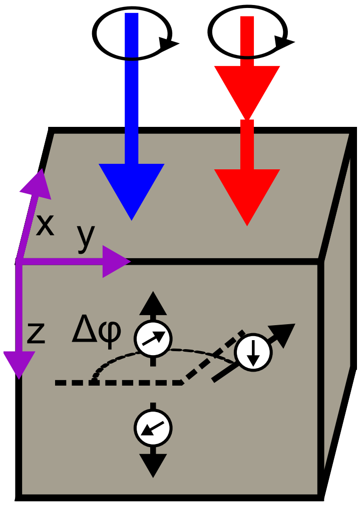

Figure 2.5: Configuration of the polarization for spin-polarized charge currents. (According to [60])

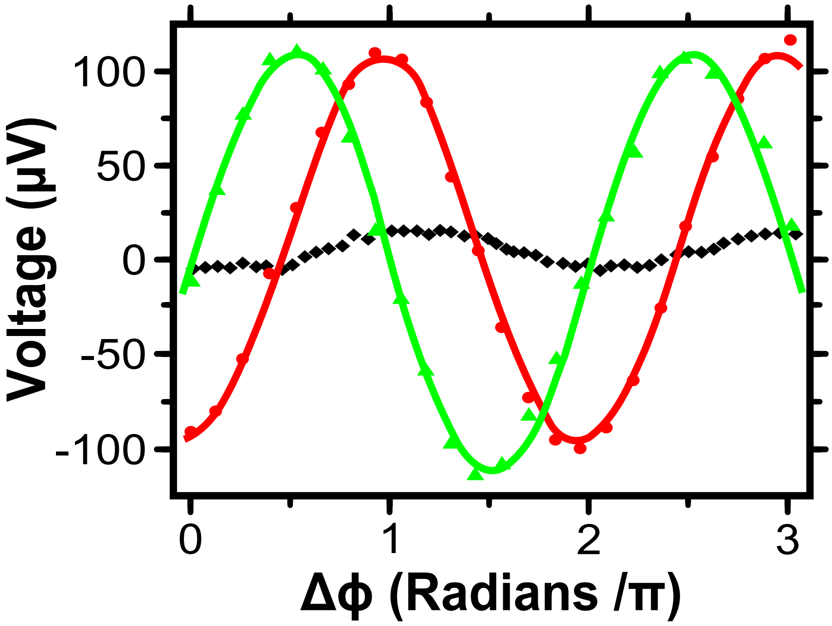

Figure 2.6: Phase dependence of the electric current for excitation with the same circular polarization for two different directions: $x$ (green triangles) and $y$ (red dots). For oppositely oriented polarizations the currents cancel each other out (black diamonds). Data is only shown for the $x$-direction. The lines represent sinusoidal fits. (According to [60])

The relative phase steers the constructive interference for one direction in **k**-space, while creating a destructive interference in the other direction.

The theoretical work in [61] and [62] present expressions for the electrical and spin currents, that are the result of the interference between the one and two-photon absorption. The interference terms are structured according to

$$\frac{\mathrm{d}\,\langle J^a\rangle_\mathrm{I}}{\mathrm{d}t} = \eta_\mathrm{I}^{acdf}(\omega)\,E^{c*}(\omega)E^{d*}(\omega)E^f(2\omega) + \text{c.c.}\,, \tag{2.51}$$

$$\frac{\mathrm{d}\,\langle K^{ab}\rangle_\mathrm{I}}{\mathrm{d}t} = \mu_\mathrm{I}^{abcdf}(\omega)\,E^{c*}(\omega)E^{d*}(\omega)E^f(2\omega) + \text{c.c.}\,. \tag{2.52}$$

The fourth rank tensor $\eta_\mathrm{I}^{acdf}(\omega)$ describes the electrical current and is purely imaginary, while the purely real fifth rank tensor $\mu_\mathrm{I}^{abcdf}(\omega)$ describes the spin currents. Predictions include a current with a phase dependent direction when using circularly polarized light as shown in Fig. 2.5. This was demonstrated in [60] and is reproduced as Fig. 2.6. The setup used here actually predates that of [54] and follows the same experimental idea.

Data for two different probe positions, one in the $x$-direction (green triangles), the other in the $y$-direction (red dots) are shown. The solid lines are sinusoidal fits to the data. This proves, that the direction of the current is accessible through the relative phase, while the total amount of carriers in a given direction stays constant. For oppositely oriented circularly polarized light, an equal number of carriers is generated in opposing directions, thus producing no net current flow in the $x$-direction (black squares).

Spin polarization as defined by the ratio of the spins produced by left ($\sigma^-$) or right ($\sigma^+$) circularly-polarized light

$$P = \frac{\sigma^- - \sigma^+}{\sigma^- + \sigma^+}, \tag{2.53}$$

was not directly confirmed, but inferred through the use of the circular polarization. The optical selection rules reveal that in the present configuration transitions from the light hole (lh) and heavy hole (hh) valence bands to the conduction band create spins of opposite orientation. Further, in bulk GaAs the hh transitions are three times stronger than the lh transitions which leads to a spin-polarized carrier population of 50%. This is further reduced if the transition from the split-off to the conduction band is excited. Spin polarizations of 100% are possible, if the degeneration of the hh and lh valence bands is removed and only transitions from the hh band are initiated. A detailed theoretical description of this process in quantum wells for all the relevant configurations is given in [62]. It turns out, that in quantum wells with 2% biaxial compressive strain, 100% spin-polarized currents with high swarm velocities are attainable.

### 2.2.4 Pure Spin Currents

Pure spin currents are created by using two orthogonally polarized beams, as shown in Fig. 2.7. The large black arrows indicate the direction of the current. The number of carriers in each direction is the same, hence there is no net current. The small arrows in the spheres mark the net electron spin polarization. Through filtering of the spin orientation a pure spin current becomes discernible.

A cosine dependence of the spin current on the relative phase between the $\omega$ and $2\omega$ field was predicted [61] and almost simultaneously verified by two independent experiments, using similar approaches in cubic ZnTe and GaAs/(AlGa)As quantum wells [63, 64].

The fundamental idea of the two approaches is the same. The initial carrier distribution has an equal amount of spins pointing in the two spin directions. As

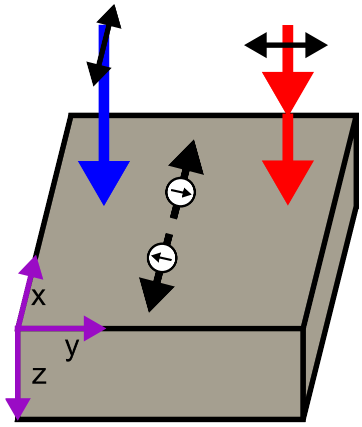

Figure 2.7: Configuration of the polarization for pure spin currents. (According to [64])

they are ballistic carriers, the spin-down and spin-up distributions will move in different directions before randomization of the momentum sets in, as shown in Fig. 2.8.

The shift which is expected to be in the order of tens of nm proves the existence of the pure spin current. The shift is determined through a spatially-resolved pump-probe setup by using a tightly focused probe beam that is circularly polarized [64]. The interaction with the spin currents changes the transmission of the probe

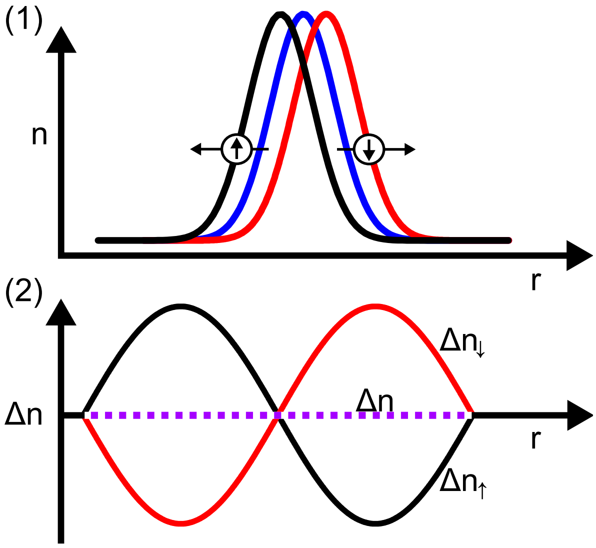

Figure 2.8: Spatial profile of the initial electron density *n* (blue line) and the expected movement of the spin-down (red line) and spin-up (black line) electrons (1). Change of the spin-up (black line), spin-down (red line) and total electron density (violet line) (2). (According to [64])

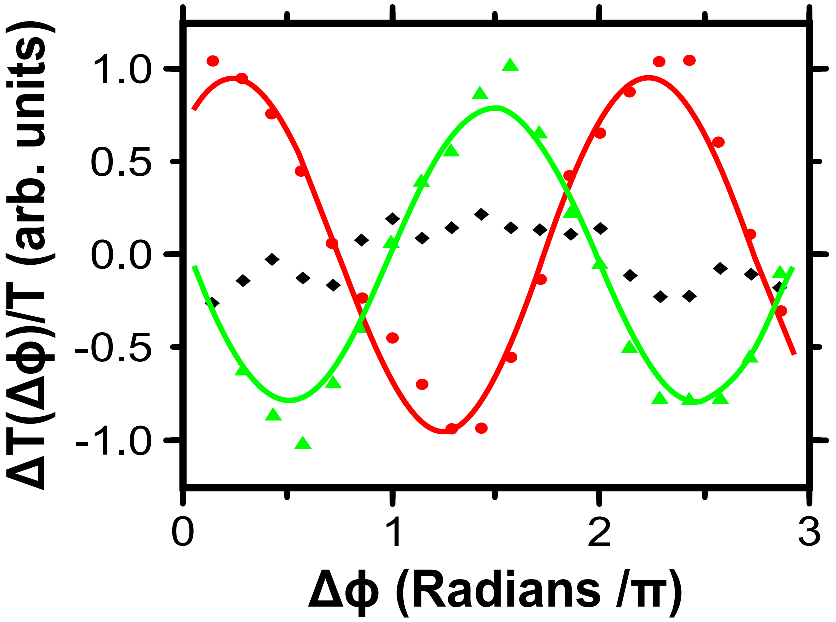

Figure 2.9: Phase dependence of the pure spin current for excitation with the same circular polarization and a circularly polarized probe beam at the three probe positions $r = \pm 7.5\,\mu$m ((+) red dots and (-) green triangles) and $r = 0\,\mu$m (black diamonds). The lines represent sinusoidal fits. (According to [64])

beam, which is detected through the differential transmission. The detected spin-flavor is determined by the choice of the polarization, which is the only change to the setup from [60].

Fig. 2.9 displays the phase-dependent change in probe transmission that is proportional to the change in occupancy of the optically coupled states. Depending on the polarization it is either a measure of the spin-up or spin-down electron density at a given probe position. As expected for QUIC, the spin populations vary cosinusoidally with $\Delta\phi$ at both probe positions. The expected phase shift of $\pi$ is not exactly met. This mismatch is attributed to not perfectly parallel wave fronts of the $\omega$ and $2\omega$ beams.

The shift distance is estimated to be approximately 10 nm which corresponds to a separation of the spin profiles of 20 nm. This concurs with theoretically predicted values of 90 nm for electrons with excess energies of 200 meV and an assumed relaxation time of 45 fs. The calculations do not take the non-uniform carrier velocity into account. It is better described by a distribution of velocities and spin orientations. This reduces the expected separation and brings it closer to the value from the measurements.

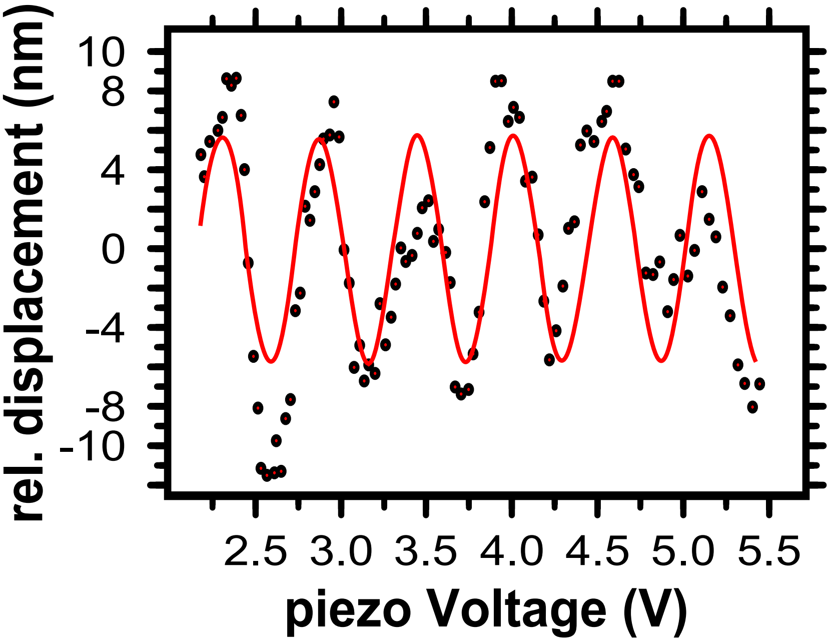

Figure 2.10: Displacement of the PL spots for excitation with the two-color light field of orthogonally polarized beams. (According to [63])

Qualitatively identical results albeit on cubic ZnSe crystals were obtained in [63]. In a time-resolved setup the displacement of the spin distributions is cleverly measured by the movement of the photoluminescence (PL) of the ZnSe crystal when excited with the two-color light field of orthogonally polarized beams. The polarization of the PL is resolved by a Wollaston prism, and the movement of the spots recorded with a CCD camera. The short distances are resolved through a differential measurement technique, see Fig. 2.10. The theoretical predictions are in the range of 100 nm. But the caveat from above applies here as well.

Further work has since resolved the dynamics spatially and temporally [65] and successfully injected spin currents using a single color by using the interference between the left and right circularly polarized light components of the pulse [66].

## 2.3 Ultrafast Currents

In this section the equations for the three ultrafast currents that are accessible through the second-order susceptibility are derived.

### 2.3.1 Derivation

The traditional definition of the microscopic current density is given by [67]

$$\mathbf{J}(\mathbf{x},t) = \sum_j q_j \, \mathbf{v}_j \, \delta(\mathbf{x} - \mathbf{x}_j(t)), \tag{2.54}$$

with the velocity of the $j$-th charge

$$\mathbf{v}_j = \frac{\mathrm{d}\mathbf{x}_j}{\mathrm{d}t}. \tag{2.55}$$

A similar term for the full-body Hamiltonian is derived by introduction of a new polarisation operator **P** [36]. It is linked to the current density by

$$\mathbf{J}(t) = \frac{\mathrm{d}\mathbf{P}(t)}{\mathrm{d}t}. \tag{2.56}$$

The inter- and intraband contributions prove to be separable according to

$$\mathbf{P}(t) = \mathbf{P}_{\mathrm{intra}}(t) + \mathbf{P}_{\mathrm{inter}}(t). \tag{2.57}$$

The problem and its solution are described phenomenologically [36]. First, there is the typical full-body Hamiltonian,

$$H(t) = \int \psi^{+}(\mathbf{x},t) \, \mathcal{H} \, \psi(\mathbf{x},t) \, \mathrm{d}\mathbf{x} + H_{\mathrm{rest}}, \tag{2.58}$$

with

$$\mathcal{H}(t) = \left[ -\mathrm{i}\hbar\nabla - \frac{e}{c}\mathbf{A}(t) \right]^2 + V(\mathbf{x}). \tag{2.59}$$

Here, the $\psi(\mathbf{x},t)$ and $\psi^{+}(\mathbf{x},t)$ are the electron field operators, that respectively create and destroy electrons in the bands. They obey the anticommutator relation $\{\psi(\mathbf{x},t), \psi^{+}(\mathbf{x},t)\} = \delta(\mathbf{x} - \mathbf{x}')$; the vector potential $\mathbf{A}(t)$ describes the electric field according to $\mathbf{E}(t) = \dot{\mathbf{A}}(t)/c$. This approach uses a periodic potential

$V(\mathbf{x}) = V(\mathbf{x}+\boldsymbol{\alpha})$ with the lattice vector $\boldsymbol{\alpha}$. The remaining electron-electron and phonon-electron interactions are bundled into $H_{\text{rest}}$.

The evolution of a field operator is given by the Heisenberg equation of motion according to

$$\mathrm{i}\hbar\frac{\mathrm{d}\psi}{\mathrm{d}t} = \Big[\psi(\mathbf{x},t), H(t)\Big]. \tag{2.60}$$

A new field operator is defined for this problem

$$\tilde{\psi}(\mathbf{x},t) \equiv \psi(\mathbf{x},t)\,\mathrm{e}^{-\mathrm{i}\mathbf{K}(t)\mathbf{x}}, \tag{2.61}$$

in order to accommodate the modified Hamiltonian, where the contributions of the electron motion and the field are separated

$$H_{\text{eff}} = \int \tilde{\psi}(\mathbf{x},t)\Big[\mathcal{H}_0 - e\mathbf{x}E(t)\Big]\tilde{\psi}(\mathbf{x},t)\mathrm{d}\mathbf{x} + H_{\text{rest}}, \tag{2.62}$$

which requires

$$\mathcal{H}_0 \equiv \Big[-\mathrm{i}\hbar\nabla\Big]^2 + V(\mathbf{x}). \tag{2.63}$$

The equation of motion

$$\mathrm{i}\hbar\frac{\mathrm{d}\tilde{\psi}}{\mathrm{d}t} = \Big[\tilde{\psi}(\mathbf{x},t), H_{\text{eff}}(t)\Big] \tag{2.64}$$

needs to be solved. An explicit Hermetian form for $H_{\text{eff}}$ is given by [36]

$$\begin{aligned} H_{\text{eff}}(t) = {} & \sum_n \int \mathrm{d}\mathbf{k}\,\hbar\omega_n(\mathbf{k})\,a_n^+(\mathbf{k})a_n(\mathbf{k}) \\ & - \mathrm{i}e\mathbf{E}(t)\sum_n \int \mathrm{d}\mathbf{k}\Big[a_n^+(\mathbf{k})\,\partial a_n(\mathbf{k})\Big] \\ & - e\mathbf{E}(t)\sum_{n,m}\int \mathrm{d}\mathbf{k}\,\mathbf{r}_{nm}\,a_n^+(\mathbf{k})a_m(\mathbf{k}) + H_{\text{rest}}, \end{aligned} \tag{2.65}$$

with the fermion operators $a_n(\mathbf{k})$ that satisfy the anticommutation relation:

$$\Big\{a_n(\mathbf{k}), a_m^+(\mathbf{k})\Big\} = \delta_{nm}\delta(\mathbf{k}-\mathbf{k}'). \tag{2.66}$$

Here, the time-dependence of the $a_n(\mathbf{k})$ is left implicit.

The term $\left[a_n^+(\mathbf{k})\,\partial a_n(\mathbf{k})\right]$ is an abbreviation for

$$\left[a_n^+(\mathbf{k})\,\partial a_n(\mathbf{k})\right] \equiv \frac{1}{2}\left[a_n^+(\mathbf{k})\frac{\partial a_n(\mathbf{k})}{\partial \mathbf{k}} - \frac{\partial a_n^+(\mathbf{k})}{\partial \mathbf{k}}a_n(\mathbf{k})\right] - \mathrm{i}\xi_{nn}(\mathbf{k})a_n^+(\mathbf{k})a_n(\mathbf{k}). \tag{2.67}$$

This requires the definition of $\xi_{nm}(\mathbf{k})$

$$\xi_{nm}(\mathbf{k}) = \frac{\mathbf{v}_{nm}(\mathbf{k})}{\mathrm{i}\omega_{nm}(\mathbf{k})}, \tag{2.68}$$

with

$$\omega_{nm} = \omega_n - \omega_m, \tag{2.69}$$

and of the velocity matrix elements $\mathbf{v}_{nm}$ with the electron free mass $m$

$$\frac{1}{m}\int \psi_n^*(\mathbf{k},\mathbf{x})\left[-\mathrm{i}\hbar\nabla\right]\psi_m(\mathbf{k},\mathbf{x})\mathrm{d}\mathbf{x} = \mathbf{v}_{nm}(\mathbf{k})\delta(\mathbf{k}-\mathbf{k}'). \tag{2.70}$$

The current density operator in the Heisenberg picture is given by

$$\mathbf{J}(t) = \frac{e}{m}\int \frac{\mathrm{d}\mathbf{x}}{\Omega}\psi^+(\mathbf{x},t)\left[-\mathrm{i}\hbar\nabla - \frac{e}{c}\mathbf{A}(t)\right]\psi(\mathbf{x},t) \tag{2.71}$$

$$= \frac{e}{m}\int \frac{\mathrm{d}\mathbf{x}}{\Omega}\tilde{\psi}^+(\mathbf{x},t)\left[-\mathrm{i}\hbar\nabla\right]\tilde{\psi}(\mathbf{x},t) \tag{2.72}$$

$$= e\sum_{nm}\int \frac{\mathrm{d}\mathbf{k}}{\Omega}\mathbf{v}_{nm}(\mathbf{k})a_n^+(\mathbf{k})a_m(\mathbf{k}), \tag{2.73}$$

with the reference volume $\Omega$. The explicit Hermetian form of equation (2.65) reveals a polarization operator, with separate contributions for inter- and intraband polarizations

$$\mathbf{P}_{\text{inter}}(t) = e\int \frac{\mathrm{d}\mathbf{k}}{\Omega}\sum_{nm}\mathbf{r}_{nm}(\mathbf{k})a_n^+(\mathbf{k})a_m(\mathbf{k}) \tag{2.74}$$

$$\mathbf{P}_{\text{intra}}(t) = \mathrm{i}e\int \frac{\mathrm{d}\mathbf{k}}{\Omega}\sum_{n}\mathbf{r}_{nm}(\mathbf{k})a_n^+(\mathbf{k})\partial a_n(\mathbf{k}). \tag{2.75}$$

The $\mathbf{r}_{nm}$ are defined by their relation to the $\xi$

$$\mathbf{r}_{nm} \equiv \begin{cases} \xi_{nm}(\mathbf{k}) & \text{if } n \neq m \\ 0 & \text{else.} \end{cases} \tag{2.76}$$

In the end a modified Hamiltonian is obtained

$$H_{\mathrm{eff}}(t) = H_0 - \Omega\Big[\mathbf{P}_{\mathrm{inter}}(t) + \mathbf{P}_{\mathrm{intra}}(t)\Big]\mathbf{E}(t) + H_{\mathrm{rest}}. \tag{2.77}$$

Relation (2.56) follows from the Heisenberg equation of motion, as long as

$$\Big[\mathbf{P}(t), H_{\mathrm{rest}}\Big] = 0. \tag{2.78}$$

This is expected to hold, as long as the electron degrees of freedom of $H_{\mathrm{rest}}$ only depend on the position of the electrons. Most models of the electron-photon interaction concur with this condition.

### 2.3.2 Second-Order effects

Shift and rectification currents are a consequence of the second-order response,

$$\langle \mathbf{J}_2(t)\rangle = \frac{\mathrm{d}\,\langle \mathbf{P}_2(t)\rangle}{\mathrm{d}t}, \tag{2.79}$$

with the polarization operator

$$\Big\langle P_2^a(t)\Big\rangle = \chi_2^{abc}(-\omega_\epsilon;\omega_\beta,\omega_\gamma)E_\beta^b E_\gamma^c\,\mathrm{e}^{-\mathrm{i}\omega_\epsilon t}. \tag{2.80}$$

The splitting of the polarization operator is passed onto the optical susceptibility

$$\chi_2^{abc}(-\omega_\epsilon;\omega_\beta,\omega_\gamma) = \chi_{2\mathrm{inter}}^{abc}(-\omega_\epsilon;\omega_\beta,\omega_\gamma) + \chi_{2\mathrm{intra}}^{abc}(-\omega_\epsilon;\omega_\beta,\omega_\gamma), \tag{2.81}$$

where $\chi_{2\mathrm{inter}}$ includes only interband effects, while $\chi_{2\mathrm{intra}}$ pools all the contributions of the intraband interactions. It can be written as the sum of three tensors, that are related to distinct current induction processes

$$\begin{aligned}\chi_{2\mathrm{intra}}^{abc}(-\omega_\epsilon;\omega_\beta,\omega_\gamma) = {} & \frac{\eta_2^{abc}(-\omega_\epsilon;\omega_\beta,\omega_\gamma)}{(-\mathrm{i}\omega_\epsilon)^2}\\ & + \frac{\sigma_2^{abc}(-\omega_\epsilon;\omega_\beta,\omega_\gamma)}{(-\mathrm{i}\omega_\epsilon)}\\ & + \tilde{\chi}_{2\mathrm{intra}}^{abc}(-\omega_\epsilon;\omega_\beta,\omega_\gamma).\end{aligned} \tag{2.82}$$

The structures of the denominators indicate that the divergence of $\chi_2$ is certain for ($\omega_\epsilon \to 0$).

The ultrafast currents originate from the special case of the optical susceptibility $\chi_2^{abc}(0;\omega,-\omega)$. First, the intraband contribution is discussed for steady state excitation with a single optical frequency as in [36]. It is split into two distinct processes,

$$\langle \mathbf{J}_{2\text{intra}} \rangle = \langle \mathbf{J}_{2\text{injection}} \rangle + \langle \mathbf{J}_{2\text{shift}} \rangle . \tag{2.83}$$

The electric field is generally of the form

$$\mathbf{E}(t) = \mathbf{E}(\omega)\,\mathrm{e}^{-\mathrm{i}\omega t} + \mathbf{E}(-\omega)\,\mathrm{e}^{\mathrm{i}\omega t}. \tag{2.84}$$

The relationship between the currents and the tensors is further specified in the following segment.

- **Injection currents** The physics of this process become clear, by a Fermi golden rule calculation [68]. It originates from the interference of one-photon absorption processes associated with different linear polarizations of light. The expectation value is given by

  $$\frac{\mathrm{d}\left\langle J^{a}_{2\text{injection}}\right\rangle}{\mathrm{d}t} = \eta_2^{abc}(-\omega_\epsilon;\omega_\beta,\omega_\gamma)E^b_\beta E^c_\gamma\,\mathrm{e}^{-\mathrm{i}\omega_\epsilon t} \tag{2.85}$$

  $$= 2\eta_2^{abc}(0;\omega,-\omega)E^b(\omega)E^c(-\omega), \tag{2.86}$$

  $\eta_2$ turns out to be purely imaginary [68], and yields

  $$= -2\mathrm{Im}\Big(\eta^{abc}(\omega)\Big)\Big|E^b(\omega)\Big|\Big|E^c(\omega)\Big|\sin(\phi^b-\phi^c) \tag{2.87}$$

  with $E^{b,c}(\omega) = |E^{b,c}(\omega)|\exp(\mathrm{i}\phi^{b,c})$. Current flow is only induced for elliptically polarized beams, with the maximal value for circularly polarized light. The direction of the current flow is controlled by the choice of right- or left-circularly polarized light, while magnitude and sign are subject to the relative phase between the electric fields.

  The third rank tensor $\eta_2^{abc}$ only exists in crystals without center of inversion symmetry. It possesses an antisymmetry in its last two Cartesian components, which reduces the possible crystal classes at first from 32 to 18. Unfortunately, GaAs and other zincblende crystals belong to class $\overline{43}m$, which does not survive. It is, therefore, impossible to observe injection currents in these materials.

- **Shift currents** The real-space center of charge differs for valence and conduction bands. Light absorption moves the electrons to the conduction band which cause a “shift” of the center of charge. It’s expectation value is given by

$$\langle J_{2\mathrm{shift}} \rangle = \sigma_2^{abc}(-\omega_\epsilon; \omega_\beta, \omega_\gamma) E_\beta^b E_\gamma^c \, \mathrm{e}^{-\mathrm{i}\omega_\epsilon t} \tag{2.88}$$

$$= 2\sigma_2^{abc}(0; \omega, -\omega) E^b(\omega) E^c(-\omega). \tag{2.89}$$

The shift current tensor is symmetric with respect to the last two Cartesian components. This implies, that from the 21 crystal classes without a center of inversion, shift currents are only forbidden for the crystal class 432. It should, therefore, be measurable in GaAs and all other zincblende structures.

For discussion of the rectification contribution [37], an excitation pulse of the form

$$\mathbf{E}(t) = \mathbf{E}_{\mathrm{env}}(t) \, \mathrm{e}^{-\mathrm{i}\omega_0 t} + \mathbf{E}^*_{\mathrm{env}}(t) \, \mathrm{e}^{\mathrm{i}\omega_0 t} \tag{2.90}$$

is considered, which in Fourier space yields

$$\mathbf{E}(\omega) = \mathbf{E}_{\mathrm{env}}(\omega + \omega_0) + \mathbf{E}_{\mathrm{env}}(\omega - \omega_0). \tag{2.91}$$

- **DC polarization** The interband polarization $\chi_{2\mathrm{rect}}^{abc}$ contains not only contributions from the intraband susceptibility, but also from the shift current tensor $\sigma_2$ that survives for all frequencies. Especially for energies below the band gap

  $$\chi_{\mathrm{rect}}^{abc}(\omega) = \chi_{2\mathrm{inter}}^{abc}(0; \omega, -\omega) + \tilde{\chi}_{2\mathrm{intra}}^{abc}(0; \omega, -\omega) + \frac{\partial \Lambda_{\mathrm{I}}^{abc}(\omega)}{\partial \omega}, \tag{2.92}$$

  where $\Lambda_{\mathrm{I}}^{abc}$ is part of the single-frequency effective coeffient of $\sigma_2$ that contains the virtual polarization contributions of $\sigma_2^{abc}$

  $$\sigma_2^{abc}(-\omega_\epsilon; \omega_\beta, \omega_\gamma) = -\mathrm{i}\Big(\Lambda_{\mathrm{I}}^{abc}(\omega_\beta) + \Lambda_{\mathrm{II}}^{abc}(\omega_\gamma)\Big). \tag{2.93}$$

  With this, the expectation value of the current is given by

  $$\Big\langle J_{2\mathrm{rect}} \Big\rangle = 2\chi_{2\mathrm{rect}}^{abc}(\omega_0) \frac{\mathrm{d}}{\mathrm{d}t} \Big( E_{\mathrm{env}}^b(t) E_{\mathrm{env}}^c(t) \Big). \tag{2.94}$$

  This already considers the symmetry of the last two Cartesian components for zincblende crystals and yields a purely real tensor.

These detailed calculations not only yield the tensor elements of $\chi_2^{abc}$ for various excitation schemes and frequency ranges, but also provides estimates of the shift distance of the electrons in GaAs and GaP [37]. It is defined as the distance that the electron center of mass shifts upon absorption of a photon. In zincblende systems, when excited with linearly polarized light along the [111] direction, the current is proportional to the carrier absorption rate $\dot{n}$. In the continuous wave limit the distance is given by

$$d_{\text{shift}}(\omega) = \left| \frac{J^a_{\text{shift}}}{e\dot{n}} \right| \tag{2.95}$$

$$= 8\pi \frac{\Lambda_{\text{II}}^{xyz}(\omega)}{\varepsilon_2^{xx}(\omega)}. \tag{2.96}$$

Here, $\varepsilon_2^{xx}(\omega)$ is the imaginary part of the dielectric function. The Γ-point wave functions are localized around the arsenic atoms at the top of the valence band, while they are localized around the gallium atoms at the bottom of the conduction band. It is expected that absorption near the band edge causes a shift distance on the order of the bond lengths which are set to 2.45 Å for GaAs and 2.36 Å for GaP, see Fig. 2.11.

The behavior of both material systems is comparable. As the energy reaches

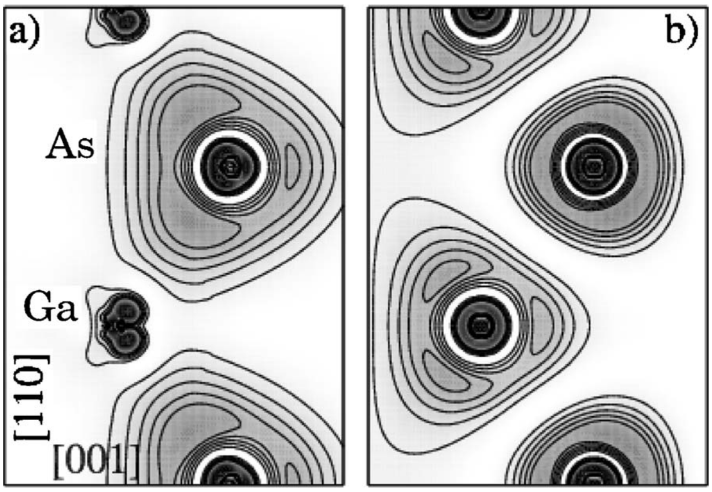

Figure 2.11: Contour plot of the electron density in the [110] plane of GaAs at the (a) highest Γ valence electron and (b) the lowest Γ point conduction band. Higher electron densities are displayed darker. Data of panel (b) was adjusted by a factor two. (According to [37])

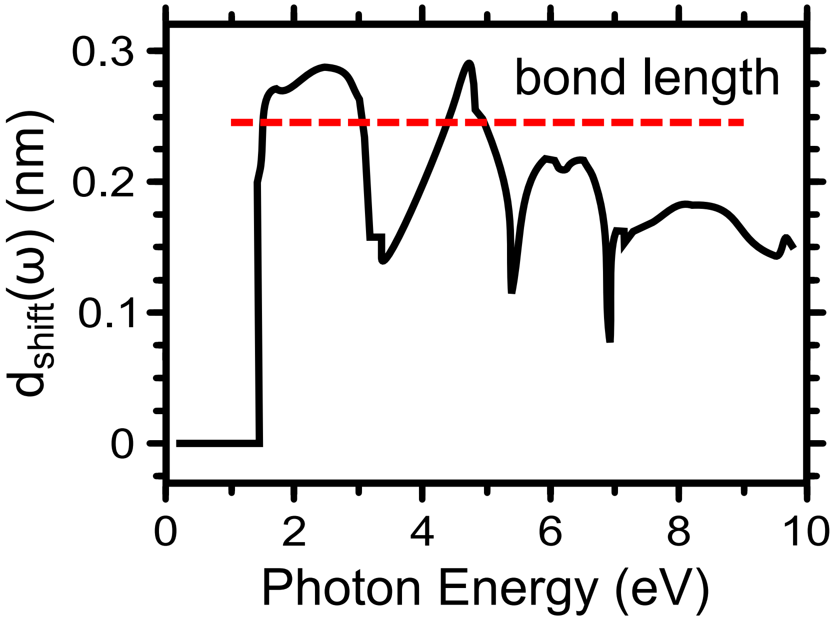

(a) GaAs

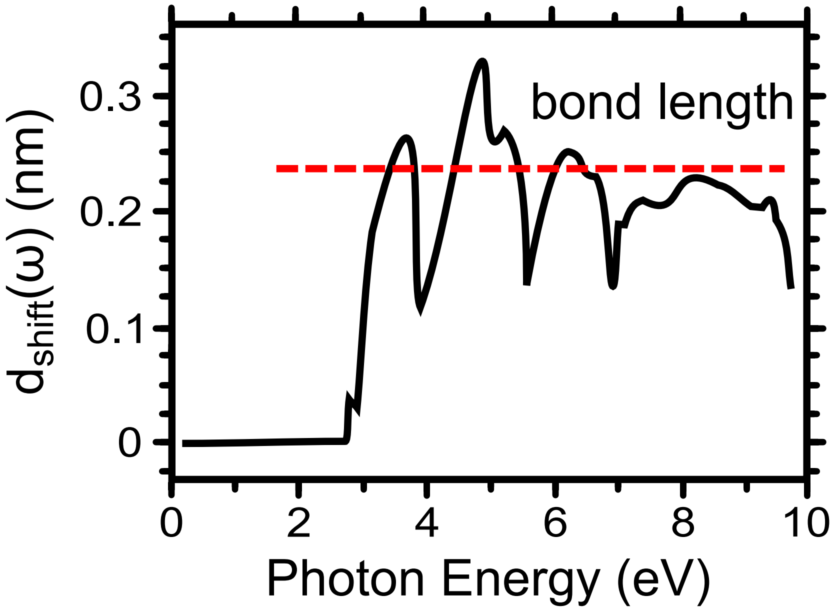

(b) GaP

Figure 2.12: Frequency dependence of the shift distance for GaAs and GaP. (According to [37])

the band gap ($E_g$(GaAs) = 1.43 eV and $E_g$(GaP) = 2.26 eV) the electrons start to move and even overshoot the bond length. An oscillatory pattern emerges, which is correlated with the energies of high absorption, a region where the valence and conduction bands energies are nearly parallel [37]. The split-off bands are visible as dips just after the band edges, see Fig. 2.12.

### 2.3.3 Injection, Shift and Rectification Currents

This section highlights some of the experiments that focus on the second-order induced current density, its related THz emission and the coherent-control paradigm.

The derivation in section 2.3.2 has revealed that the current densities stem from divergences in the second order susceptibility as detailed in equation (2.82). It is reproduced here for convenience:

$$\begin{aligned}\chi_{2\text{intra}}^{abc}(-\omega_\epsilon;\omega_\beta,\omega_\gamma) = {} & \frac{\eta_2^{abc}(-\omega_\epsilon;\omega_\beta,\omega_\gamma)}{(-\mathrm{i}\omega_\epsilon)^2} \\ & + \frac{\sigma_2^{abc}(-\omega_\epsilon;\omega_\beta,\omega_\gamma)}{(-\mathrm{i}\omega_\epsilon)} \\ & + \tilde{\chi}_{2\text{intra}}^{abc}(-\omega_\epsilon;\omega_\beta,\omega_\gamma).\end{aligned}$$

The evolution of the current density follows the electric field and is summed up by

$$\frac{\mathrm{d}J_{\text{inj}}}{\mathrm{d}t} = 2\varepsilon_0\eta_2\, E(t)E^*(t), \tag{2.97}$$

$$J_{\text{shift}} = 2\varepsilon_0\sigma_2\, E(t)E^*(t), \tag{2.98}$$

$$J_{\text{rect}} = 2\varepsilon_0\chi_2\,\frac{\partial}{\partial t}E(t)E^*(t). \tag{2.99}$$

Here, the tensors are treated without dispersion in the limit

$$\omega_\beta \to \omega_\gamma = \omega_\epsilon \to 0. \tag{2.100}$$

This describes the mixing of two light-field components of the same frequency. These formulas expose the dependence of the current density on the optical pulse envelope. The shift current follows it directly, while the rectification current follows its time derivative.

#### The symmetry relations of the $\sigma^{abc}$ tensor

The symmetry properties of the shift and injection current tensors $\sigma_2^{abc}$ and $\eta_2^{abc}$ were described in section 2.1.3.

The properties of the $T_d$ point group of (110)-oriented bulk GaAs do not allow any nonzero elements for the current injection tensor. However, by growing symmetric, strained, or unstrained quantum wells (QW), the point group is reduced to

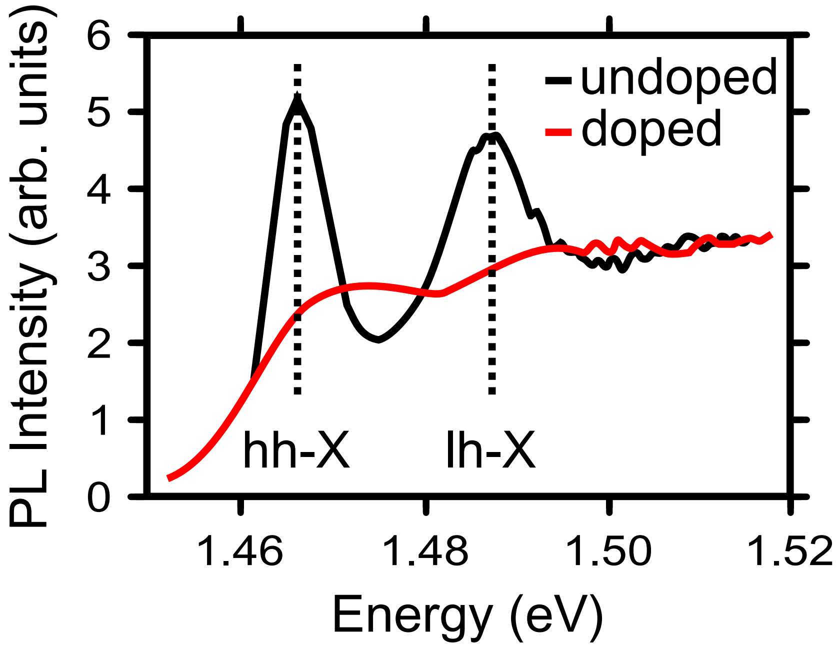

Figure 2.13: PLE spectrum of the doped (red line) and undoped (black line) GaAs QW sample at room temperature. The exciton transitions are highlighted. (According to [69])

$C_{2v}$. This yields new tensor elements. In addition to the extra shift tensor element ($xxx$), four new injection tensor elements appear ($yyx = -yxy$, $zxz = -zzx$). Both, the ($xxx$) shift tensor element and the ($yyx$) injection tensor element produce measurable currents.

The optical properties of the GaAs QW are presented in the PhotoLuminescence Excitation (PLE) spectrum in Fig. 2.13. The QWs are grown on a (110)-oriented GaAs substrate with a 500 nm GaAs buffer layer in between. The QW region consists of 40 periods of GaAs/$Al_{0.3}Ga_{0.7}$. The wells and barriers share a width of 8 nm. The peaks belong to the heavy hole (hh) exciton (hh-X) and the light hole (lh) exciton (lh-X) resonances. The nature and the ratio of the excitons are set by the excitation conditions. Moving the center wavelength to the hh-X resonance generates mainly heavy hole excitons. The light hole resonance overlaps with the heavy hole continuum. Excitation at the light hole resonance creates both lh-x and free-electron-heavy-hole pairs. For excitation with light parallel to the [001] direction, the ratio between light and heavy hole excitons is expected to be equal. For excitation with light at energies higher than the light hole resonance the ratio between the free-electron-heavy-hole and free-electron-light-hole pairs is expected to be 2:1 [70, 71].

The last two indices of the tensors indicate the direction of the light fields. It is

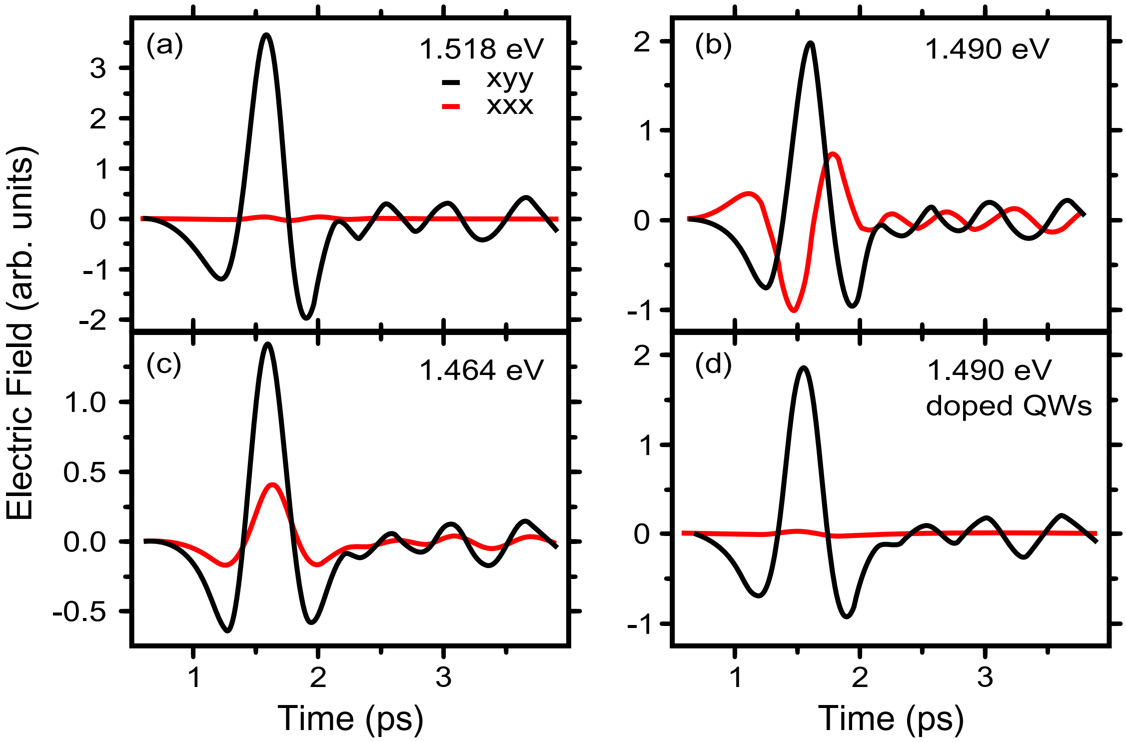

Figure 2.14: THz traces associated with the (*xyy*) (black line) and (*xxx*) (red line) current density for different excitation photon energies. (a) Excitation at 1.518 eV @ the hh & lh continuum. (b) Excitation at 1.490 eV @ the lh exciton. (c) Excitation at 1.464 eV @ the hh exciton. (d) Excitation at 1.490 eV @ the lh excitation, doped QW. (According to [69])

therefore easy to achieve comparable experimental conditions for the measurement of the THz emission for the two currents. A simple rotation of the polarization gives access to the relevant current density. The experiment was conducted for different excitation conditions, beginning at photon energies slightly larger than the light hole resonance at 1.518 eV. Going on, the photon energy was first set to the light hole resonance at 1.490 eV and then to the heavy hole resonance at 1.464 eV. The shape of the THz trace for the (*xyy*) induced current density hardly changes. But the situation for the (*xxx*) case is different. While at first, no THz emission is detectable, a clear THz trace becomes visible at the light hole resonance and drastically alters its shape at the heavy hole resonance. The peak-to-peak amplitude decreases from 0.6 of the (*xyy*)-based THz trace to 0.3 for the (*xxx*) case, see Fig 2.14. The shifting shape corresponds to a phase shift in the THz spectrum and is attributed to a current reversal process [69]. An explanation for this reversal is given through a model presented in [34].

The GaAs crystal lattice is held together by strong ionic bonds that induce permanent dipole moments along the bonds in the [111] directions. There is no discernible dipole moment for the equilibrium conditions, as the contributions cancel each other out. Excitation at the exciton resonances lead to significant dipole moments along opposite directions depending on the chosen resonance. This distinction leads to the measured current reversal [69, 72].

The effects of n-doping the quantum well barriers with a Si concentration of $n = 8 \times 10^{10}\,cm^{-2}$ are shown in Fig. 2.13 and Fig. 2.14. The distinct peaks of the exciton resonances vanish. The free carriers screen the Coulomb attraction. This in turn weakens the exciton binding energy and decreases the strength of the exciton resonance. As a consequence, no ($xxx$) shift current signal is visible.

A similar phase shift is also observed for the ($yxy$) based injection current, see Fig. 2.14. But the underlying process of the current reversal is different. In crystal structures that possess an inversion asymmetry the spin orbit interaction leads to a splitting of the spin subbands that are linear in $k$. Using circularly polarized light of the same helicity couples different subbands depending on the photon energy of the light source. Carrier distributions produced at the lh and hh exciton resonance flow in opposite directions [72, 73].

### Wurtzite Crystals

The symmetry properties of the wurtzite crystal structure ($6mm$) provide an opportunity to simultaneously generate shift and injection currents in the same material using a polarization dependent single-color coherent-control scheme [74]. The interference is induced here, by connecting initial and final states through two beams with distinct polarizations. The current generation process is related to a third rank tensor. It is described by these equations:

$$J^z_{\text{shift}} = 2\sigma^{zzz}\left|E^z\right|^2 + 2\sigma^{zxx}\left|E^x\right|^2, \tag{2.101}$$

$$J^x_{\text{shift}} = 4\sigma^{xzx}\left|E^x\right|\left|E^z\right|\cos(\phi^z - \phi^x), \tag{2.102}$$

$$\frac{\mathrm{d}J^x_{\text{inj}}}{\mathrm{d}t} = -4\mathrm{i}\eta^{xzx}\left|E^x\right|\left|E^z\right|\sin(\phi^z - \phi^x). \tag{2.103}$$

There are three unique non-zero tensor elements that are suitable for shift currents ($zzz, zxx, zxz = xxz$), and one unique tensor element for injection currents ($xzx = -xxz$). The currents adhere to different physical processes and crystal symmetry properties which makes it possible to keep them apart [74].

The phase dependency of the magnitude of these currents is captured by the coherent control equations (2.101 – 2.103). Injection currents are maximal for

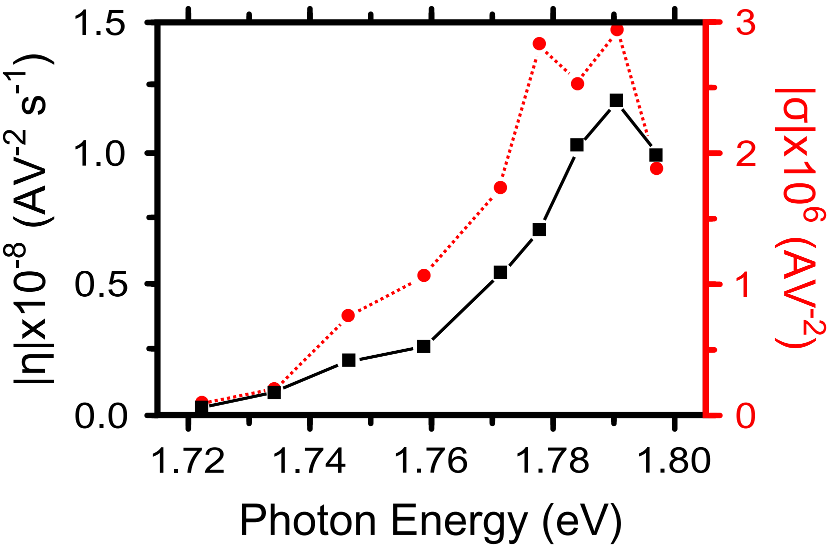

Figure 2.15: Magnitude of the tensor elements $\sigma^{zzz}$ (red dots) and $\eta^{zxz}$ (black squares) in CdSe as a function of photon energy. (According to [74])

circular polarization, while shift currents are best probed in a collinear polarization scheme. The experiments become very compelling in combination with a theoretical model. Inclusion of material and physical parameters into the model and tweaking the parameters until the recorded THz traces are reproduced, this gives insight into the magnitude of the current tensors $\sigma^{zzz}$ and $\eta^{zxz}$ and their dependence on the photon energy, see Fig. 2.15.

### Coherent Control

The THz emission characteristics of coherently controlled injection currents are given in [75]. The frequency spectrum of the room-temperature bulk GaAs sample is centered on 4 THz. It has a spectral width of 3 THz, but possesses a spectral hole below 2 THz. The experiment raises two important issues. This is evidence that the THz radiation is sensitive to the current generation process and is useful as a sensor. It additionally demonstrates how to coherently control the THz emission. The approach is straightforward. Tuning the relative phase between the two pulses that controls the magnitude of the injection current directly influences the magnitude of the emitted THz radiation, as shown in Fig. 2.16.

### Rectification and Shift Currents in GaAs

The use of light with photon energies above and below the band gap enables the comparison of the shift and rectification current density generated in the same (110)-oriented GaAs crystal. Contrary to the theoretically predicted results, see equations (2.98) and (2.99) the experimentally obtained traces show that the

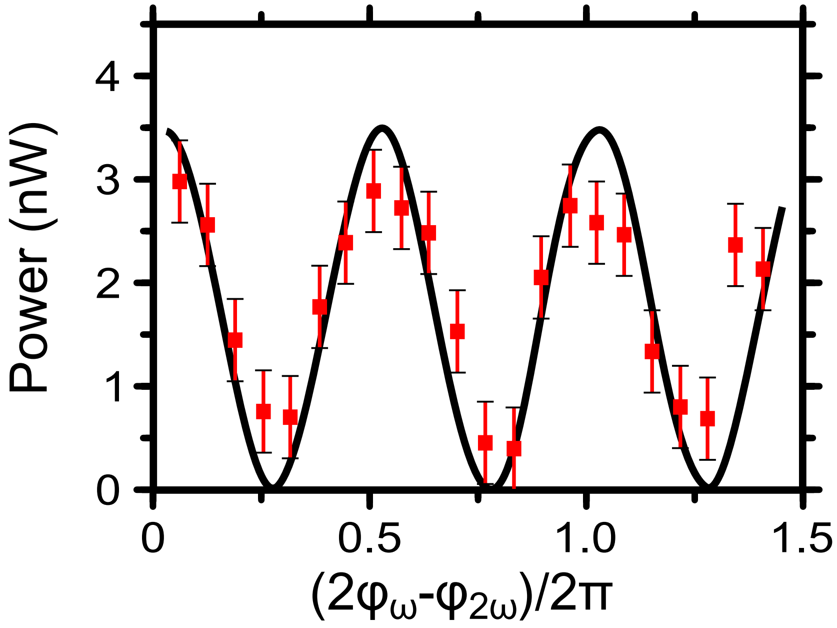

Figure 2.16: Phase dependence of the THz emission. (According to [75])

THz trace of the shift current density leads the rectification current THz trace by a phase shift of $\pi/2$. A simple model reveals that for peak carrier densities $n = 10 \times 10^{18}\,\mathrm{cm}^{-3}$ a current reversal occurs during the optical pulse [76]. This is similar to the response of a simple harmonic oscillator driven above and below its resonance frequency.

## 2.4 The Phase

The relationship between the spectrum of a pulse and its temporal shape is determined by the uncertainty principle. This constraint is introduced via the direct link between the frequency and the time-domain in the Fourier theorem [77]. The so-called time-bandwidth product for a Gaussian shaped pulse is given by

$$\Delta t\,\Delta\nu \geq 0.441. \tag{2.104}$$

The number on the right hand side of the equation depends on the chosen pulse shape, i.e., it is 0.315 for a secant-hyperbolicus ($\mathrm{sech}^2$) pulse [78]. The pulse length needs to be supported by the available bandwidth. Pulse lengths around 90 fs require a bandwidth of approximately 10 nm, pulse lengths that approach the sub-10 fs regime require at minimum a spectrum that spans an octave. Only bandwidth-limited pulses fulfill the equality. It is this predicament, that makes the phase of a laser pulse such a significant property. Its relevance grows with ever shorter pulses and becomes a great concern when entering the almost single optical-cycle regime. The harmonic frequency comb only became possible with the development of ever sophisticated tools to efficiently manage the phase [79].

The electric field in the time-domain is usually formulated according to

$$E(t) = \frac{1}{2}E_0(t)\,\mathrm{e}^{\mathrm{i}(\omega_0 t-\phi(t))} + \text{c.c.}. \tag{2.105}$$

The terms describe the rapidly varying carrier wave $\exp(\mathrm{i}\omega_0 t)$, the amplitude $E_0(t)$ and the time-dependent phase of the envelope $\phi(t)$. For use with a pulse shaper the frequency-domain is preferred. Here, the field is obtained by Fourier transformation

$$\tilde{E}(\omega) = \int_{-\infty}^{\infty} E(t)\,\mathrm{e}^{-\mathrm{i}\omega t}\,\mathrm{d}t\,. \tag{2.106}$$

Likewise, an inverse Fourier transformation connects the frequency to the time-domain

$$E(t) = \frac{1}{2\pi}\int_{-\infty}^{\infty} \tilde{E}(\omega)\,\mathrm{e}^{\mathrm{i}\omega t}\,\mathrm{d}\omega\,. \tag{2.107}$$

The field is separable into its spectrum $S(\omega)$ and its spectral phase $\phi(\omega)$

$$\tilde{E}(\omega) = \sqrt{S(\omega)}\, \mathrm{e}^{-\mathrm{i}\phi(\omega)}. \tag{2.108}$$

The phase is usually decomposed into its Taylor series

$$\phi(\omega) = \phi_0 + \left.\frac{\mathrm{d}\phi}{\mathrm{d}\omega}\right|_{\omega_0} (\omega - \omega_0) + \frac{1}{2} \left.\frac{\mathrm{d}^2\phi}{\mathrm{d}\omega^2}\right|_{\omega_0} (\omega - \omega_0)^2 + \cdots . \tag{2.109}$$

The zeroth order of the Taylor series is the absolute phase or the carrier-envelope phase (CEP). The maximum of the electric field and the pulse envelope don't usually overlap. The offset between these two is given by the absolute phase, see Fig. 2.17. For a laser pulse centered at 800 nm the period of a single oscillation of the light field is 2.67 fs. There are 37 oscillations in a 100 fs long pulse and the offset is therefore negligible. But for pulses that approach the single-cycle regime this is a serious concern. A lot of effort is put into stabilizing the carrier envelope phase [79]. And in fact the efficient generation of attosecond pulses and the maintenance of stable harmonic frequency combs became possible only after stabilization of the carrier envelope phase [80].

The first order of the Taylor series has no effect on the temporal shape of the pulse. It causes a temporal shift of the pulse, which is easily verifiable by a Fourier transformation according to

$$\tilde{E}(\omega)\, \mathrm{e}^{-\mathrm{i}\omega\tau} \to E(t - \tau). \tag{2.110}$$

This relationship shows how to implement an optical delay line in order to build an all optical setup. The time delay is calculated according to

$$\tau = -\frac{\mathrm{d}\phi}{\mathrm{d}\omega}. \tag{2.111}$$

Applying this phase to only a segment of the spectrum creates a second pulse at $\tau$. This is the so called 2-color pulse. It consists of two pulses that are phase stable and are centered around two new center frequencies, see Fig 2.18 [40].

Beginning with the second order of the Taylor series the manipulation of the phase has a direct influence on the pulse envelope. Application of a quadratic phase function results in linear chirp. This is a linear increase (decrease) of the frequency in time. Using positive values causes linear up-chirp, while negative values produce down-chirp. It leads to a broadening of the pulse, independent of

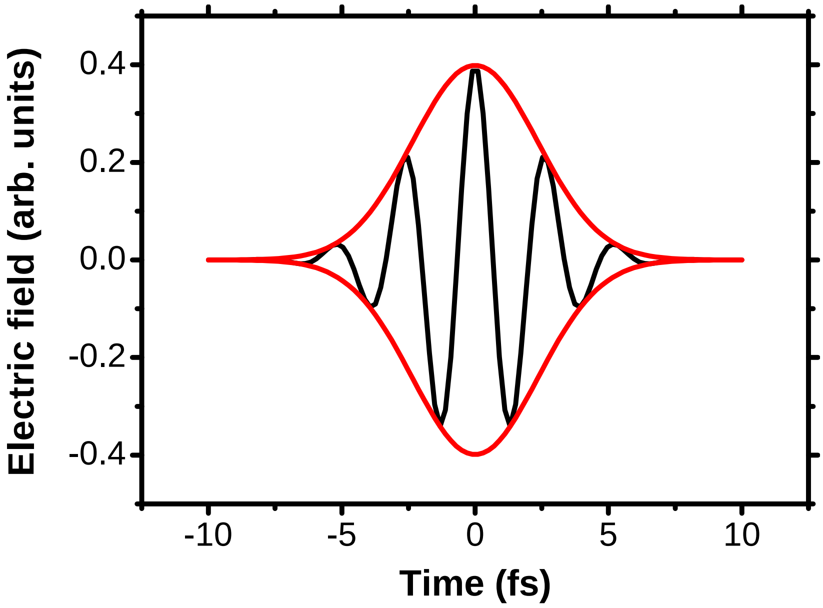

(a) Pulse with CE-phase $\phi = 0$

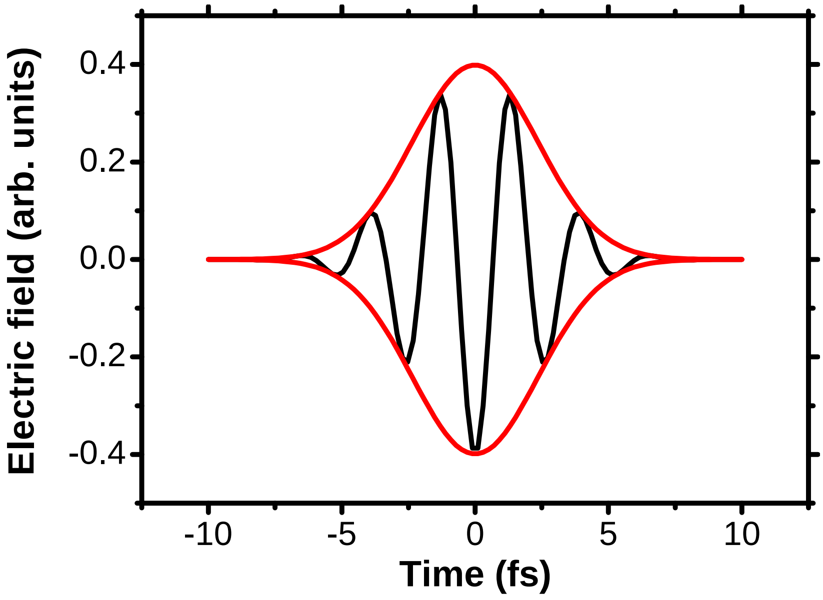

(b) Pulse with CE-phase $\phi = \pi$

Figure 2.17: Effects of the CEP on a few fs-pulse. The relative position of the maximum of the electric field to the pulse envelope is now tunable. Ramping up the phase to $\phi = \pi$ inverts the electric field, without any impact on the pulse envelope.

its sign, as the second term under the root is always larger than one [78]:

$$\Delta t_{\mathrm{out}} = \sqrt{\Delta t^2 + \left(4\ln 2 \frac{\phi^{(2)}}{\Delta t}\right)^2}. \tag{2.112}$$

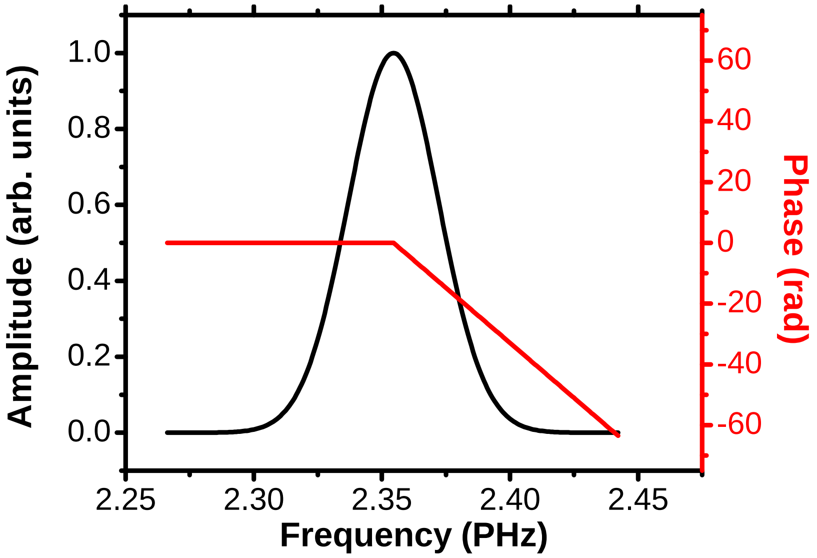

(a) Frequency-domain

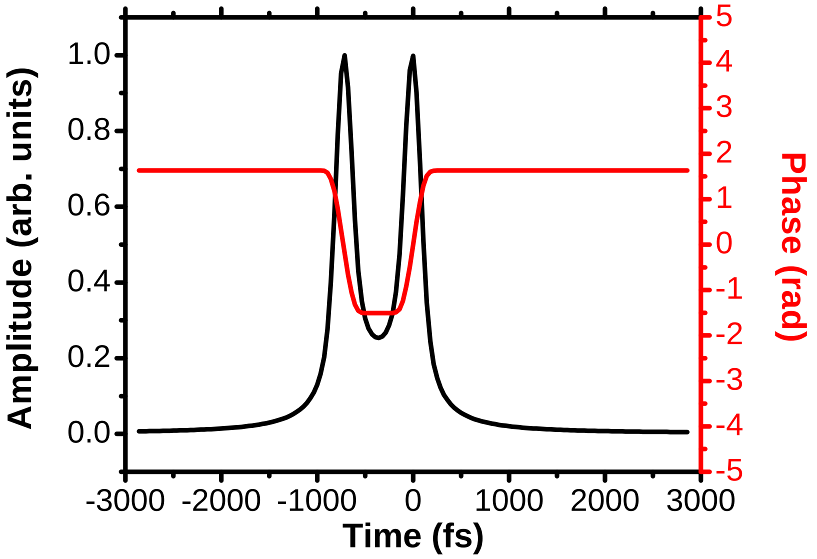

(b) Time-domain

Figure 2.18: The 2-color pulse is created by applying a sloped phase to only a segment of the available spectrum. The temporal separation of the two pulses is directly related to the slope of the line.

The third order of the Taylor series is called quadratic chirp. The odd orders of the Taylor series only have a marginal influence on the length of the pulse, but cause other distortions. They introduce asymmetry to the pulse that results in a substructure in the time-domain. Due to this, the Full Width at Half Maximum (FWHM) cannot be used as the determining factor for the pulse length anymore, see Fig. 2.19. More sophisticated methods for pulse characterization are required

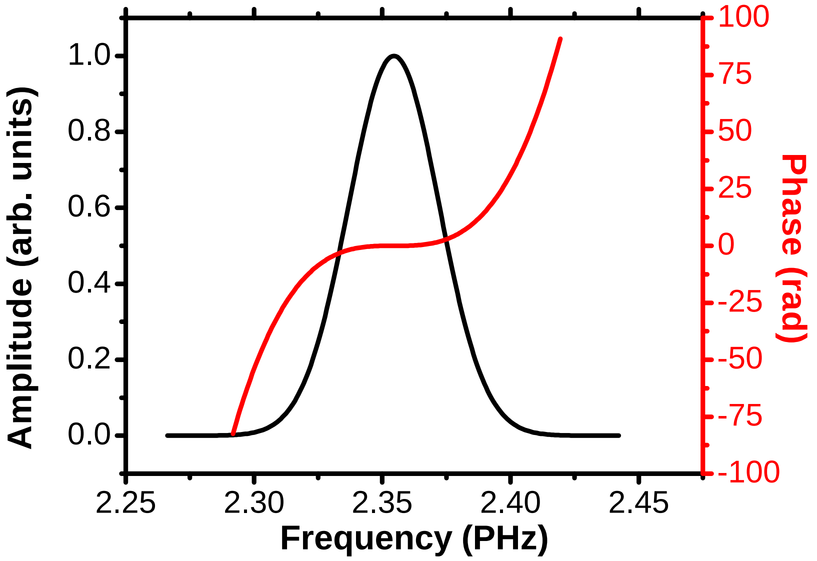

(a) Frequency-domain

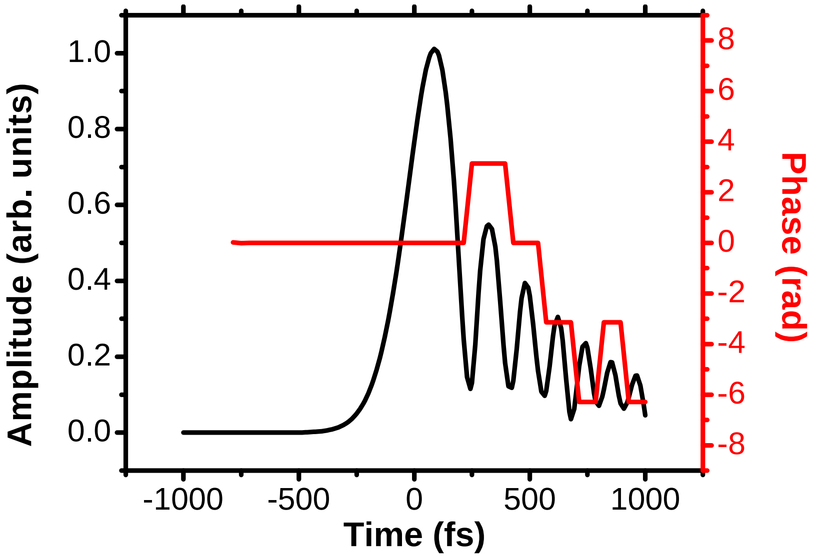

(b) Time-domain

Figure 2.19: Quadratic chirp only marginally influences the pulse length. It causes distortions in the time-domain which make the pulse asymmetric.

here. Full pulse characterization tools specify both, the spectrum and the phase of the pulse. These methods usually combine measurement of a property with a retrieval algorithm. FROG (Frequency Resolved Optical Gating) for example is based on a two dimensional representation of the pulse. A spectrum of the pulse is recorded with each delay step of the autocorrelator measurement. An iterative algorithm then reconstructs the pulse spectrum and phase [81].

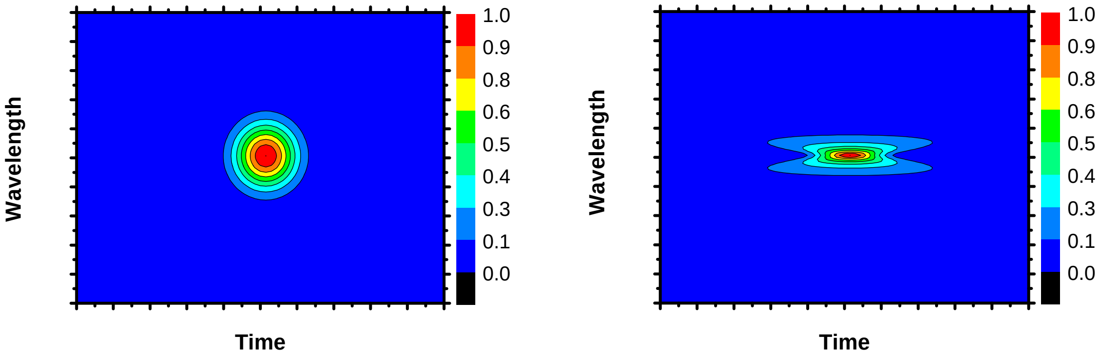

(a) Bandwidth limited pulse (b) Cubic phase distortion

Figure 2.20: FROG traces for a bandwidth-limited pulse and a pulse with quadratic chirp.

The FROG traces of a bandwidth-limited pulse and one with cubic phase distortions are contrasted with each other in Fig. 2.20. The effect of the phase distortion extends to both dimensions. It is evident, that a single autocorrelation trace would not capture the complexity of the pulse.

Several other mask shapes are in use to create pulse pairs. One of these uses a sinusoidally modulated phase function, see Fig. 2.21. It is represented by

$$\phi(\omega) = a\sin(b\omega + c). \tag{2.113}$$

The parameter $b$ is the temporal separation of the pulse pair, while $c$ distributes the energy between the pulses. The amplitude of the phase function is given by $a$ and is usually set to one. The pulse pair that results from this mask is bandwidth limited, which is discernible in the flat phase in the time-domain.

The rectangular phase mask is similar to the sinusoidal phase function in composition and effect. It is represented by

$$\phi(\omega) = a\,\mathrm{rect}(b\omega + c). \tag{2.114}$$

Its shape and the resulting pulse are shown in Fig. 2.22. Notable is the different development of the peaks. While the sinusoidally shaped pulse peaks seem to follow an undetermined envelope, the peaks of the rectangularly shaped phase resemble a train of pulses. The relationship between the temporal separation and the parameter $b$ is not as straightforward as before. Usually a calibration needs to be performed. The amplitude $a$ allows access to the relative CEP between the two pulses. This makes it a very interesting and versatile phase mask.

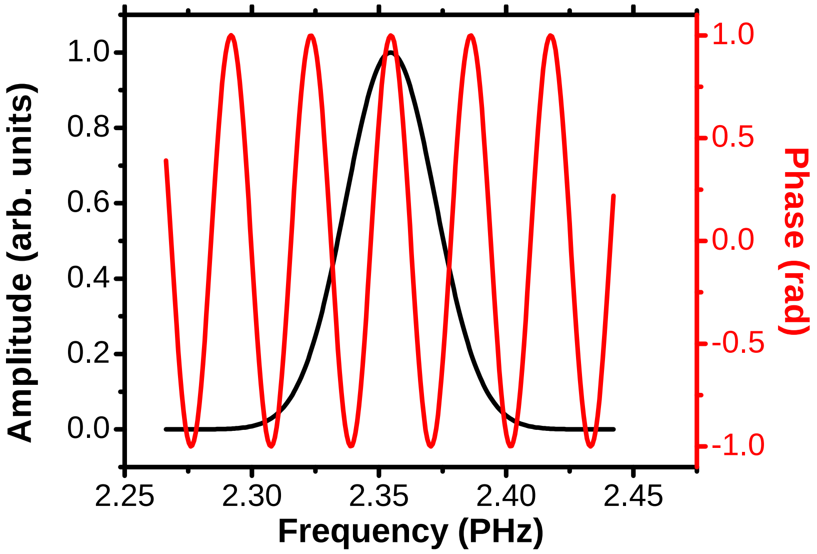

(a) Frequency-domain

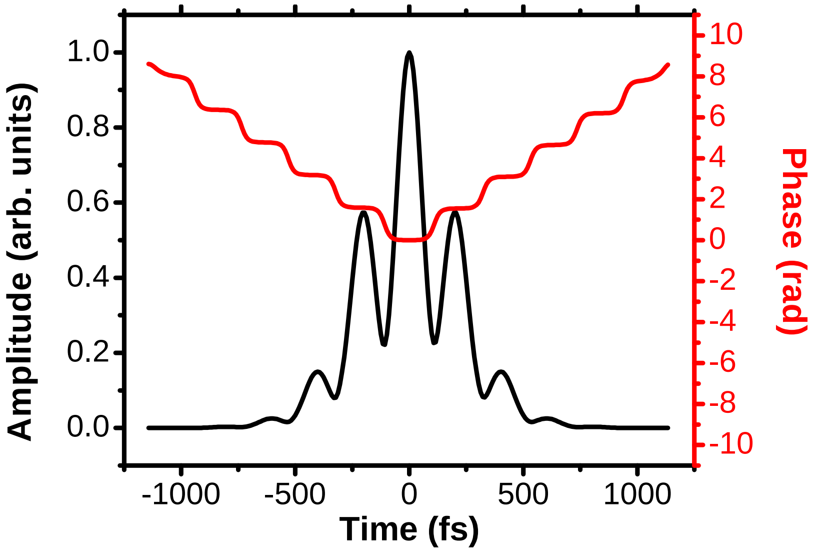

(b) Time-domain

Figure 2.21: Effects of a sinusoidal phase function.

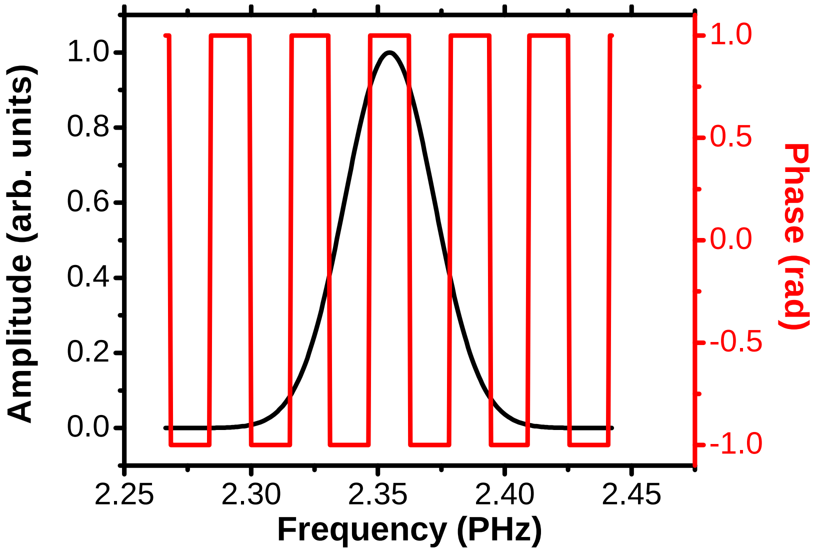

(a) Frequency-domain

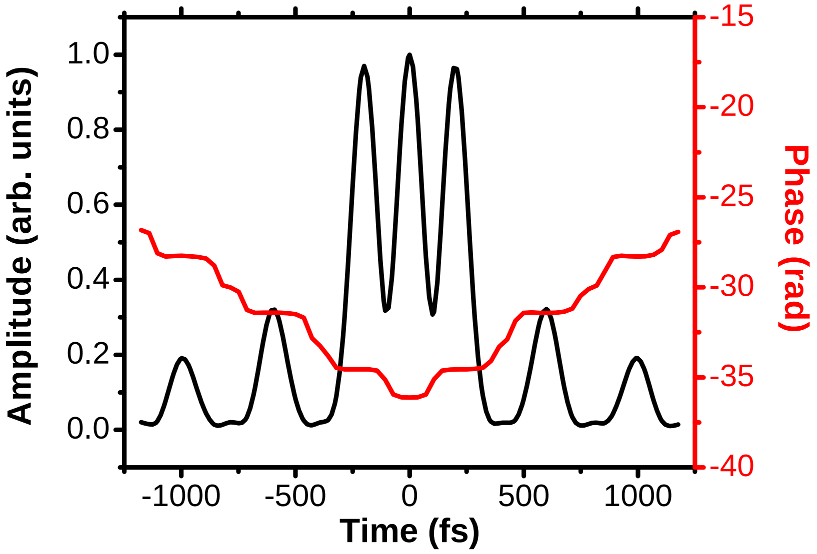

(b) Time-domain

Figure 2.22: Effects of a rectangular phase function.

# 3 The Setup, the Model, and the Feedback Loop

This chapter provides the technical basis for the experiments. The investigation of the coherent-control of ultrafast currents needs a sensor, a manipulative tool, and a framework within which the experiment is conducted. A THz time-domain setup is the sensor for the behavior of the ultrafast currents capturing their reaction to the action introduced by the pulse shaper. The coherent-control scheme is implemented through manipulation of the phase of the laser pulse. Additionally, an evolutionary algorithm is introduced to the framework to enable rapid adaptation of the THz trace to any specified target.

A straightforward phenomenological theoretical description is derived that replicates the experiment. It enables direct insight into the behavior of the current. It is based on the realization that the behavior of the current density is guided by the shape of the pulse envelope.

## 3.1 The THz Time-Domain Setup

THz time-domain spectroscopy technology has been well established in many groups worldwide. The experiences of our group with this technique and its specific implementation have been described in these contributions [48, 82–85].

Generally, a distinction needs to be made, as to what kind of a THz time-domain setup needs to be employed. Typically, for spectroscopic applications a relatively strong THz source such as an antenna-like device is used, as it is easier to obtain high signal to noise ratios with these sources. In these structures free carriers are generated in a semiconductor slab with a femtosecond laser pulse [87]. An external bias is applied to the isotropic carrier distribution that creates the accelerated carriers which emit radiation in the THz regime.

THz setups are also useful as sensors for processes that lead to radiation in the THz regime, i.e., shift and rectification currents. The choice of source material

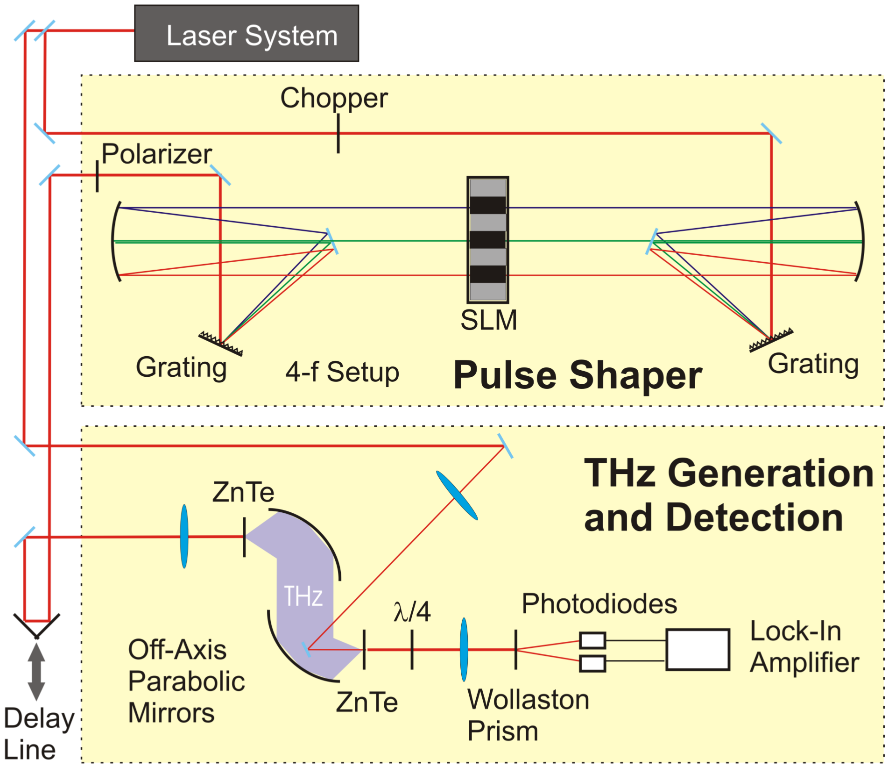

Figure 3.1: The THz time-domain setup with integrated pulse shaper. The frequency components of the pulse are arrayed in a line at the center of the pulse shaper by the grating-lens combinations. After setting the phase with the SLM, the pulse is reassembled by a mirrored arrangement of the grating-lens combination. The emitted THz radiation from the sample is collected, collimated and refocused onto a thin ZnTe crystal by a pair of gold coated off-axis parabolic mirrors. An electro-optical detection scheme is used to measure the THz field. A pair of balanced photodiodes is used to detect the slight deviation in the polarization that is proportional to the strength of the THz field. (From [86])

is then dependent on the processes under consideration. ZnTe and GaAs were chosen because they display large nonlinear coefficients for the respective processes.

A detailed schematic of the setup is given in Fig. 3.1. This section will focus on the THz part, the detailed description of the pulse shaper follows in section 3.2. For a phase shaping mask that is merely initialized, the output pulse is bandwidth-limited and the pulse shaper can be ignored for the moment. A sample THz trace and the accompanying spectrum are shown in Fig. 3.2

A Ti:Sapphire laser system (Spectra-Physics, Tsunami HP Advantage, tuning range (600 - 1100 nm)) is used to produce bandwidth-limited 90 fs pulses with a Full

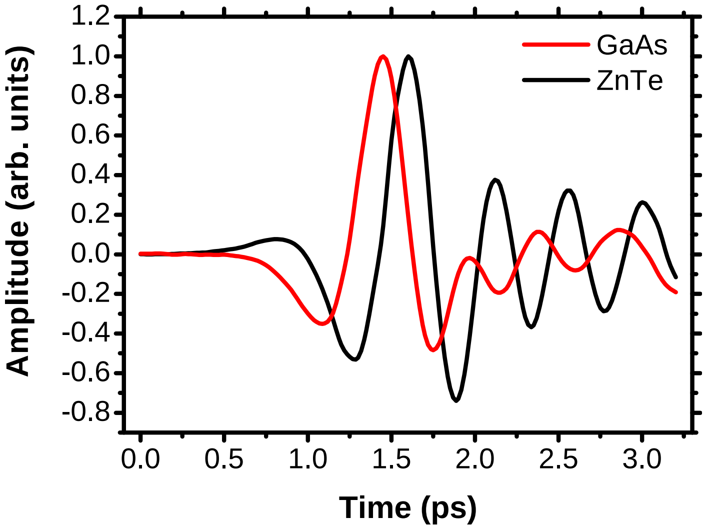

(a) Time-domain

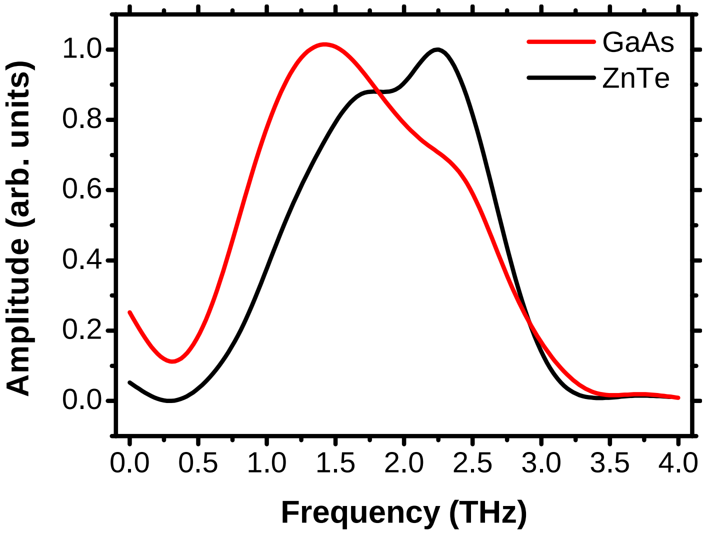

(b) Frequency-domain

Figure 3.2: Sample THz traces for shift and rectification currents.

Width at Half Maximum (FWHM) bandwidth of 10 nm at a wavelength of 800 nm with a repetition frequency of 80 MHz. The pump source is a continuous wave (cw) laser (Spectra Physics, Millennia) capable of providing up to 15 W of light at 532 nm.

The beam is split in two to provide light for the THz generation and detection. The generation pathway includes the pulse shaper and a mechanical delay stage that provides the temporal resolution to map out the THz trace. The pulse shaper requires p-polarized light, i.e., light with an electric field parallel to the plane of incidence. The polarizations of the emitted THz radiation from the shift and

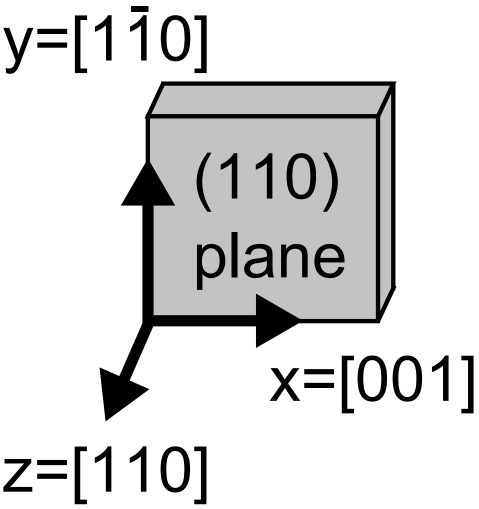

Figure 3.3: Sketch of the sample geometry of (110)-cut crystal.

rectification processes are perpendicular to each other. In order not to interfere with the detection arm, the polarization of the excitation pulse is changed to p-polarization for rectification, and s-polarization for shift currents. It is rotated by a $\lambda/2$ plate before the sample.

The THz radiation is generated at the focus of a 10 cm lens that provides spot sizes of approximately 300 $\mu$m. The radiation from the sample (either from ZnTe or from GaAs) is collected and collimated by a gold coated off-axis parabolic mirror with a focal length of 5.08 cm. The collimated beam is refocused onto a 1.0 mm thick <110>-cut ZnTe crystal. It co-linearly traverses the crystal with the optical beam from the detection pathway. The detection pathway must be of equal length as the generation pathway so that the interaction occurs with the original pulse. A Teflon plate is placed between the two parabolic mirrors which are positioned 10 - 15 cm apart from each other. This is necessary to block any remaining optical light that may have passed unconverted through the sample. Additionally, a THz polarizer can be introduced to select the polarization of the THz radiation. It was not used in the experiments, as the emitted THz radiation is polarized in a distinct direction. In other crystal geometries with different tensor elements, the relevant THz polarization needs to be filtered. A sketch of the sample geometry of a (110)-cut crystal is given in Fig. 3.3.

The beam used for the THz detection is focused onto the THz spot on the ZnTe crystal by a lens with a focal length of 70 cm, to ensure a comparable spot size. A small mirror is used to enable the precise alignment of the overlap, the single most important alignment step for this part of the setup. As long as there is an overlap, a THz waveform shall be visible. Alignment can be supported by swapping the sample with a thin piece of paper, where the scattering angle of the optical frequencies mimics the THz emission angle. Slight deviations from a circular form between the parabolic mirrors are excusable, as long as the spot on the ZnTe detection crystal is visible with the naked eye in the darkened room, and seems circular. Overlap between the two optical spots is then easily achieved.

Careful consideration must also be taken for the polarization of the detection beam. It has proven useful to maintain and refresh a p-polarization. A combination of $\lambda/2$ plate and polarizer is used to enable continuous control over the optical power of the beam.

THz detection is achieved by electro-optical sampling (EOS) [88], which utilizes the Pockels effect [35]. Here, an electrical field causes a change of the birefringence of the crystal, which is linear to the applied field. The THz and the optical beam co-propagate through a thin (1.0 mm) ZnTe crystal which absorbs the THz radiation. The optical beam continues through a set of polarizer and $\lambda/4$ plates after which it is circularly polarized. A Wollaston prism separates the two orthogonally polarized components that make up the circular polarization and guides them onto a pair of balanced photodiodes. The impinging light induces a current flow in the diodes that is detected by a lock-in detector. When idle, i.e., without an applied THz field, the difference in the current between the two diodes is set to zero. This is achieved by using the $\lambda/4$ plate to influence the ellipticity of the impinging light so that the two orthogonal components separated by the Wollaston prism have equal intensity. When the THz field is switched on, the field causes the birefringence of the ZnTe crystal to change slightly which in turn offsets the balance of the orthogonal polarized components. This difference in current is directly proportional to the applied THz field, as shown in [89]. By introducing a time delay between the THz and the optical pulse with the mechanical delay stage, the THz trace is mapped out.

Great care must be taken for the choice of the detection crystal, as the detectable bandwidth is dependent on the material of the crystal and its thickness. For applications with small bandwidths, a ZnTe crystal of 1.0 mm thickness is sufficient; the available bandwidth here lies in the range of 0.25 - 2.75 THz, see Fig. 3.2. A detailed analysis of the effect of the crystal properties will be given together with the description of the model in section 3.3 as this has to be considered there too.

## 3.2 The Pulse Shaper

Real-time control over the amplitude and phase of a laser pulse cannot be achieved by electronic means in the time-domain. Typical response times here are in the range of milli- and microseconds, which are orders of magnitude larger than the temporal FWHM of the laser pulse, in this case about 90 fs.

Fourier-transformation of the pulse into the frequency domain avoids these difficulties, as the description of the pulse now depends on the frequency. Here, the introduction of appropriate phase filters changes the shape of the pulse. An inverse Fourier-transformation translates these changes back to the time-domain.

A grating is used to separate the frequencies that make up the bandwidth-limited laser pulse. The grating sits in the focal plane of a parabolic gold mirror to collimate the diverging beam. The phase and amplitude manipulation will take place in the second focal plane. Using the same arrangement of the components in reverse, the original pulse is reassembled, completing the so-called 4f-setup.

The realization of the setup is shown in Fig. 3.4. The beam is set to p-polarization with a $\lambda/2$ plate, in order to maximize the throughput, as the gratings have a higher efficiency for p-polarized light. Additionally, a self-assembled beam expander consisting of a two-lens system increases the beam diameter from 2 mm

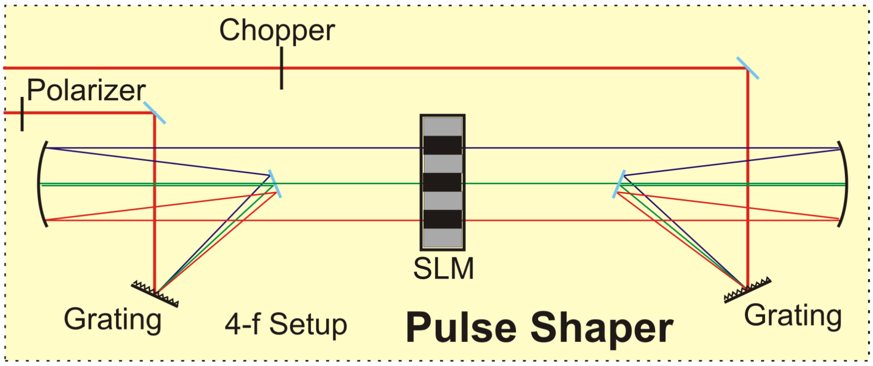

Figure 3.4: The frequency components of the pulse are arrayed in a line at the center of the pulse shaper by the grating-lens combinations. After setting the phase with the SLM, the pulse is reassembled by a mirrored arrangement of the grating-lens combination. When the polarizer is present the setup is used for amplitude and phase shaping, otherwise it is used for polarization and phase shaping.

to 8 mm. This was necessary to prevent damage to the gratings due to the high power of the oscillator.

The gratings (Newport) are gold coated with 1200 lines /mm blazed for a wavelength of 750 nm; the gold-coated parabolic mirrors have a focal length of 45.7 cm. The Spatial Light Modulator (SLM) sits in the Fourier plane and consists of two liquid crystal displays with 640 pixels each that enable independent control of amplitude and phase.

Using liquid-crystal displays as the primary pulse shaping device has introduced the much needed flexibility to use pulse shapers as self-learning machines. The liquid crystals are built out of long rod-shaped optically active molecules suspended in a liquid that are in a nematic phase, i.e., they possess a preferred orientation, which is susceptible to change when an electric field is applied. In birefringent materials the traversing light is split into an ordinary and an extraordinary beam, with orthogonal polarizations and differing indices of refraction. A change of the optical path length causes the addition of a phase, which is implemented here, by controlling the applied electric field [44, 90].

The use of two liquid-crystal displays enables independent control of amplitude and phase. They respectively are a function of the phase difference between the two displays according to

$$A = \cos\left(\frac{\Delta\phi_1 - \Delta\phi_2}{2}\right), \tag{3.1}$$

$$\phi = \frac{\Delta\phi_1 + \Delta\phi_2}{2}. \tag{3.2}$$

Here, $\Delta\phi$ is the phase-offset between the ordinary and the extraordinary beam.

The pulse shaper is completed by a polarizer that selects the propagating polarization component. In order to facilitate a high-power throughput the polarizer is set to filter the horizontal component. This enables a throughput close to 75% of the original power.

Figures of merit for a successful alignment of the pulse shaper are the spectral shape and phase of the pulse. Accessing the phase is especially challenging, as autocorrelator traces do not measure the phase. For this reason the commercially available APE Autocorrelator with the additional FROG option (APE Berlin) was procured. FROG stands for Frequency Resolved Optical Gating and is a smart solution for the problem. Instead of just measuring an autocorrelator trace and

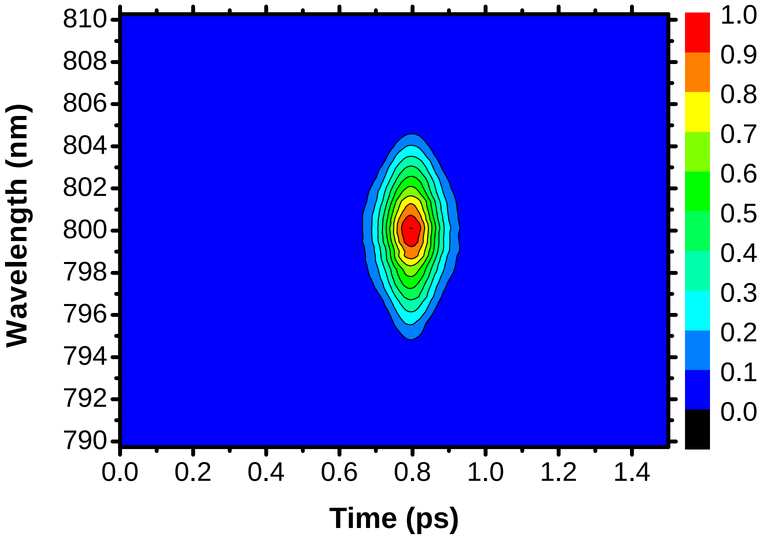

Figure 3.5: FROG trace of a bandwidth-limited laser pulse. Amplitude and phase are determined with a phase-retrieval algorithm, see Fig. 3.6.

including a spectrum, a spectrum is taken for each delay step of the autocorrelator trace. This two dimensional data structure is a unique and comprehensive representation of the laser pulse [81].

The phase is reconstructed by an iterative algorithm that calculates FROG traces

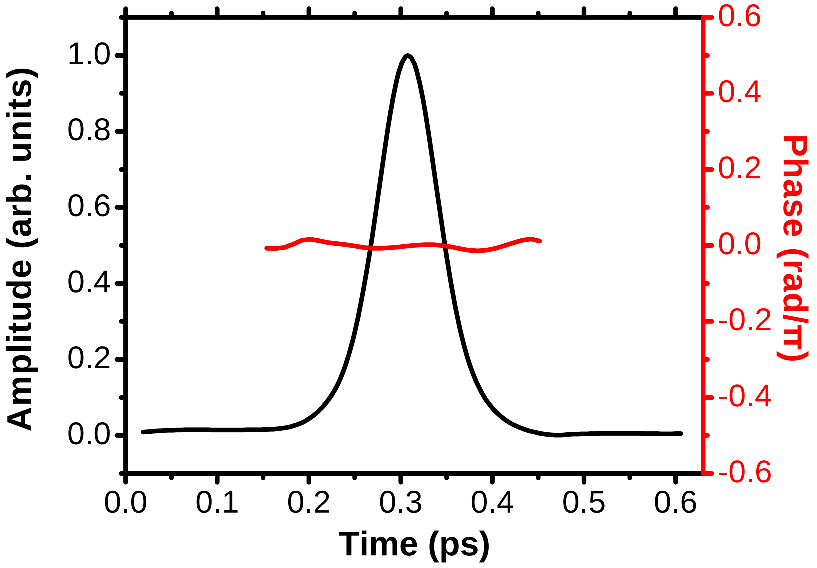

Figure 3.6: Amplitude and phase reconstruction of the bandwidth-limited laser pulse.

of different pulses, whose spectrum and spectral phase are known. Convergence is achieved when the difference between the calculated and the target trace falls below an appropriate threshold. As the phase of the final pulse is known, the problem is solved. It has been shown, that this so called two dimensional phase retrieval problem produces unique results that only differ by constant phases, which are not relevant [81].

Phase and amplitude of the pulse as shown in the FROG trace of Fig. 3.5 are successfully reconstructed in Fig. 3.6. The shape of the amplitude is not Gaussian, but is more accurately described by a secant-hyperbolicus shape, which is expected for the output of the laser system. The phase is depicted in red and is flat. This is proof of a successful alignment, as this implies a bandwidth-limited laser pulse.

Several attempts were made to incorporate automated phase retrieval mechanisms into the setup, as the APE Autocorrelator is not always suitable and useful. Especially problematic is the long acquisition time, which is detrimental for a self-learning machine. The most promising results were achieved with a GRENOUILLE setup (GRating-Eliminated No-nonsense Observation of Ultrafast Incident Laser Light E-fields), that enables real-time monitoring and phase-retrieval.

## 3.3 Modeling the System

Modeling the setup is straightforward, considering the reduction of the complicated term of equation (2.82) to the more practical terms in equations (2.97–2.99). An additional simplification is achieved by neglecting the dispersion of the tensor components of $\sigma$ and $\chi$. This is reasonable, as the bandwidth of our laser pulse is just 10 nm FWHM which corresponds to an energy bandwidth of 19.3 meV. Rapid changes of the dispersion are not expected in this region. The electric constant is also neglected as linear multiplications of constants are irrelevant.

In order to fully model the setup, the model must be able to accomplish several things.

1. Generate a pulse with enough data points for sufficient resolution.
2. Implement a pulse shaper and the requisite phase masks to replicate the experimental conditions.
3. Generation of the actual current density.
4. Determination of the pure THz field from the current density.
5. Emulation of the EOS process to determine the measured THz time-domain trace.

In light of these requirements, which are sorted according to the working order of the algorithm, it is advisable to start with a pulse in the frequency-domain. In deviation from the expected output from the experiment, a Gaussian pulse profile was used. The amplitude is expressed as

$$E(f) = \int \mathrm{d}f \, 2 \ln 2 \, \mathrm{e}^{-\left(\frac{f-f_0}{\Delta f}\right)^2} \tag{3.3}$$

with an initially flat phase to represent a bandwidth limited pulse, see Fig. 3.7. Central wavelength and the bandwidth of the pulse as determined by its FWHM are input in the more familiar nanometer units, but are converted to frequencies, for the Fast-Fourier Transform (FFT). The frequency window is constricted to a range of $1.15\Delta f$. This is sliced into the 1024 frequency components for which the calculation is performed. It is important to use a sufficiently large frequency window to ensure enough detail for the calculation of the current density.

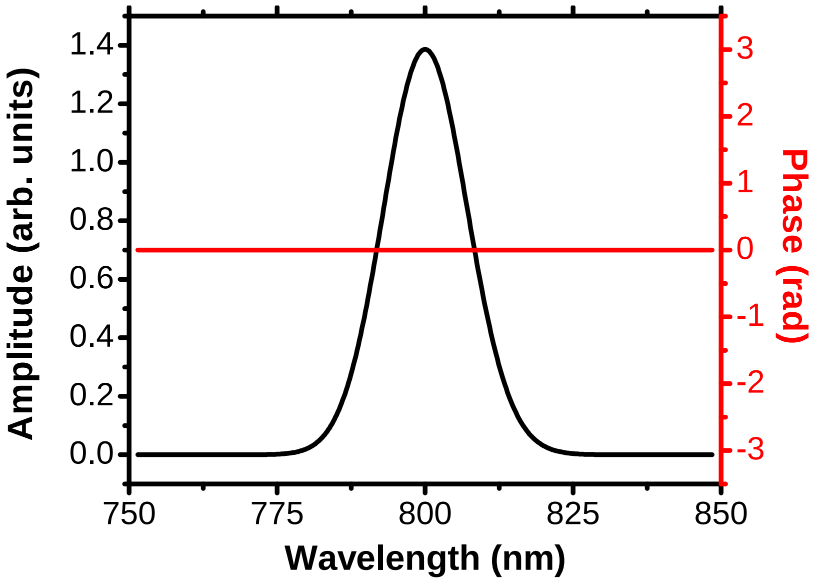

Figure 3.7: The initial bandwidth-limited pulse with a flat phase.

The convolution theorem turns the implementation of the pulse shaper and its masks in the frequency domain into a straightforward multiplication of the desired amplitude and phase modulations to the complex representation of the pulse

$$E_{\mathrm{out}}(f) = r\, e^{\mathrm{i}\phi} E_{\mathrm{in}}(f). \tag{3.4}$$

This is shown exemplary for the two phase masks that are employed in the experiments, the 2-color mask is presented in Fig. 3.8a, while the rectangular mask is depicted in Fig. 3.8b. Each major calculation step will be accompanied by a graphical display of the pulse envelope, its phase and the outcome of the operations.

The application of the phase to the pulse is achieved via an inverse Fast-Fourier Transform (iFFT) into the time-domain. This produces fast oscillating electric fields. Only the positive parts of the envelopes are shown in Fig. 3.9. The full shape of the field envelopes can be reconstructed by mirroring along the x-axis. These figures are not to be confused with autocorrelation traces. As autocorrelation traces are not the appropriate display format, FROG traces are presented instead. Fig. 3.10 illustrates how the manipulation of just the phase has an effect on the temporal as well as the spectral dimensions.

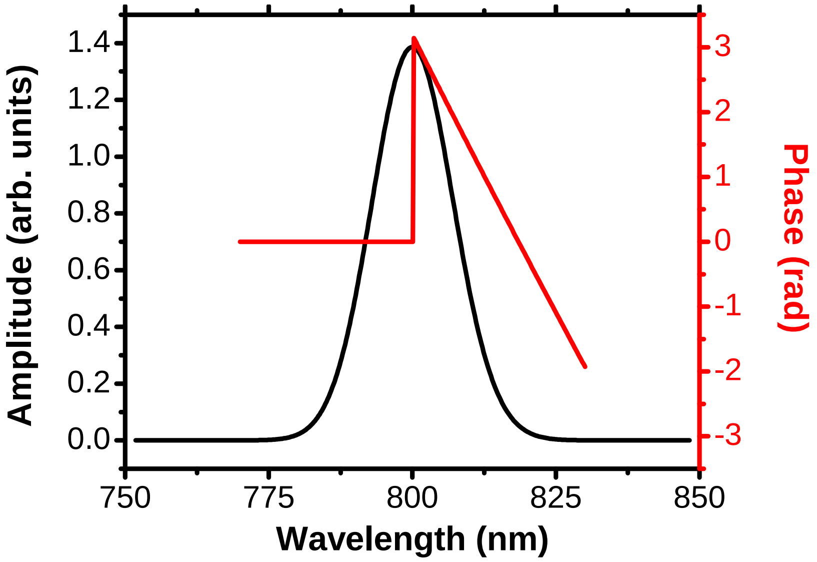

(a) 2-color mask

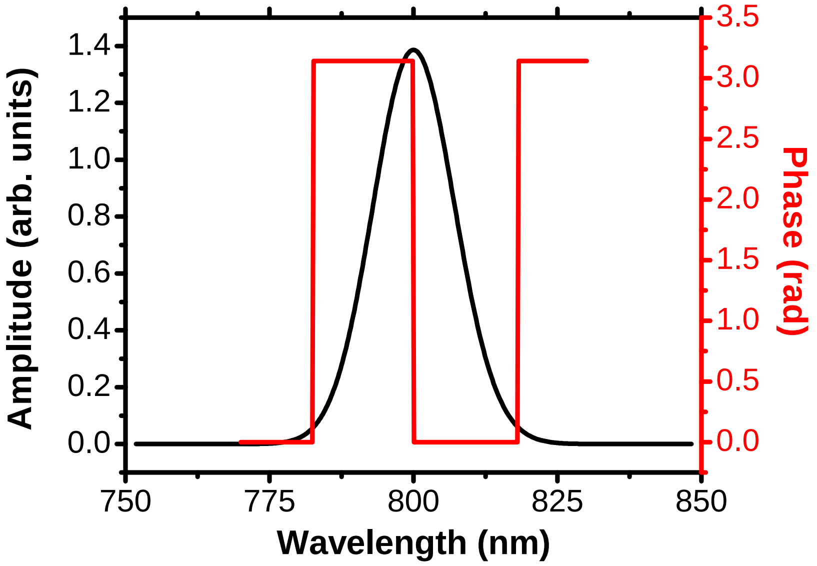

(b) Rectangular mask

Figure 3.8: Application of the two phase masks in the frequency-domain.

The current itself is calculated according to

$$J = E(t)E^*(t), \tag{3.5}$$

which considers all the second-order terms. In the experiment, the active process is selected by the phase matching condition, while here filtering is necessary. A FFT is performed and the results are displayed in Fig. 3.11a. The unfiltered result is depicted in black. The contributions of the other processes appear at higher

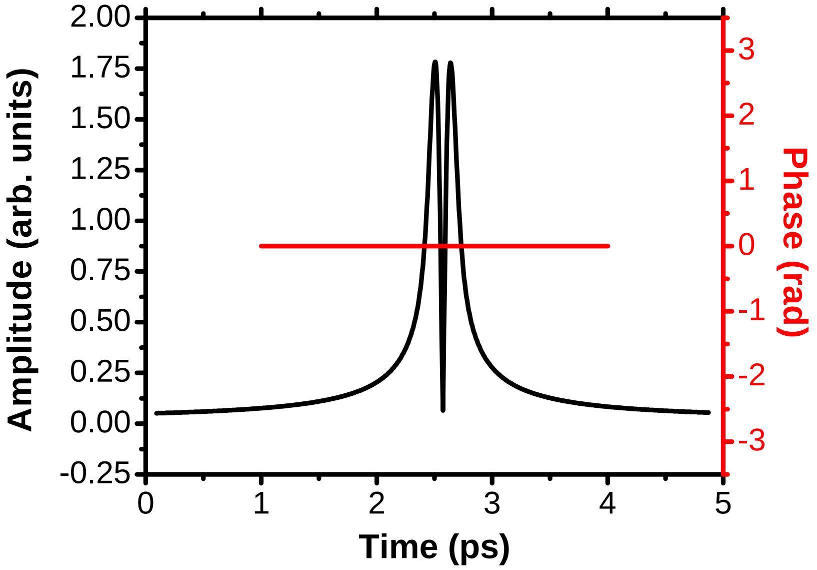

(a) 2-color mask

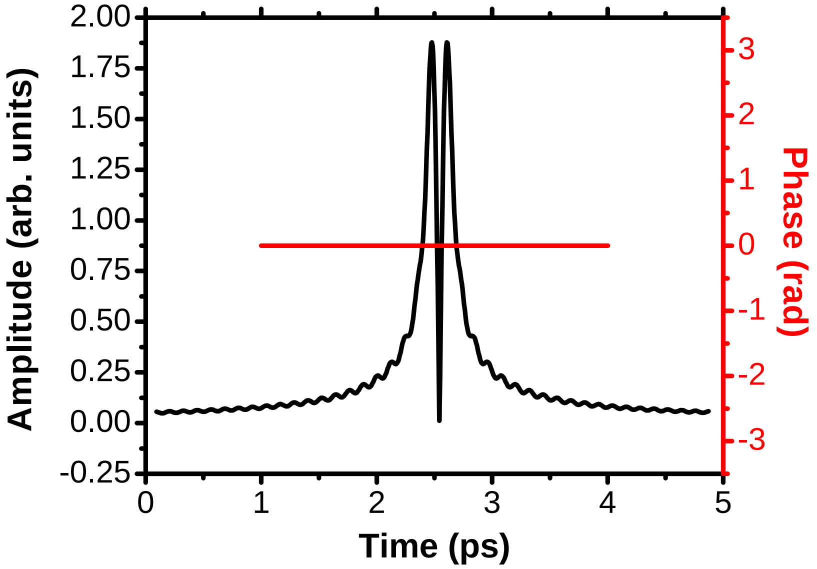

(b) Rectangular mask

Figure 3.9: Consequences of the phase masks in the time-domain: The emergence of a phase stable pulse pair.

frequencies. They are subsequently set to zero. An iFFT produces the Gaussian shaped current density, as pictured in Fig. 3.11b. The moving carriers produce an electric field, which leads to emission of THz radiation. The shape of the THz trace is generated by differentiation according to

$$E_{\mathrm{THz,\ shift}} = \frac{\mathrm{d}}{\mathrm{d}t} J, \tag{3.6}$$

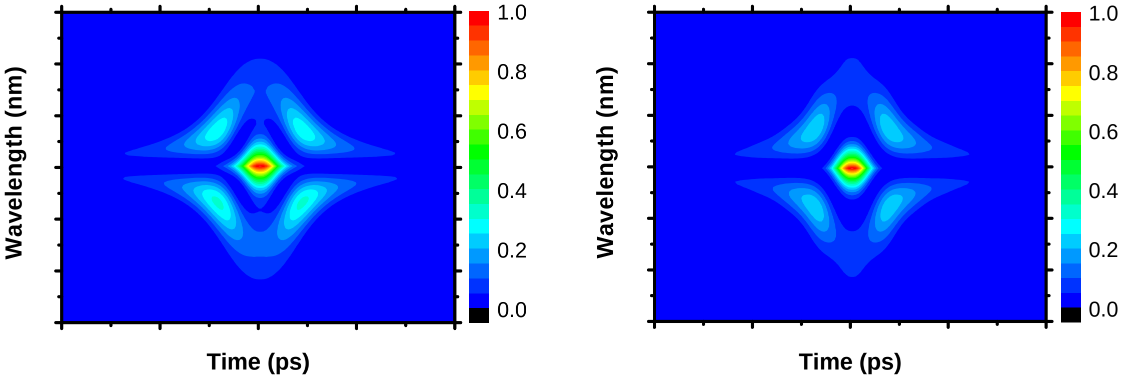

(a) 2-color mask (b) Rectangular mask

Figure 3.10: FROG traces of a laser pulse after application of a phase mask. The shape of the pulse envelopes must differ significantly from the bandwidth limited pulse in Fig. 3.5. Though they are created with distinctly different phase masks, at the time-separation presented here, the overall shape of the pulse envelopes are similar to each other.

for shift currents, while the second derivative is required for rectification currents

$$E_{\text{THz, rect}} = \frac{\mathrm{d}^2}{\mathrm{d}t^2} J. \tag{3.7}$$

The result is depicted in Fig. 3.12. These are the pure THz trace (Fig. 3.12a) and THz spectrum (Fig. 3.12b) before they are subject to the electro-optical sampling process. The measured THz waveform generated with the data from the rectification process would produce an inverted THz trace. To rectify this, the pure THz waveform is inverted before further processing. The unencumbered THz waveform possesses only a single cycle and spreads over 20 THz. Only setups with sufficient detection bandwidth will be able to measure this. The bandwidth of the ZnTe crystal in this setup extends to approximately 3 THz, which distorts the measured THz waveform. The electro-optical sampling process is modeled according to ref. [88], in order to replicate this limitation.

The goal is to recreate the frequency response function of the electro-optic sensor. As proposed in [88], the pulse and the THz wave copropagate through the crystal with a thickness $d$ and accumulate a Group Velocity Mismatch (GVM) (Fig. 3.13b), as their velocities differ. The time is given by

$$\delta(\Omega) = \frac{n_g(\lambda_0) - n(\Omega)}{c} d, \tag{3.8}$$

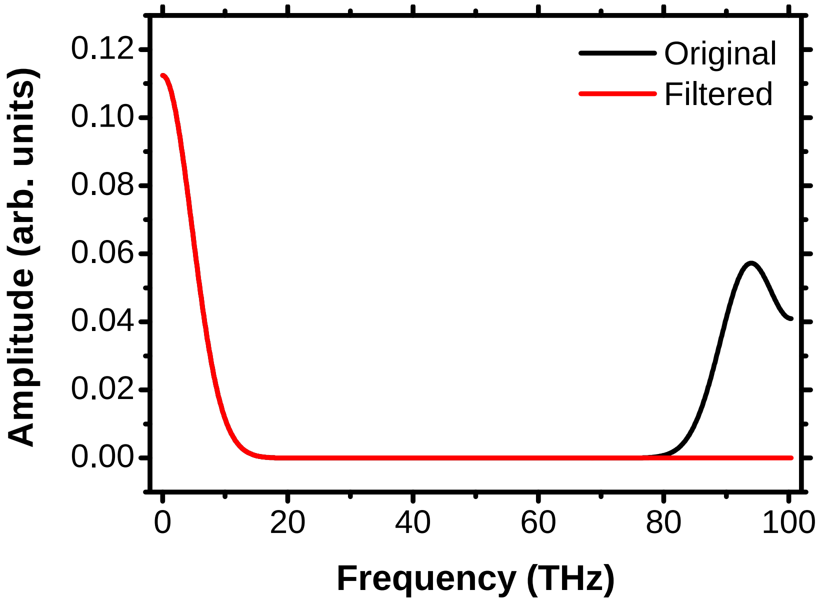

(a) Frequency-domain

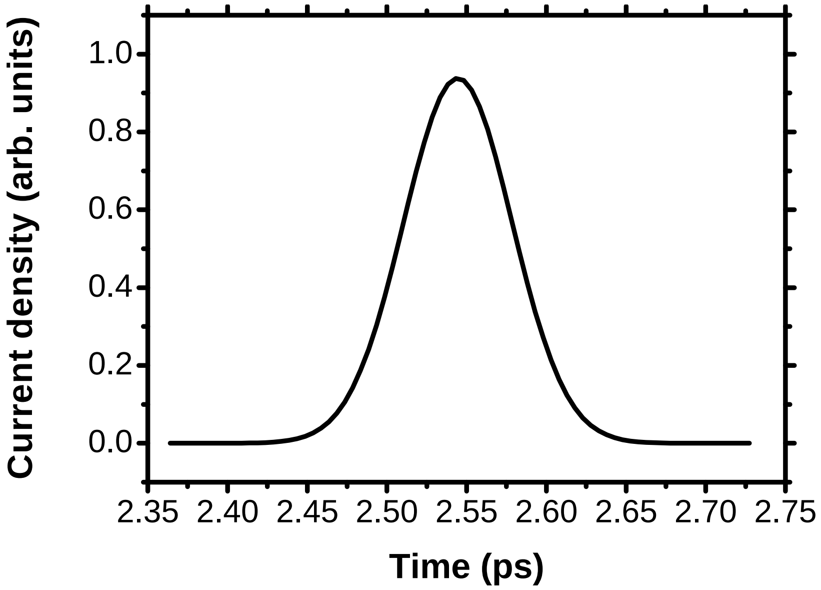

(b) Time-domain

Figure 3.11: The calculated current density in frequency and time-domain. Note the contributions of the other frequency mixing processes in the black curve in (a), which are filtered out to produce the red curve which is used to generate the current density in the time-domain.

where $n_g(\lambda)$ is the optical group index (Fig. 3.13a), that is calculated according

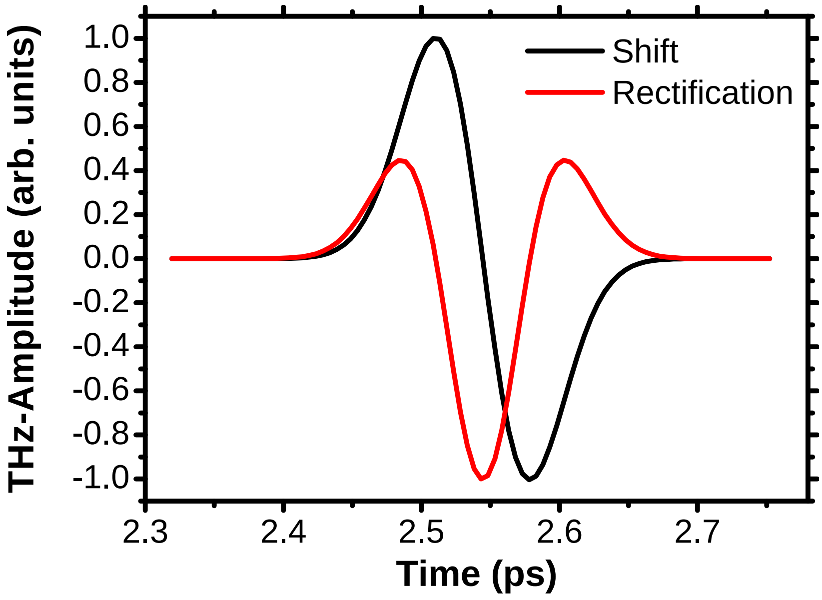

(a) Time-domain

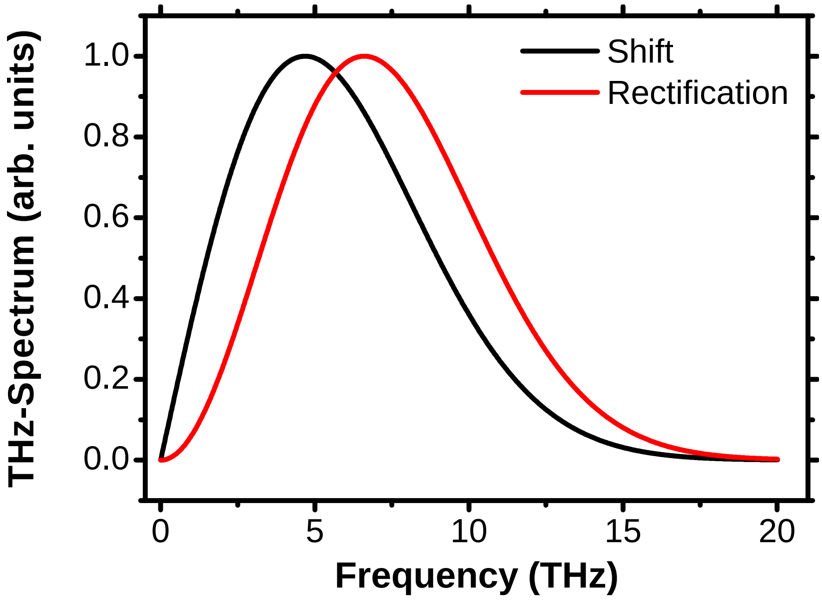

(b) Frequency-domain

Figure 3.12: The pure THz waveforms before consideration of the electro-optical sampling process. The two different current generating processes create distinctly shaped THz traces and spectra.

to

$$n_g(\lambda_0) = n(\lambda) - \lambda \frac{\partial n(\lambda)}{\partial \lambda}, \tag{3.9}$$

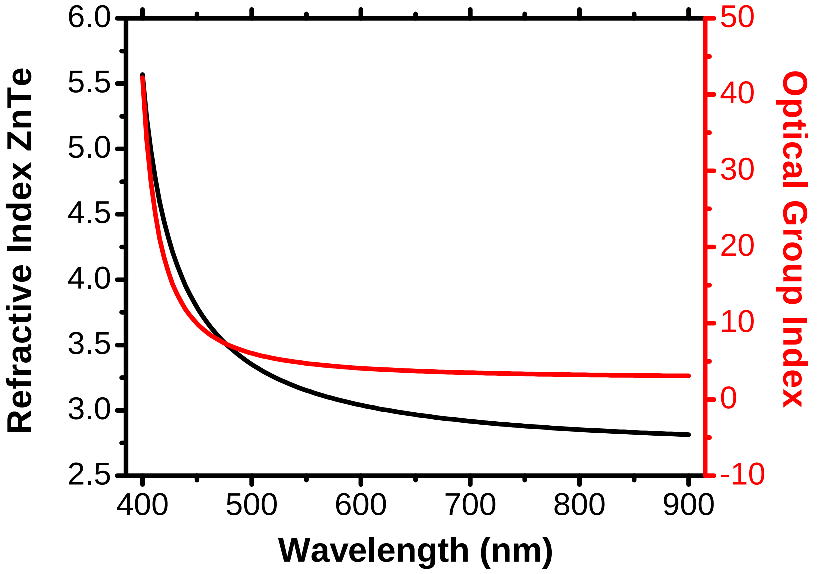

(a) Refractive index of ZnTe and the optical group index

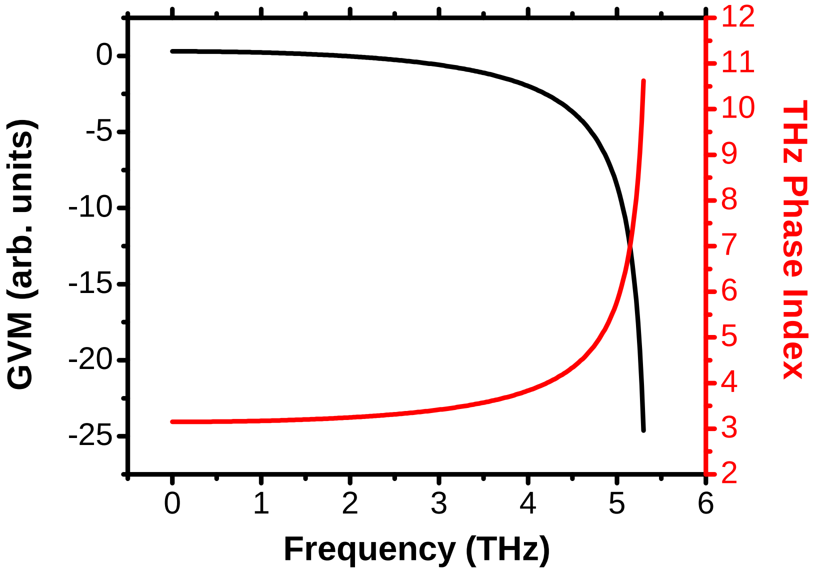

(b) GVM and the THz phase index

Figure 3.13: Miscellaneous functions that are used to model the electro-optical sampling process.

where the equation for the refractive index is taken from [91] (Fig. 3.13a):

$$n(\lambda) = \sqrt{\frac{3.01\lambda^2}{\lambda^2 - 0.142} + 4.27}, \tag{3.10}$$

with $\lambda$ in units of $\mu$m. The denominator precludes this formula from being useful

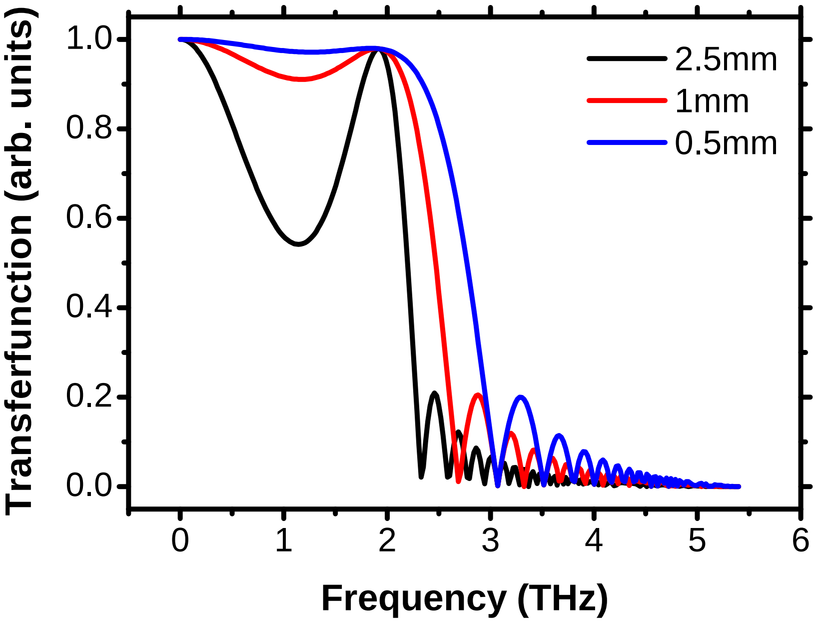

Figure 3.14: Transfer functions for various crystal widths that are used to consider the electro-optical sampling process.

for $\lambda < 0.376\,\mu$m. The THz phase index is given by (Fig. 3.13b)

$$n(\Omega) = \sqrt{\frac{289.27 - 6f_{\mathrm{Thz}}^2}{29.16 - f_{\mathrm{Thz}}^2}} \tag{3.11}$$

with the frequency in units of THz. The denominator again restricts the available bandwidth to 5.4 THz, but since the available bandwidth in the experiment only extends to about 3 THz this is tolerable,

$$f_{\mathrm{THz}} = \frac{\omega_{\mathrm{THz}}}{2\pi} \qquad \text{in [THz].} \tag{3.12}$$

The full frequency response is given by

$$G(\Omega) = \frac{t(\Omega)}{\delta(\Omega)} \int_0^{\delta(\Omega)} \mathrm{e}^{\mathrm{i}2\pi\Omega t}\,\mathrm{d}t \tag{3.13}$$

$$= t(\Omega)\frac{\mathrm{e}^{\mathrm{i}2\pi\Omega\delta(\Omega)} - 1}{\mathrm{i}2\pi\Omega\delta(\Omega)}, \tag{3.14}$$

and is depicted for various crystal thicknesses in Fig. 3.14. The $t(\Omega)$ is the Fresnel

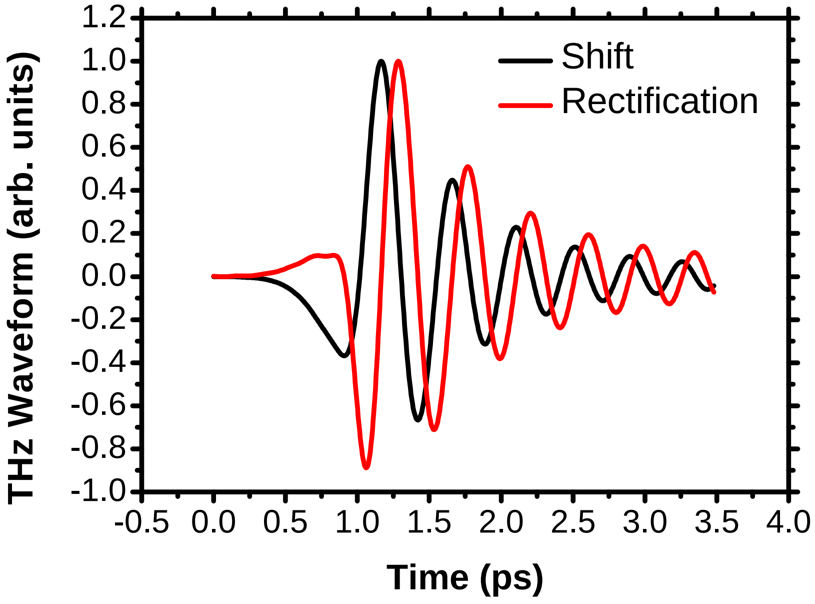

(a) Time-domain

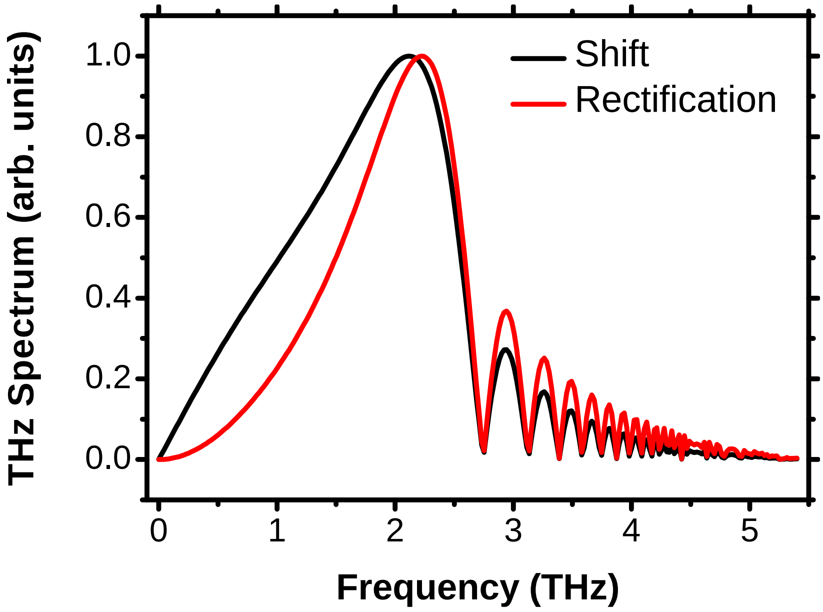

(b) Frequency-domain

Figure 3.15: THz trace and THz spectrum of shift and rectification currents after consideration of the electro-optical sampling process. The model faithfully reproduces the properties of the measured THz trace and spectrum.

transmission coefficient

$$t(\Omega) = \frac{2}{n(\Omega)+1}. \tag{3.15}$$

It is desirable to go to smaller crystal lengths, though this has a negative effect on the signal strength. The 1.0 mm thick crystal is a good compromise. The effect of the transfer function on the THz field and waveform of the shift currents are reproduced in Fig. 3.15.

The electro-optical sampling process emerges as the main source for the oscillations. This is due to the limited bandwidth of the detection sensor. The resulting THz trace is comparable to the measured one, presented above. Minor differences remain in the spectrum. This is not surprising, as none of the energy leeching processes are considered; still, the similarities prevail.

## 3.4 The Evolutionary Algorithm

Self-learning machines excel in solving problems where the solution is hidden in a vast solution space. The feedback loop establishes a memory mechanism which suddenly allows the machine to independently find a solution by leveraging the information from the past. This powerful tool is able to experimentally find solutions to complex problems which are difficult to model or where the optimal solution is unintuitive [92–94].

The algorithm at the center of the self-learning machine is a genetic algorithm. It borrows heavily from the concept of evolution. Here, a population of individuals tries to survive in an ecological niche. Two forces drive the development of the collective: selection and adaptation. The fittest will survive and thrive, while the inept will not. The offspring of the survivors are better adapted to the niche, by inheriting the most successful genes. Mixing the genes introduces new gene combinations. This protects against the frailty of a homogenized population.

The experiment can be described analogously. The ecological niche is the solution space, while the individuals are the parameters that describe the phase mask. The fitness of the individual is tested against its ability to reduce the oscillations following the main THz lobe.

In detail, the phase mask is used to influence the shape of the exciting laser pulse which induces the THz radiation. The parameterization of the phase mask can be done in three ways:

1. Take the full width of the phase mask and assign each pixel a random value in the interval $[0, 2\pi]$
2. Pick several points along the phase function and use these as building blocks for a continuous function.
3. Come up with a meaningful physical process that influences the desired outcome and parameterize accordingly.

The presented solutions are sorted by their convergence times. It is useful to consider the amount of parameters of each approach. The first proposition has 640 parameters, i.e., the number of pixels available in the mask, of which there are two. Each pixel can be independently set with 12 bit resolution. This translates to 4096 independent values. Therefore there are $1280^{4096}$ different combinations, i.e., individuals. This of course includes physically impossible solutions, which are conveniently avoided by the second approach. Using a continuous function avoids the impossible solutions, i.e., abrupt oscillations between 0 and $2\pi$ in adjacent pixels. This is a useful approach to take, when chirped solutions are sought. The best and most efficient way is of course to include information about physical processes most likely responsible for the effect. When trying to recompress a chirped pulse, a phase mask based on a Taylor function would be the most promising approach. In the presented experiment a second electric field is introduced into the setup. Solutions like this will not be found by the first two propositions in any usable time-frame. The second pulse, as proposed in the experiment, is created by using either the rectangular, or the 2-color mask. Both masks need only three parameters to determine their shape, thus characterizing an individual of the gene pool.

The algorithm works according to the following scheme, which is visualized in Fig. 3.16:

1. Initialize a population with randomly generated individuals. In order to shorten the conversion time, the parameter space is predetermined and restricted to a region with likely solutions.
2. Each individual is tested, in this case a THz trace is recorded and its fitness assessed. Its mean square error to a predetermined target trace is calculated for this purpose. Here, the target is dynamically generated from the recorded trace. This tolerates a gradual change of experimental conditions that might occur during run-time.
3. Sort the individuals according to their lowest mean square error and keep the best $x$%, where $x$ is available as a tuning parameter.
4. The selected individuals generate the new population by creating offspring through the available evolution operations: survival, mutation and recombination. The ratio of the operations is available as a tuning parameter.
    - **Survival:** It seems prudent to let the best performing individual survive. To keep it around as a safeguard against a future decline of the fitness. But this is a bad idea. It actually works against efficient convergence and might yield only locally optimized solutions.
    - **Recombination:** Here, the new individual is created by combining the genes from two randomly selected individuals either through mixing or through averaging.

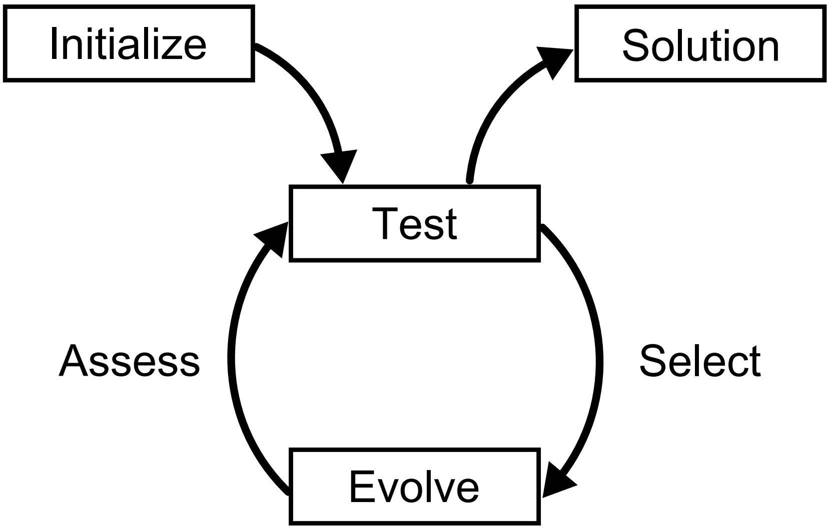

Figure 3.16: Schematic workflow of the evolutionary algorithm. First an initial population is created by choosing random values for the genes. Each individual is then tested, i.e., its associated THz trace is recorded. The individuals are then sorted according to their suitability to the task. The most promising candidates are then allowed to procreate using the three evolutionary operators that are described in the text. The circle of life is repeated, with a test of the newly formed generation, until an adequate solution is found.

- **Mutation:** The genome of one randomly selected individual is taken and a random selection of the genes is subjected to a modification by the mutation parameter. This is calculated by considering the allowed range of the value, a Gaussian distribution centered on 0 with a FWHM of 1, and the variance. The variance is used to control the impact of the mutation. It decreases if the process converges, and increases if it doesn't. This step size is controlled by the convergence parameter which is the value by which the variance increases or decreases. Both, the initial variance and the convergence parameter, are available as tuning parameters.

5. The new generation is tested and the circle is complete. The process is stopped when a convergence criterion is achieved.

The most critical component is the fitness function, as it is the figure of merit for the efficacy of the process. There are no limits to its complexity and even speed is no issue in this setup, as the slowest component is the actual recording of the THz trace. Penalties for strong deviations from the target trace assure the fast demise of the stray individuals.

Other critical parameters are the size of the population and the parameters that control the mutation and recombination rate and effect. Finding the right combination of these parameters to ensure convergence in adequate time is hard, and requires experience. It is especially difficult in this setup where the acquisition time is approximately 60 s for a single THz trace. With 42 individuals the test of a generation takes up to 45 min, making it difficult and time-consuming to discern the variation caused by the fine-tuning.

In effect, the used parameters were taken from trial runs done on the recompression of an artificially broadened laser pulse by inserting a thick slab of glass into the beam path. This inflicts second-order chirp on the pulse, which is balanced by a phase function based on a Taylor series. This only takes a few minutes and is a good test for the evolutionary algorithm and the self-learning system.

# 4 Coherent-Control of Shift and Rectification Currents

Shift and rectification currents as described by equations (2.98) and (2.99) depend on the shape of the envelope and on the time derivative of the optical pulse envelope of the exciting laser pulse. Several approaches were pursued to shape it. In a first effort the envelope shaping properties of chirp were examined. But as will become apparent, this approach is very limited in the amount of distinct phase shapes it is able to produce. The more promising idea is the addition of a second pulse and the use of the superposition principle. This enables real control over the shape of the pulse envelope and the resulting THz trace.

## 4.1 Chirped Laser Pulses

Direct influence on the envelope shape is provided only by the even chirp orders, which influence the length of the pulse. The uneven orders distort the electric field, but only influence the pulse length for very large values [81]. With this in mind, the effect of linear and quadratic chirp on the currents was investigated.

Chirp was applied to a bandwidth-limited pulse through the SLM. The phase mask was calculated according to the Taylor expansion of the phase as detailed in section 2.4. The physical limitations of the SLM restricts the values for the quadratic chirp to $\pm 1 \times 10^4\,\mathrm{fs}^2$, and for cubic chirp to $\pm 5 \times 10^5\,\mathrm{fs}^3$. Higher values lead to distorted pulses.

The experiment was conducted in the following way: The parameter space of the chirp is sampled in steps of $1 \times 10^3\,\mathrm{fs}^2$ and $2 \times 10^4\,\mathrm{fs}^3$, respectively. A THz trace is recorded for each step. The results are presented in 3D plots, where the THz traces are stacked and sorted along the y-axis according to their chirp value. A cut at any point along the y-axis reveals the corresponding THz trace, while a cut through the x-axis shows the evolution of the THz trace at this point in time for the chirp progression. The experiment was conducted on both GaAs for shift and

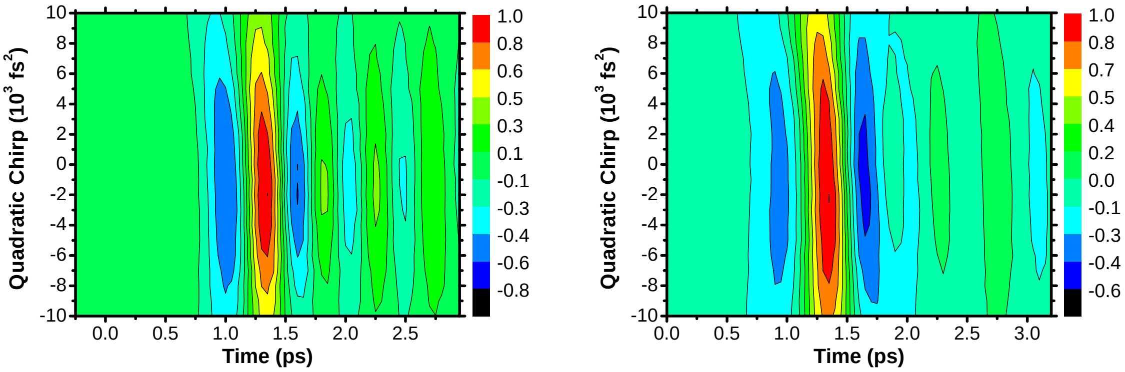

(a) Rectification current

(b) Shift current

Figure 4.1: Influence of the linear chirp on the THz emission (Experiment). The behavior of rectification and shift currents is comparable. Longer pulses create weaker THz pulses. Curiously, the THz amplitude is maximal not for the bandwidth-limited, but for negatively chirped pulses.

ZnTe for rectification currents. The plots for both types of currents are shown side by side for comparison.

### 4.1.1 Linear Chirp

Though the dependence on the pulse envelope of the respective currents is different, the behavior of the currents is comparable, see Fig. 4.1a for rectification and Fig. 4.1b for shift currents. Both exhibit a peak of the THz emission for negatively chirped pulses, which is odd, as it is usually assumed that the emission is maximal for bandwidth-limited pulses with a flat phase. This assumption is corroborated by the model, see Fig. 4.2a for rectification and Fig. 4.2b for shift currents. Here, the peak emission is indeed obtained for the bandwidth-limited pulse.

This deviant behavior is understood if the pulse is assumed not to be bandwidth-limited. But alignment of the pulse shaper is rigorously checked and the pulse is in fact bandwidth-limited, as shown in Fig. 4.3.

The additional negative chirp is not reproducible by the model. It thus must be attributed to either an inherent process not considered by the model or to the FROG, which would lead to an inaccurate alignment regarding chirp. The latter explanation is supported by the chirp map, which is useful as an additional sanity check, see Fig. 4.4. Here, the intensity of a SHG process in a thin BBO crystal (100 $\mu$m) is used as a sensor for the pulse distortion due to phase effects.

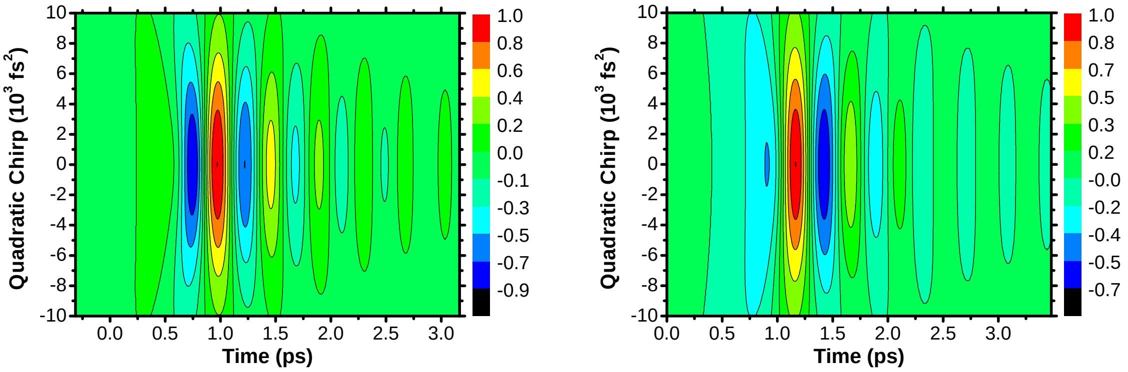

(a) Rectification current

(b) Shift current

Figure 4.2: Influence of the linear chirp on the THz emission (Model). The model corroborates the experimental data, but in contrast to the experiment peak THz emission is obtained for the bandwidth-limited pulse.

The strongest signal is generated by a bandwidth-limited pulse and decreases as additional phase distortions are applied. Since the principle effect of a phase is impartial to the sign, a highly symmetric shape is expected.

The experimental result unfortunately is not entirely symmetric. It deviates especially for high positive cubic phase values though a peak is still obtained for the bandwidth limited case. This finding is very puzzling, since this means, that

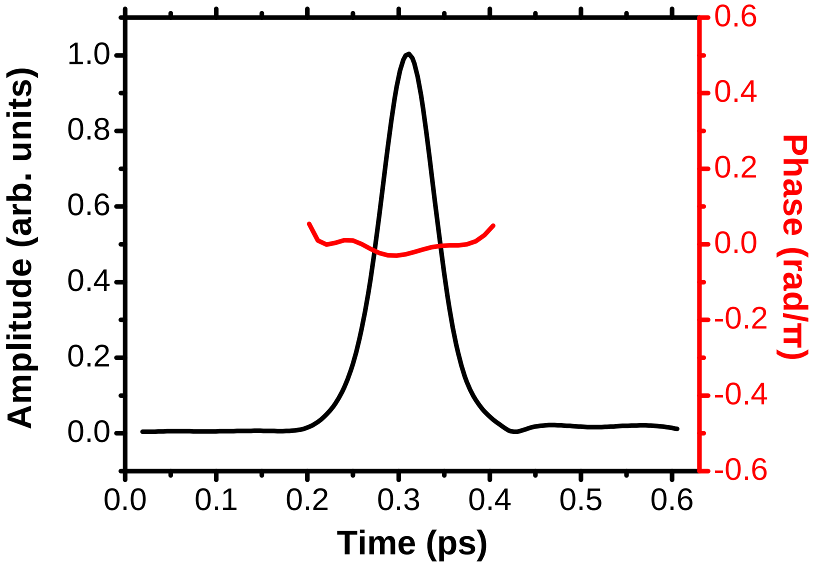

Figure 4.3: Bandwidth-limited pulse, i.e., with a flat phase, as reconstructed from a FROG trace.

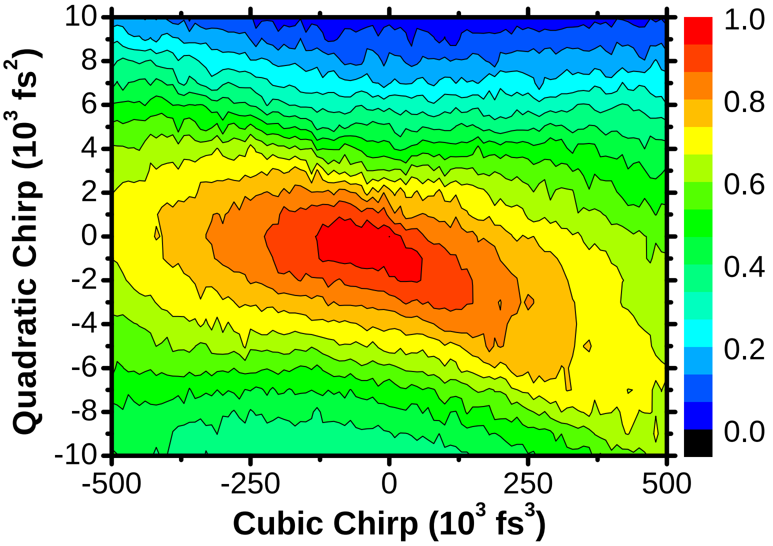

Figure 4.4: The accuracy of the applied chirp is most easily visualized by a chirp map. Linear and quadratic chirp is applied and the SHG signal of a thin crystal is recorded. The strongest signal is expected for bandwidth-limited pulses, which decreases when additional chirp is applied. In contrast to the highly symmetric shape that was expected, we see this lopsided shape with deviations for high positive cubic phase values. The origin of this behavior is not yet clear, but it will have to be investigated whether this is an alignment issue.

a flat phase is not a suitable indicator for bandwidth limitation, as it could still mask higher order distortions. Further investigations into this phenomenon will reveal whether this is an alignment issue. Theoretically a phase mask could be used to offset this strange behavior and produce the symmetrical shape. It would be interesting to see how this corrective measure would then interfere with the other figures of merit.

Apart from the slight chirp distortion, the behavior of the currents is accurately reproduced by the model. This warrants a look at the underlying current as generated by the model. The derivation in section 3.3 has shown, that the THz traces for the two processes are generated through derivation of the current density. Therefore, the underlying current density is independent of the underlying generation process. As expected, it follows the pulse profile and broadens as the pulse length increases, see Fig. 4.5.

The development of the real THz field is of particular interest. The limited bandwidth of the electro-optical sampling process usually prevents its observation, see section 3.3. The increasing pulse length leads to a restrained field that even-

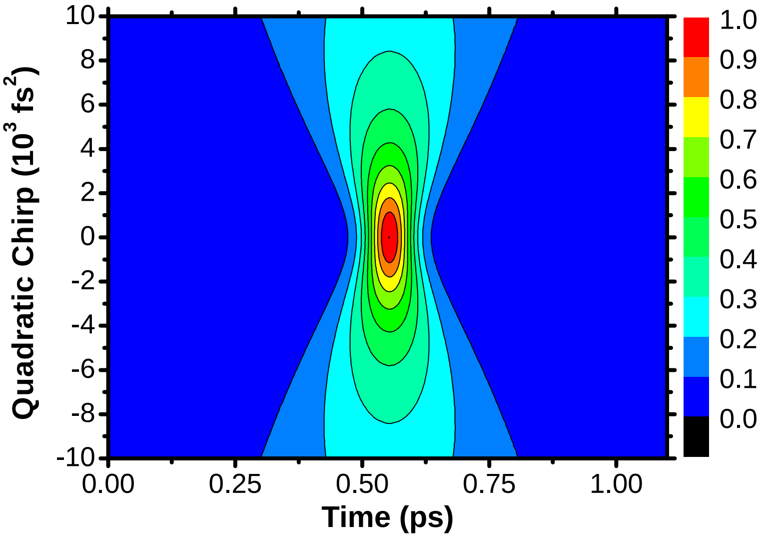

Figure 4.5: The current density follows the pulse profile and broadens as the pulse length increases through application of linear chirp.

tually lies completely within the bandwidth provided by the detection crystal. The behavior of the two actually different currents is indistinguishable in the model, therefore this will only be shown for shift currents in GaAs, but it applies equally for rectification currents in ZnTe.

Fig. 4.6a includes measured THz fields after considering the limited bandwidth of the EOS process for three chirp cases ($0\,\mathrm{fs}^2$, $1 \times 10^4\,\mathrm{fs}^2$, $1.8 \times 10^4\,\mathrm{fs}^2$). The THz traces of Fig. 4.6b approach the single-cycle regime, as the bandwidth of the real THz field falls below the ringing threshold. Regrettably, the emission intensity of the long optical pulses is reduced by two orders of magnitude.

Altogether, it is almost impossible to reproduce these considerations with our setup, as the SLM cannot produce chirps higher than about $1 \times 10^3\,\mathrm{fs}^2$, and even if this amount of chirp were applied through other means the intensity drop-off will make it very difficult to detect anything. Nonetheless, there is a suitable proof that a bandwidth constriction of the real THz field will lead to THz traces that approach the single-cycle regime.

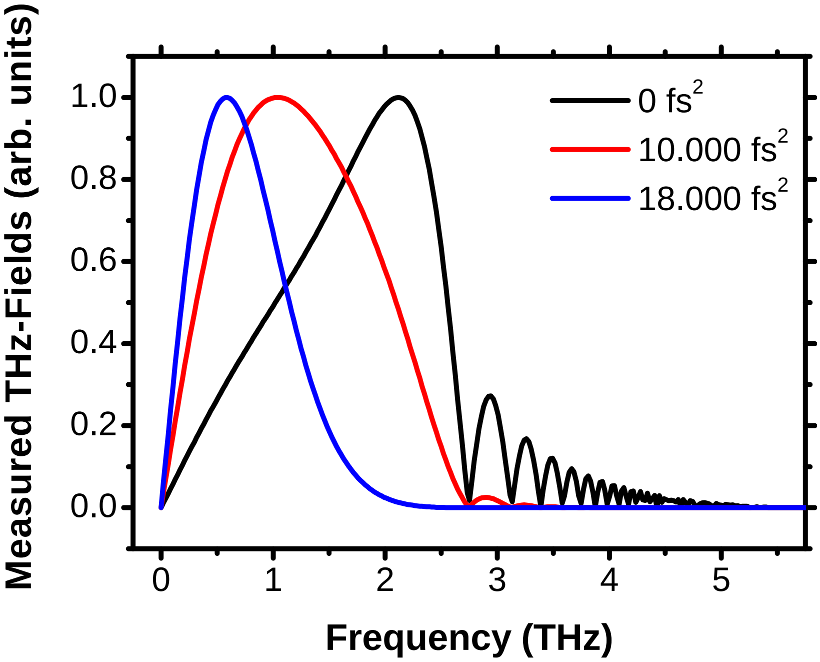

(a) THz spectrum

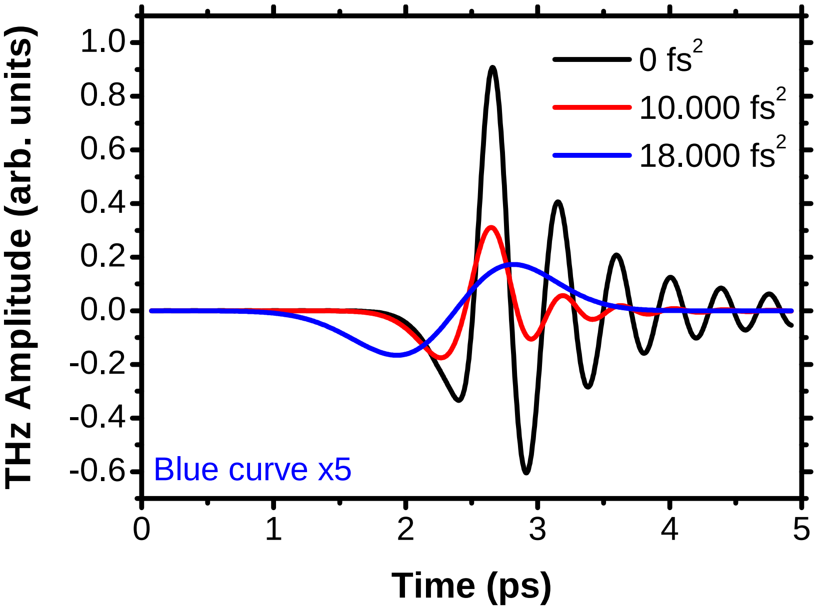

(b) THz waveform

Figure 4.6: Influence of high linear chirp on the THz spectrum and THz trace. Very high chirp produces a narrow spectrum that therefore incurrs no distortions due to the electro-optical sampling. The corresponding THz traces then approach the single-cycle shape.

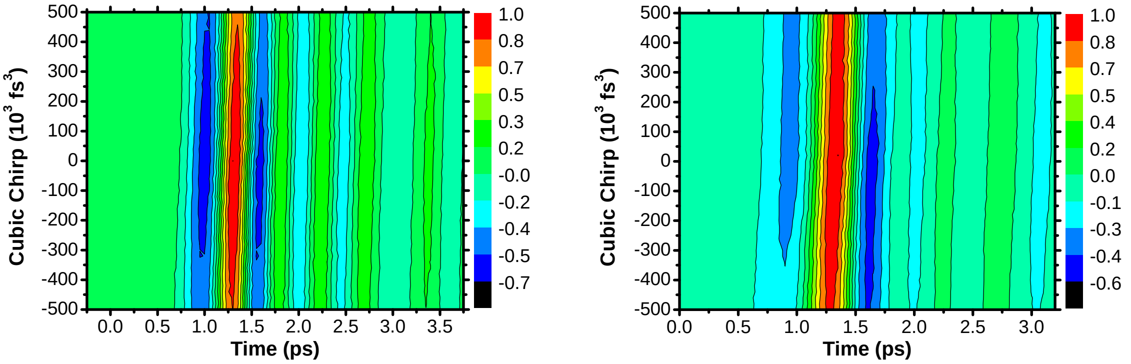

(a) Rectification current

(b) Shift current

Figure 4.7: Influence of the quadratic chirp on the THz emission (Experiment). Quadratic chirp has almost no influence on the shape of the pulse envelope. The emitted THz radiation therefore will exhibit little phase dependence. The THz peak amplitude in the experiment remains nearly constant over the range of the applied chirp values.

### 4.1.2 Quadratic Chirp

Quadratic chirp exerts little if any influence on the shape of the pulse envelope, thus no phase dependence is expected. The experimental findings confirm this and are presented in Fig. 4.7a for rectification and Fig. 4.7b for shift currents.

The main THz peak in both samples remains nearly constant over the range of the applied chirp values, see Fig. 4.8a for rectification and Fig. 4.8b for shift currents. The entire THz trace acquires a chirp-dependent time shift which is accompanied by a slight shift in the onset and decline of the first and second dip of the THz trace, respectively. It is more pronounced in the case of the shift current.

Several of the main features of the experiment are replicated by the model, see Fig. 4.8. The intensity of the main THz peak stays constant for the chirp variation. The shift of the dips is also visible, and is also more pronounced for shift currents. While the chirp dependence of the rectification currents is accurately described by the model, this does not hold for the case of shift currents. The variation in the THz peak strength is not as pronounced in the experiment, as it is in the model. It is therefore difficult to attribute this difference solely to the observed chirp disparity.

The current as presented in Fig. 4.9 provides the explanation for the discussed features. The time shift of the THz trace is a direct result of the time shift experienced by the current. The symmetry properties of the third-order phase changes

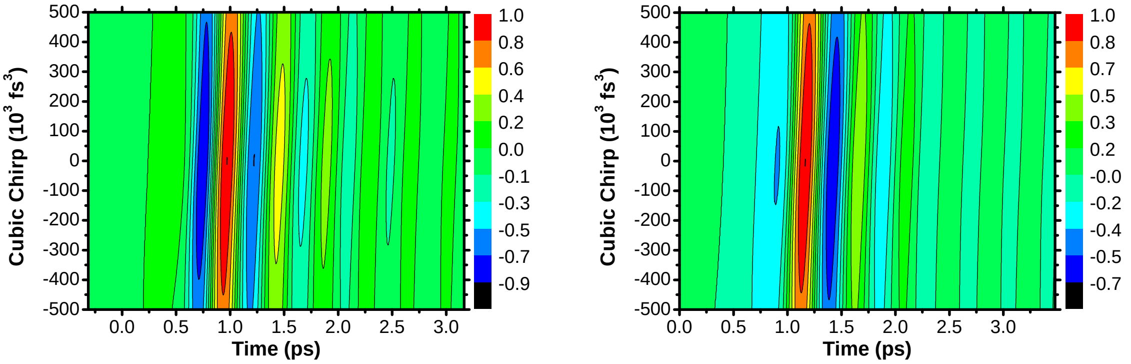

(a) Rectification current

(b) Shift current

Figure 4.8: Influence of the quadratic chirp on the THz emission (Model). The model corroborates the experimental data. The emitted THz radiation exhibits little phase dependence. The THz peak amplitude in the model remains nearly constant over the range of the applied chirp values.

the previously observed mirror symmetry of the current in the case of the second order phase to a point symmetry. The change of the oscillatory substructure stems again from a shift of the main peak in the real THz field. It moves to lower frequencies for higher chirp values. This causes the oscillations to vary which is

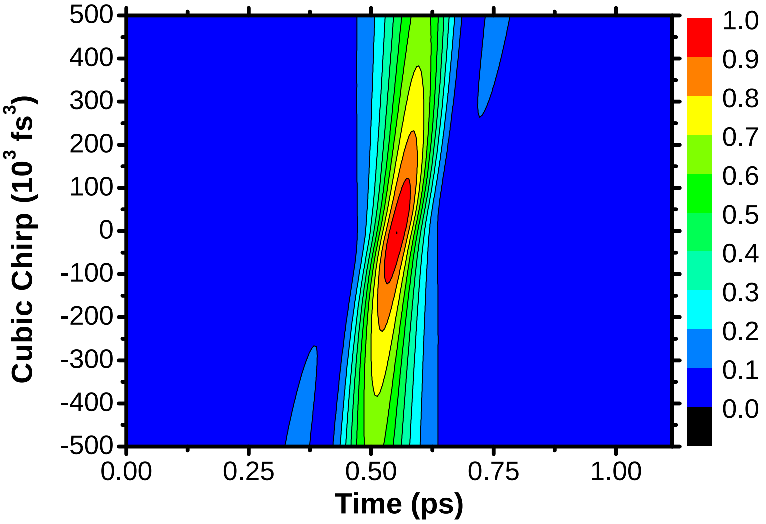

Figure 4.9: The current density follows the pulse profile. As the influence of quadratic chirp on the pulse envelope is negligible, the only interesting feature of the current density is the symmetry change from mirror to point-symmetric that is linked to the third order of the phase. For very high chirp values a secondary peak becomes visible which has no effect on the shape of the THz trace.

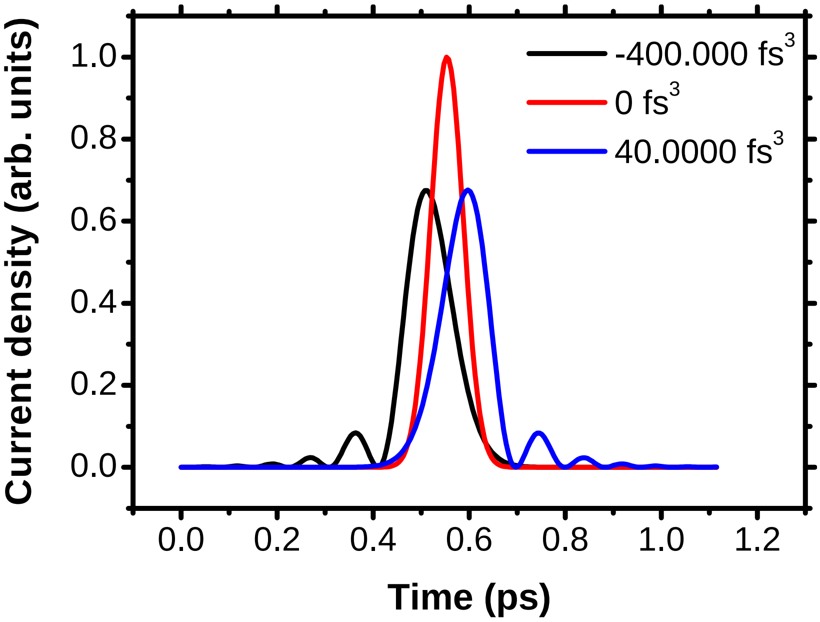

Figure 4.10: A secondary peak becomes visible in the current density for very high chirp values. It has no effect on the shape of the THz trace.

visible as the chirp dependent onset and decline of the first and second dip. A secondary peak becomes visible for very high chirp values, but has no effect on the shape of the THz trace, see Fig. 4.10.

This concludes the chirp based experiments. It has been demonstrated, that chirp influences the pulse envelope and thus also the THz trace. This is visible in both the time as well as the frequency-domain. This approach was not pursued any further, because the design possibilities of the chirped pulses are very limited.

## 4.2 The Pulse-Envelope Shaping Properties of Pulse-Pairs

It has become evident, that the more appealing approach is the introduction of a second pulse into the setup. The ensuing superposition of the pulses has more degrees of freedom that control the shape of the pulse envelope and thus have an effect on the THz trace. Introducing a second pulse into the setup usually requires a Michelson interferometer to stabilize and control the relative phase between the two pulses. Apart from the relative phase, the interferometer allows control over the temporal separation of the two pulses.

An equivalent situation can be generated with a SLM-based pulse shaper. A special phase mask creates the pulse-pair with a stable relative phase between the two pulses. Additional distortions to the pulse envelope can be integrated directly. One caveat remains: A second pulse with a wavelength not already present in the pulse cannot be introduced this way. Apart from this, the pulse shaper is a very versatile tool to control and shape the pulse envelope.

### 4.2.1 Experimental Implementation

Two phase masks were used in the experiment. They are named the ’2-color’ (Fig. 4.11) and ’rectangular’ (Fig. 4.12) phase masks. Both turn the initial pulse into a phase-stable pulse-pair. These patterns enable control over three degrees of freedom:

1. The absolute phase $\phi_0$, set by the offset between the constant and the sloped part in the 2-color, and by the amplitude in the rectangular mask.
2. The temporal separation between the two pulses $\tau$, set by the slope in the 2-color, and by the period of the rectangular function in the rectangular mask.
3. The energy distribution between the two pulses, set by shifting the discontinuity at the center in either direction.

While $\tau$ is easily set in the 2-color mask by adjusting the slope, this property needs to be calibrated for the rectangular phase. The time separation for various $\tau$-settings was measured with an autocorrelator. It is represented by the slope of the fit of a line with a forced zero-crossing at $\tau = 0$.

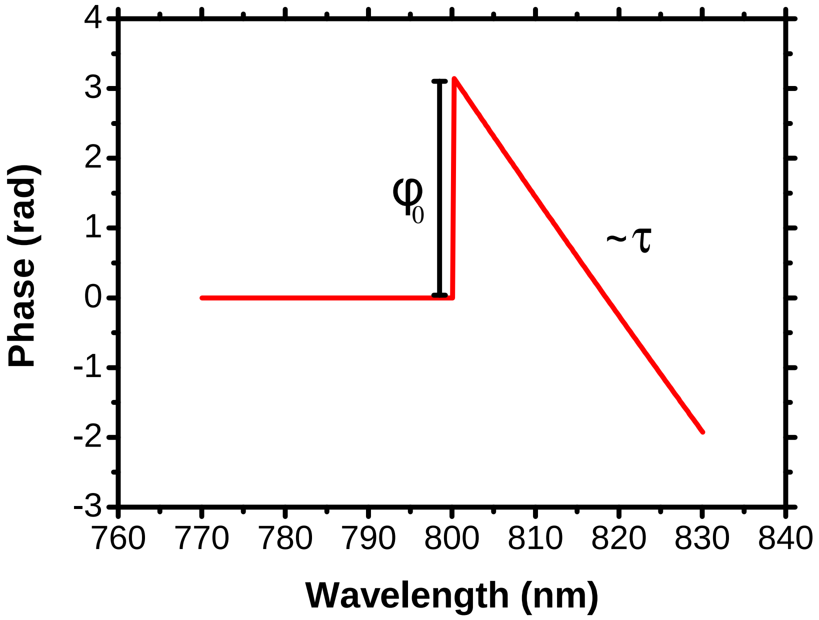

Figure 4.11: Introduction of the 2-color phase mask as used in the experiment. Three degrees of freedom are available: The absolute phase, the temporal separation and the energy distribution between the two pulses.

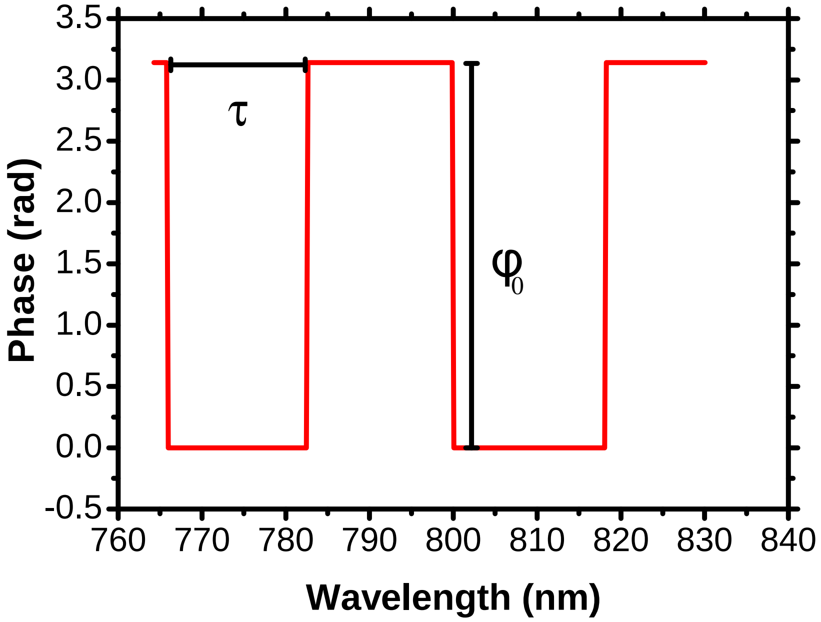

Figure 4.12: Introduction of the rectangular phase mask as used in the experiment. Three degrees of freedom are available: The absolute phase, the temporal separation and the energy distribution between the two pulses.

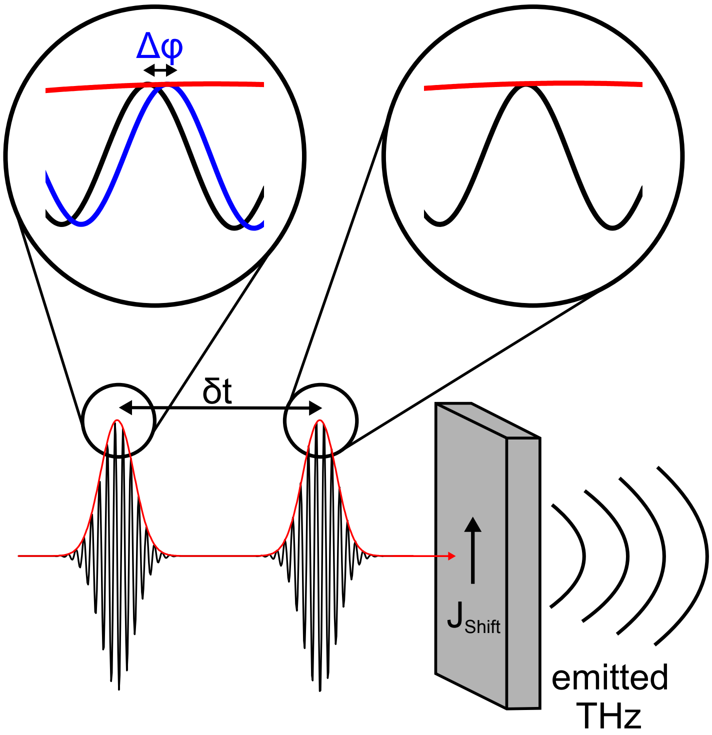

Figure 4.13: Visualization of the control over the relative carrier envelope phase in the phase-stable pulse-pair. The blue curve in the second pulse signifies the shift of the second electric field relative to the first, that is set through the absolute phase. This has significant influence on the shape of the pulse envelope.

Peculiar about these points of influence is the absolute phase. It usually plays no role in the description and handling of pulses on the time scales used here. It describes the phase offset between the pulse envelope and the underlying electric field. At 800 nm for pulse lengths of 100 fs, there are 37 oscillations of the field under the envelope. A slight offset is therefore negligible and undetectable. For short pulses with only a few oscillations however, this is a significant effect and requires sophisticated equipment to stabilize [95–97].

The pulse pair is constructed as a superposition of two electrical fields. While the exact position of the fields relative to the envelope remains arbitrary, the two fields are detunable with respect to each other through the absolute phase. This is highlighted in Fig. 4.13. The current generation process is indicated by the THz radiation emitted from the crystal. The time delay of the incident phase-stable pulse-pair is exaggerated, though due to the superposition principle the interference term should still have some significance even for separation times larger than double the FWHM. The blue curve in the second pulse signifies the

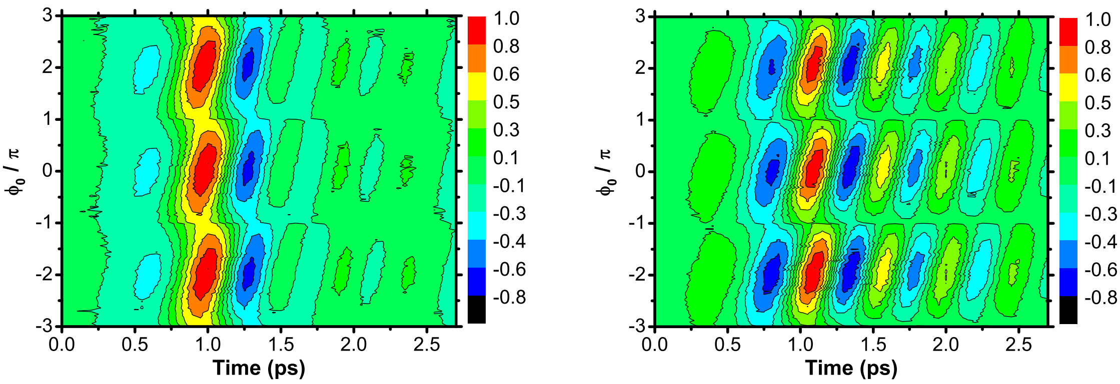

(a) Shift current

(b) Rectification current

Figure 4.14: Phase dependence of rectification and shift currents for the rectangular phase mask set to $\tau = 60\,\text{fs}$ (Experiment). The oscillatory pattern is clearly visible. It depends on the shape of the pulse-pair-envelope that is set through the absolute phase.

shift of the second electric field relative to the first. Consequently the pulse envelope depends on the detuning of the fields. As a pure phase effect, it is expected to behave with an oscillation modulo $2\pi$.

The experimental implementation is the same as above. A time separation is set, and the absolute phase is sampled in 201 steps between the boundary values of $-3\pi$ and $3\pi$. A THz trace is recorded for each value of the absolute phase. The results are presented in a stacked 3D plot. Two phase masks and two samples were investigated at two separate time delays for comparison.

First, the traces generated by the rectangular mask are presented. The temporal separation of the pulse pair is set to 60 fs. This time is to be understood as the separation of the pulse-envelope peaks for an absolute phase of $\phi = 0$. The graph for GaAs is in Fig. 4.14a, the one for ZnTe in Fig. 4.14b.

An oscillatory pattern emerges as predicted. It possesses a period of $2\pi$ and is based on the phase relationship postulated above. The oscillations stem from the dependence of the emitted THz radiation on the manipulated pulse envelope. The phase variation introduces an additional time delay to the THz traces. This is evident by the tilt of the peak positions. There are no apparent material related differences in the depicted behavior. The oscillatory substructure is more pronounced in ZnTe. The oscillations extend to the whole THz trace and not just to some of its features. This behavior might therefore be connected to the real THz field, as introduced above.

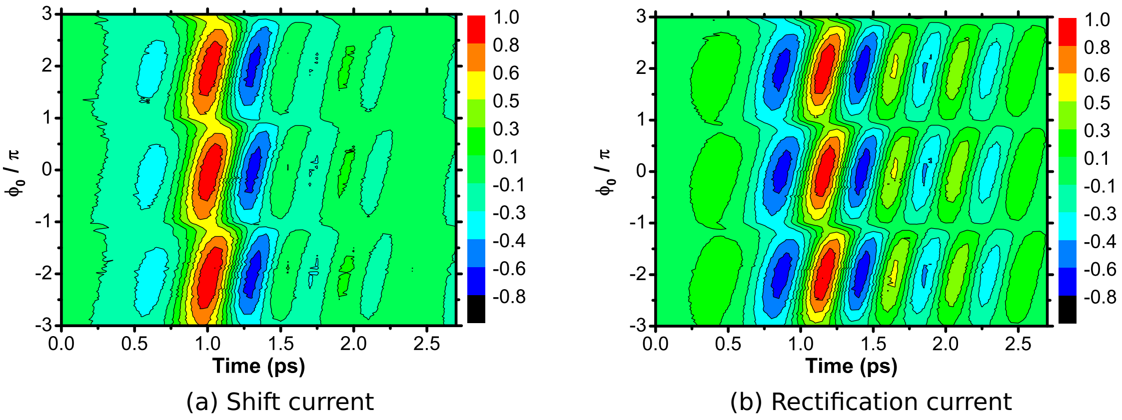

(a) Shift current

(b) Rectification current

Figure 4.15: Phase dependence of rectification and shift currents for the 2-color phase mask set to $\tau = 60\,\mathrm{fs}$ (Experiment). The pattern is nearly indistinguishable from the one generated with the rectangular phase mask. The additional wavelength shift of the 2-color phase mask plays no role here.

The properties of the 2-color phase mask are investigated next. The graphs are nearly indistinguishable from each other for these time delays, see Fig. 4.15. The two phase masks produce similar phase envelopes, and the wavelength shift of the 2-color mask plays no role here. Looking back at the modeled pulse envelopes and FROG traces introduced in Fig. 3.10, this is not surprising, as only minute variations of the substructure are discernible here.

The influence of the superposition principle is visible for large temporal separations, i.e., for $\tau = 200\,\mathrm{fs}$, see Fig. 4.16. First, the effects of the rectangular phase mask are discussed. The shape of the stacked THz traces reveals an oscillatory pattern, but also shows remarkable distinctions from the 60 fs case. As the separation is larger than the FWHM of either pulse, the fact that it still produces the familiar $2\pi$ pattern is proof, that this is an interference process.

A closer look at these results shows a peculiar distinction for the value $\phi = \pi$. While the rise and fall characteristic of the THz trace was gradual in the previous case, it is more pronounced and focused around the $2\pi$ values here. A secondary oscillation peak arises at $\phi = \pi$ and is visible in both samples. This behavior points to a distinct distribution of the current density. The experiment was repeated for the 2-color mask with the same temporal separation and the results are presented in Fig. 4.17. This was done in order to test, whether this is due to the temporal separation or a peculiarity of the pulse pair generated by the rectangular phase mask.

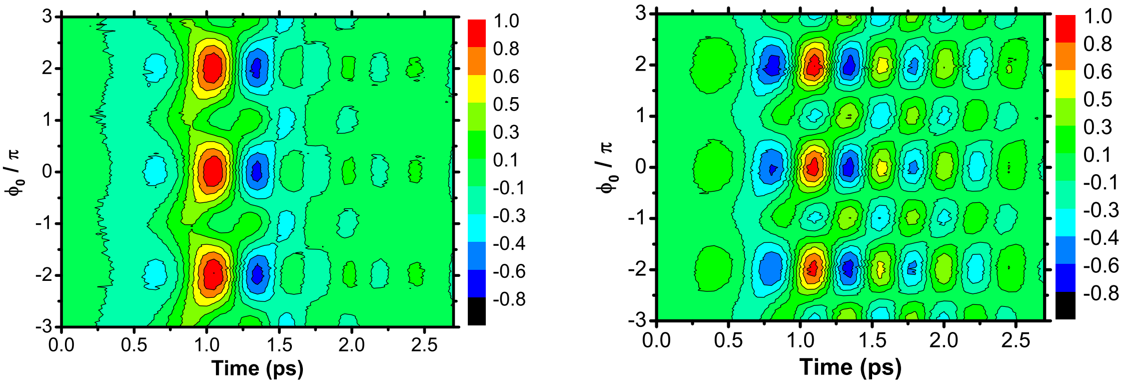

(a) Shift current

(b) Rectification current

Figure 4.16: Phase dependence of rectification and shift currents for the rectangular phase mask set to $\tau = 200\,\text{fs}$ (Experiment). That the oscillatory pattern is visible even for these large temporal separations is further proof for an interference process. The shape of the pattern is distinct from the $\tau = 60\,\text{fs}$ case.

The differences in the results are striking. The outcome of the experiment with the 2-color mask for 200 fs closely resembles the case for 60 fs. Though it shares the more pronounced rise and decay times with the 200 fs rectangular case. In light of these findings, a look at the respective FROG traces is appropriate.

The $\phi = 0$ case is shown in Fig. 4.18, as the effect of the pulse envelopes of the two masks is clearly visible here. The FROG trace corresponding to the rectan-

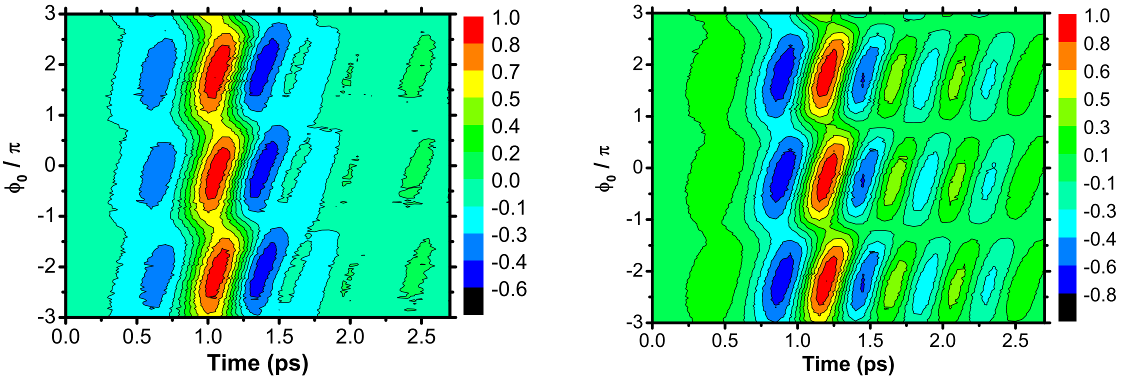

(a) Shift current

(b) Rectification current

Figure 4.17: Phase dependence of rectification and shift currents for the 2-color phase mask set to $\tau = 200\,\text{fs}$ (Experiment). The pattern here closely resembles the one for $\tau = 60\,\text{fs}$ case, in contrast to the rectangular phase mask.

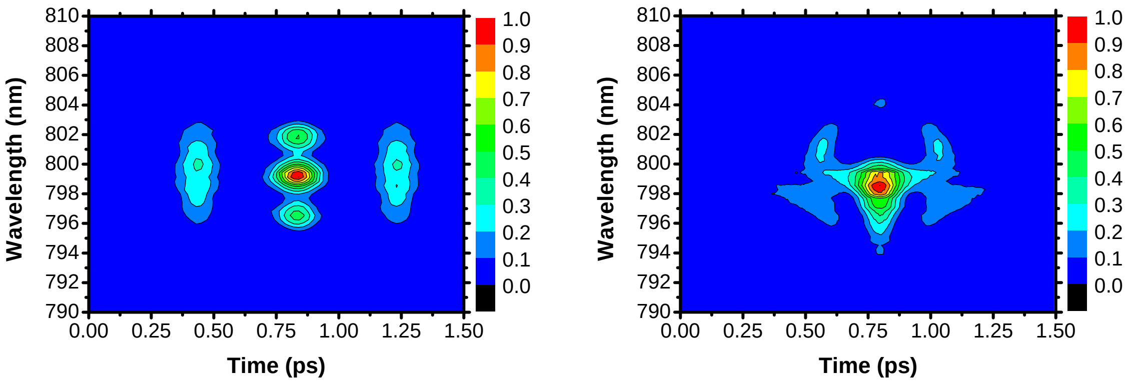

(a) Rectangular phase mask

(b) 2-color phase mask

Figure 4.18: FROG traces for a temporal separation of $\tau = 200\,\mathrm{fs}$ and an absolute phase of $\phi = \pi$ for the two phase masks. The distinct differences here account for the different THz patterns from before. The high structure and symmetry of the rectangular phase mask is in stark contrast to the 2-color phase mask.

gular mask is in Fig. 4.18a, while the respective trace for the 2-color mask is in Fig. 4.18b. The trace on the left is distinguished by its symmetry, while the symmetry is broken in the right pane by the applied linear chirp to one side of the spectrum. The locus of the pulse is dependent on which side of the spectrum the slope is applied. The influence of the rigid pulse structure of the pulse shaped by the rectangular mask on the current density is evident, though no comparable disruption is caused by the 2-color mask.

Overall, the results are very convincing. It was shown, that the pulse shaper is a useful tool to manipulate the absolute phase of a pulse pair; in essence manipulating the superposition of these two electric fields and hereby shaping the pulse envelope. This is reinforced by the oscillating behavior of the THz traces with a period of $2\pi$. It was therefore proven, that it is possible to coherently-control the current density of shift and rectification currents through control of the absolute phase of the pulse pair.

At least two questions remain open: THz radiation functions as a sensor for the behavior of the currents. Is it possible to deduce the underlying current? The oscillations of the THz trace are a consequence of the limited bandwidth of the electro-optical sampling process. As such, a look at the impact of the pulse-pair variations on the THz field would be instructive. These questions are answered by a model that replicates the experiment and offers insight into the underlying processes.

### 4.2.2 A Model of the Current Density

The detailed description of the model was given in section 3.3. This section will focus on the detailed analysis of the results obtained through the model. It will be shown, that the straightforward model can explain almost all of the discussed properties.

The small temporal separation of 60 fs is discussed first. Analogous to the experimental case, it is straightforward to set for the 2-color mask, but needs to be calibrated for the rectangular phase mask. The temporal separation of the pulse pair was measured through evaluation of the autocorrelation integral and correlated with the intended separation to generate the correct scaling factor.

The generated stacked THz plots are presented below for all the examined cases. The rectangular mask is discussed first. The good agreement with the experiment is striking, see Fig. 4.19a for a stacked 3D plot of the THz emission generated with the shift and Fig. 4.19b for the rectification current. The oscillatory pattern with a period of $2\pi$ is retained, as is the slight time shift that depends on the phase variation. Even the differing slopes of the two current processes are replicated. The modeled traces do have a more distinctive oscillatory tail in contrast to the measured ones. This is attributed to the straightforward implementation of the current generation process that does not consider scattering or any other energy-distributing process. The excellent agreement between the model and the experiment implies that the model is able to provide insight into the underlying current density and the real THz field. The current density of both processes is identical by design and presented in Fig. 4.20.

The characteristics of the process are easier to describe with a closer look at its shape for some of the special values of $\pi$ that are presented in Fig. 4.21. The pulse envelope is intact for an absolute phase of $\phi = 0$, and the current density presents itself as a single peak, due to the close proximity of the two peaks. This is contrasted by the situation for $\phi = \pi$, where the envelope is split into two separate peaks, that produce two distinct peaks of equal height in the current density.

The peak strength falls below 50%, but the total density remains constant, as the remainder is absorbed in the broadened wings of the distribution. The half integer $\pi$ values are the transition states between the two framing states. The pulse envelope breaks apart and the main peak shifts to later times, while a weak second peak emerges simultaneously for earlier times. This movement is responsible for the visible shift of the main THz peak. It appears that the main displacements of

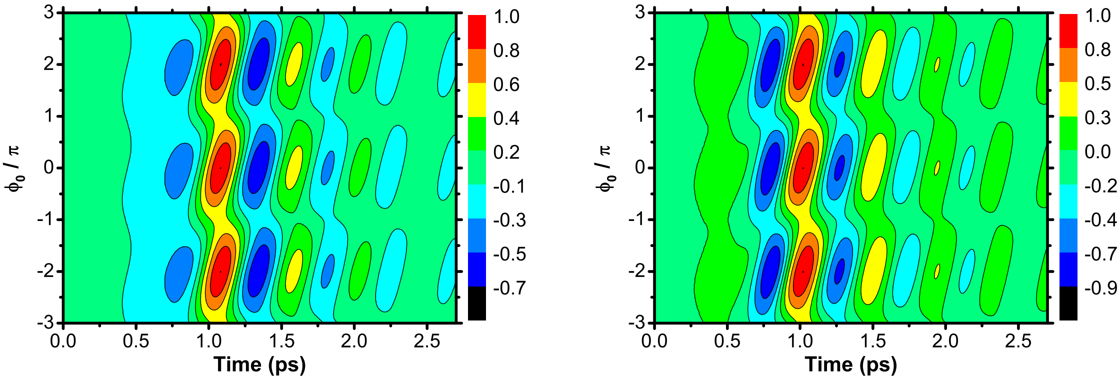

(a) Shift current

(b) Rectification current

Figure 4.19: Phase dependence of rectification and shift currents for the rectangular phase mask set to $\tau = 60\,\mathrm{fs}$ (Model). The model corroborates the experimental data for both current types. The oscillatory pattern modulo $2\pi$ is retained. Minor differences to the experiment are attributed to the straightforward simulation of the current generation process.

the current density peaks occur in the first and last $\pi/2$ segment. In the second and third $\pi/2$ segments the peak heights first even out before the second peak gains dominance. This fluid motion is captured in the stacked plot. As the first peak moves to later times, the second peak slowly emerges, becomes dominant, and fades away as a new peak appears. The breakup of the pulse envelope is notable. For a set time delay of 60 fs, the resultant time difference of the two current peaks approaches 130 fs for $\pi/2$ and 140 fs for $\pi$.

The comparison of experimentally (Fig. 4.22) and theoretically (Fig. 4.23) obtained THz traces for GaAs reinforces the proclaimed excellent correspondence even for single THz traces. The main features match: the shape and the time dependence of the traces are in accordance, as is the phase dependence.The shape of the trace for $\phi = \pi$ is notable as it resembles a single-cycle THz pulse.

A few discrepancies remain and shall be discussed:

- The experimentally obtained traces rise a bit, before they drop.
- The peak heights of the experimentally obtained traces for $\pi/2$ and $3/2\pi$ do not exactly correspond to each other, though the time separation follows the predicted behavior.
- The decay behavior of the oscillations does not match. The theoretical trace follows a Gaussian envelope, but the experimentally obtained trace exhibits a sudden amplitude drop and the oscillations stay at a constant

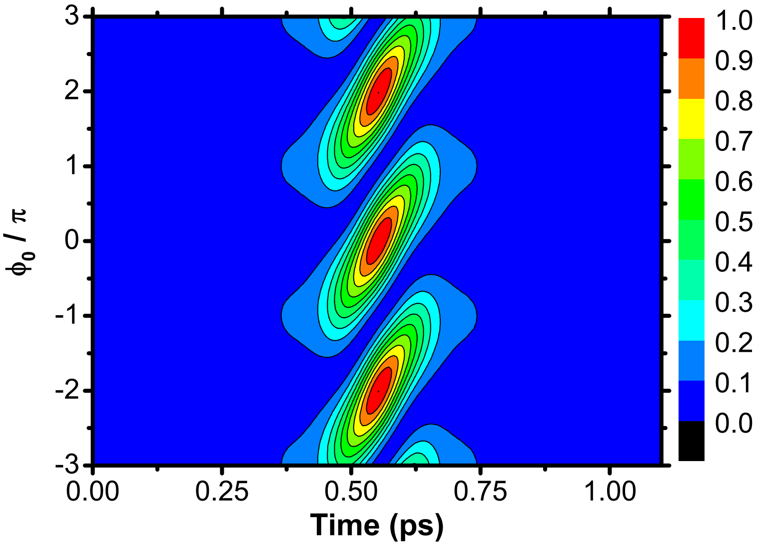

Figure 4.20: Phase dependence of the current density for the rectangular phase mask set to $\tau = 60\,\text{fs}$ (Model). The current density follows the evolution of the pulse envelope shape closely. The oscillatory pattern modulo $2\pi$ is also visible here, which is the final proof of the coherent control scheme.

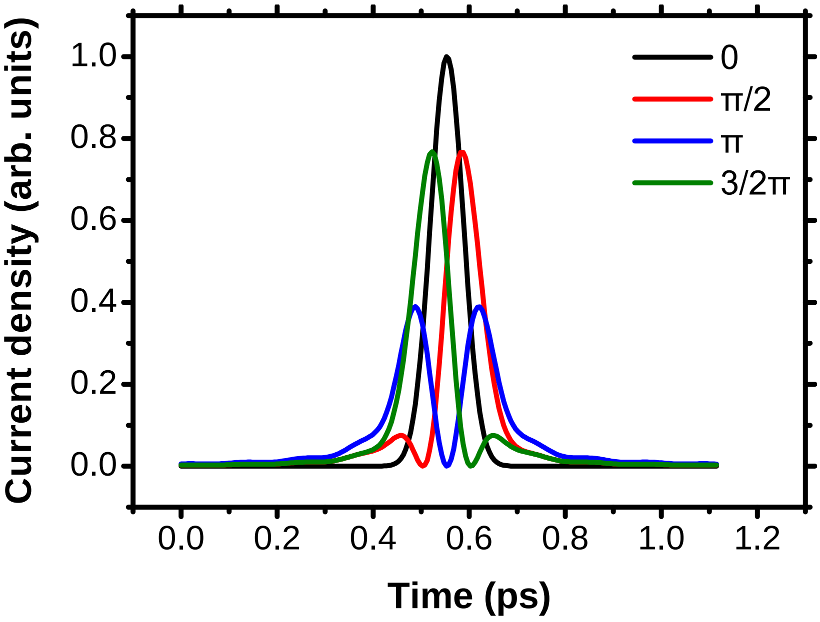

Figure 4.21: Select traces of the current density for CEP values of $\phi = 0, \pi/2, \pi, 3/2\pi$. As the absolute phase gradually increases, a second pulse becomes visible and the energy distribution between the two pulses is equalized for $\phi = \pi$. The second peak begins to dominate and finally becomes the sole visible peak when the cycle is complete.

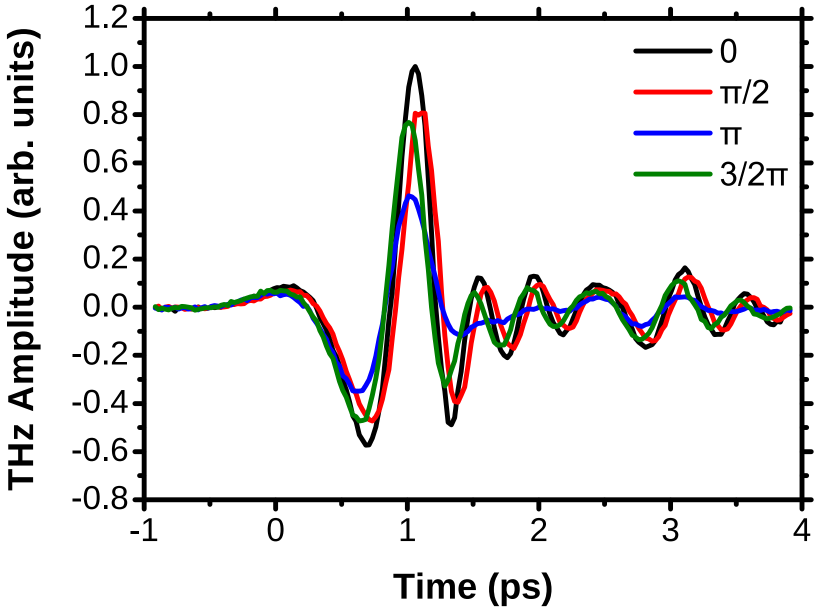

Figure 4.22: Select THz traces of the shift current for CEP values of $\phi = 0, \pi/2, \pi, 3/2\pi$ (Experiment).

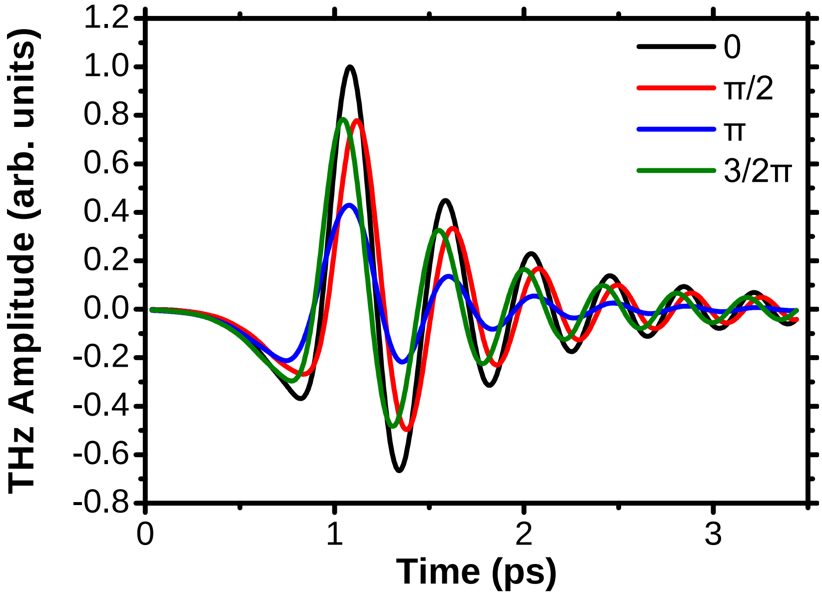

Figure 4.23: Select THz traces of the shift current for CEP values of $\phi = 0, \pi/2, \pi, 3/2\pi$ (Model). The correspondence with the experimentally measured traces is excellent. Some of the discrepancies are discussed in the text.

value. The oscillations in the experimental case are neat only for the first two, while the third has an odd form. This is not the repeater THz pulse which is seen at much later times, usually after tens of ps.

- The ratio of the first and second dip is reversed from experiment to theory.

Most of these discrepancies are attributed to the very simple electro-optical sampling process. The slight rise might be an indicator for an unconsidered parameter, while the unmatched dip ratio might be caused by alignment. This is not a sign of faulty alignment, as both cases have occurred on occasion after realignment of the setup. This was deemed not crucial, but now that the shape of the modeled trace is known, greater care could be taken to replicate the model and find the underlying cause for this.

These points remain valid for all the conducted experiments and also for the rectification currents in ZnTe. A few additions and discrepancies between the experiment (Fig. 4.24) and the model (Fig. 4.25) are pointed out below:

- The theoretically obtained trace now rises slightly which is not matched by the experiment.
- The ratios of the first and second dip still do not match and are reversed now.
- The experimental trace for $\phi = \pi$ does not approach a single-cycle waveform.
- The drop-off in the amplitude of the oscillations is not as pronounced as in GaAs therefore the match with the theoretical trace is better.

These discrepancies have a profound impact on the shape and form of the THz spectrum, as shown in Fig. 4.26 (experiment) and Fig. 4.27 (model), for the rectangular mask and a temporal separation of 60 fs. The raggedness of the experimentally obtained spectrum is a direct consequence of the non-uniform periodicity of the oscillations. The overall drop in magnitude especially around 2 THz is visible in both cases. As expected for a simple time shift, the traces for $\pi/2$ and $3/2\pi$ produce the same spectrum.

An interesting observation is the predominance of the peak at 2 THz in the theoretical spectrum. This is not surprising, when the shape of the transfer function (see Fig. 3.14) is taken into account and combined with the shape of the full THz field (see Fig. 3.12b). The rise of the field is multiplied with the near constant value of the transfer function; as such it is only natural for the peak at 2 THz to appear. But why does the behavior the model differ from the experiment? The

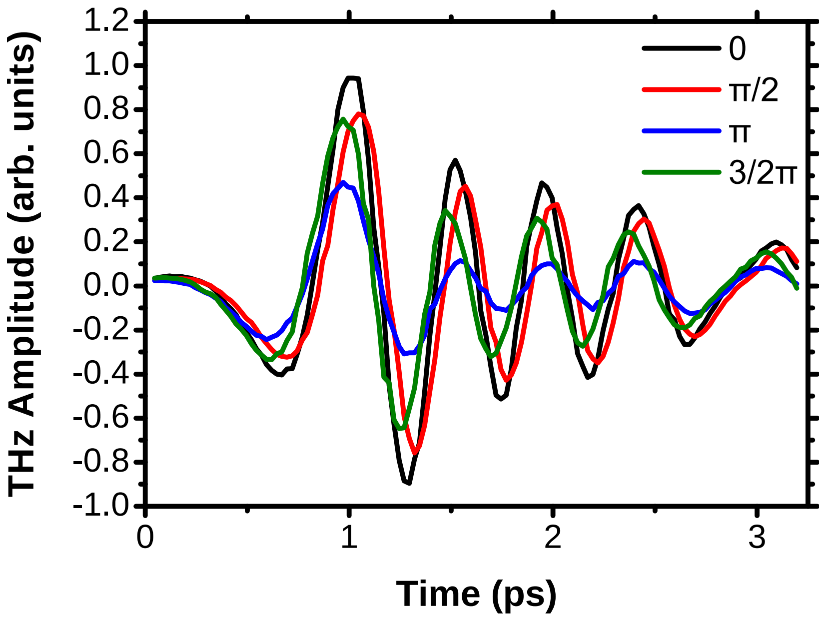

Figure 4.24: Select THz traces of the rectification current for CEP values of $\phi = 0$, $\pi/2$, $\pi$, $3/2\pi$ (Experiment).

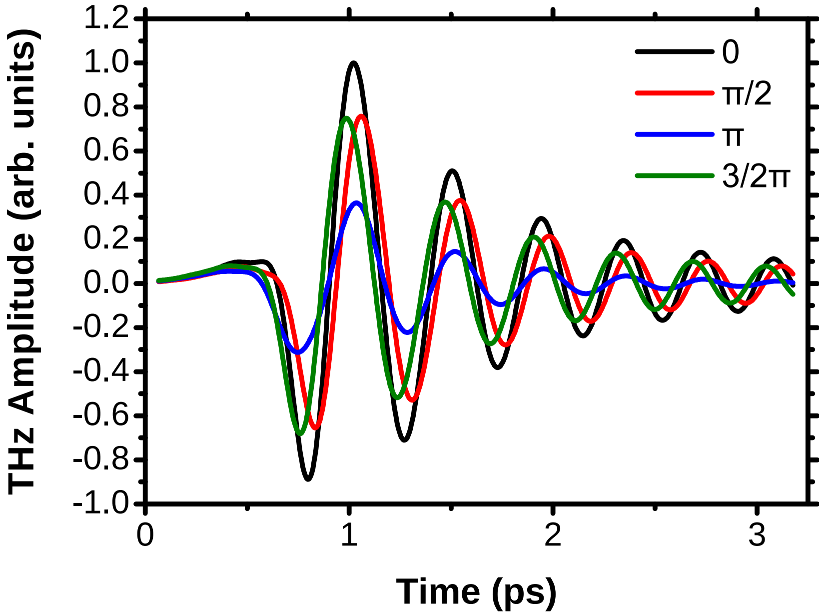

Figure 4.25: Select THz traces of the rectification current for CEP values of $\phi = 0$, $\pi/2$, $\pi$, $3/2\pi$ (Model). The correspondence with the experimentally measured traces is excellent. Some of the discrepancies are discussed in the text.

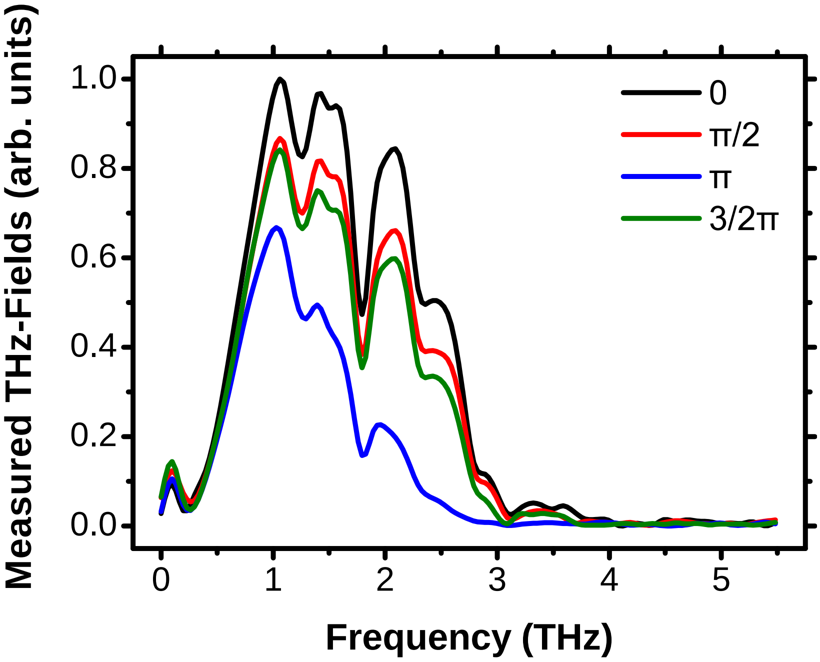

Figure 4.26: Select THz spectral traces of the shift current for CEP values of $\phi = 0$, $\pi/2$, $\pi$, $3/2\pi$ (Experiment).

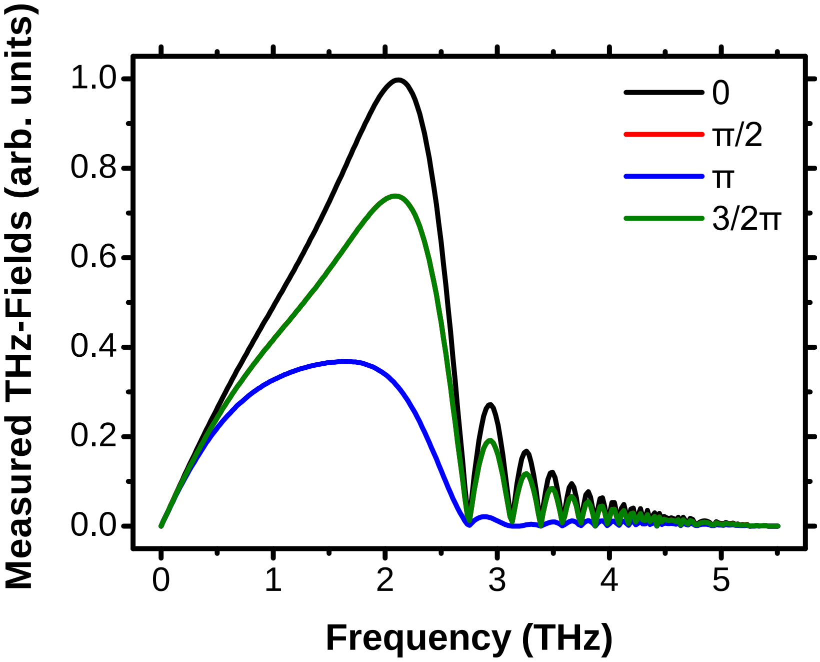

Figure 4.27: Select THz spectral traces of the shift current for CEP values of $\phi = 0$, $\pi/2$, $\pi$, $3/2\pi$ (Model). Although the general shape and behavior of the experiment are retained, the discrepancies are attributed to the very simple electro-optical sampling model. Notable is the behavior of the peak at 2 THz, which is visible both in the experiment and in the model.

answer must lie in the chosen limits of the model. The straightforward modeling of the currents through the mixing of the two electric fields has no real free parameter to adapt the theory to the experiment. The only way to exert any influence is through the thickness of the detection crystal, but the effect this has on the spectrum is limited. Reducing the thickness shifts the peak to higher frequencies, increasing the thickness moves it to lower frequencies. The overall shift is small and significantly changes the shape of the THz time trace, i.e., does not solve the conflict between THz time trace and spectral shape. This might indicate that the electro-optical sampling model is too simple.

The model gives access to the real THz field and the effects the second electric field has on it, as shown in Fig. 4.28 for shift and Fig. 4.29 for rectification currents. This is especially interesting in light of the approximation of a single-cycle pulse for the phase $\phi = \pi$ in the GaAs crystal.

The second field causes a constriction at 2.5 THz. The first segment of the real THz field lies within the detectable bandwidth. This causes the single-cycle THz trace. Inspection of the recorded THz traces for the case $\phi = \pi$ (Figs. 4.22 & 4.24) reveals that the oscillations in GaAs are more suppressed than in ZnTe, which could be explained by a remaining overlap of the real THz field and the transfer function. In the GaAs case, it seems, as if the first segment lies well within the detectable bandwidth, while significant overlap remains for ZnTe. Further optimization could increase the attenuation.

Increasing the time separation of the two pulses introduces further constrictions, as shown for GaAs and a separation of $\tau = 200$ fs. The real THz field is in Fig. 4.30, while the measured field is in Fig. 4.31. The width of the first segment is controlled by the relative phase, and leads to a different situation than above. The peak of the measured field for $\phi = \pi/2$ and $\phi = 3/2\pi$ lies now below 2 THz. The oscillations of the corresponding THz trace are reduced significantly.

The discussion is continued with a look at the evolution of the THz traces and the associated currents for long time delays. The modeled graphs agree well with the experiment, as expected. Therefore only exemplary proof is given through the stacked traces of GaAs. Analogous to the previous figures, the effects of the rectangular mask are in Fig. 4.32a, while the results of the 2-color mask are in Fig. 4.32b. The interesting structure of the THz trace created by the rectangular mask is preserved, while the small peaks in between are more pronounced, which is of course related to the higher fidelity and the absence of noise in the theoretical approach. The 2-color traces are distorted and seem elongated, same as in the experimental case.

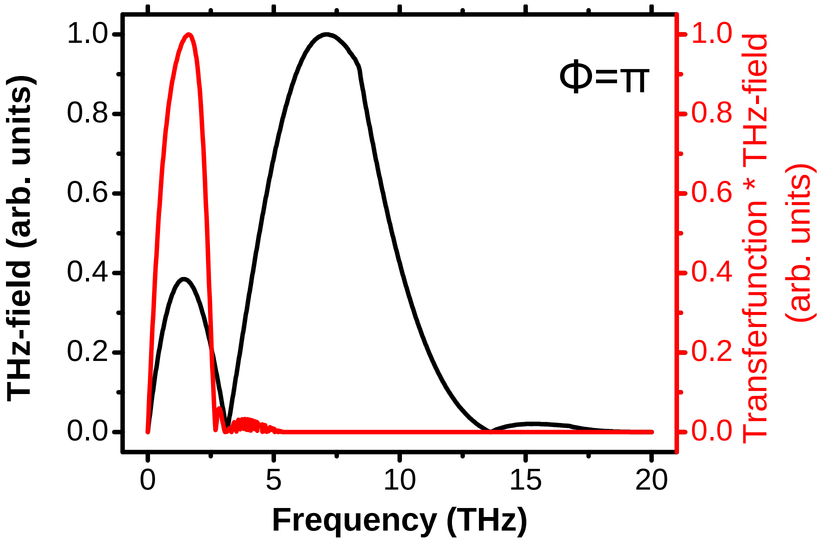

Figure 4.28: Comparison of the real and measured THz field for shift currents at $\phi = \pi$. The shapes of the THz traces for different values of the absolute phase can be explained with the limited bandwidth available in the detection crystal. The addition of a second field causes constrictions in the real THz field where the complete field is detained within the limited bandwidth and THz pulses that resemble single-cycle pulses become visible.

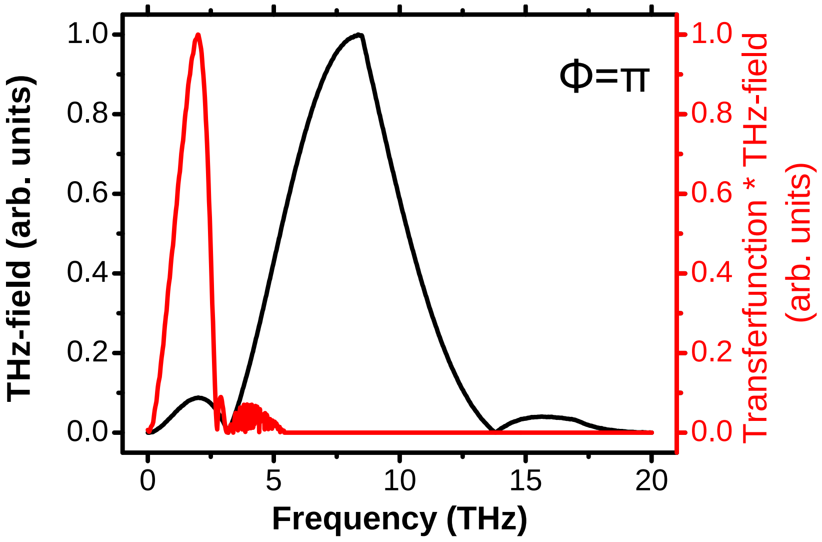

Figure 4.29: Comparison of the real and measured THz field for rectification currents at $\phi = \pi$. See above for explanation.

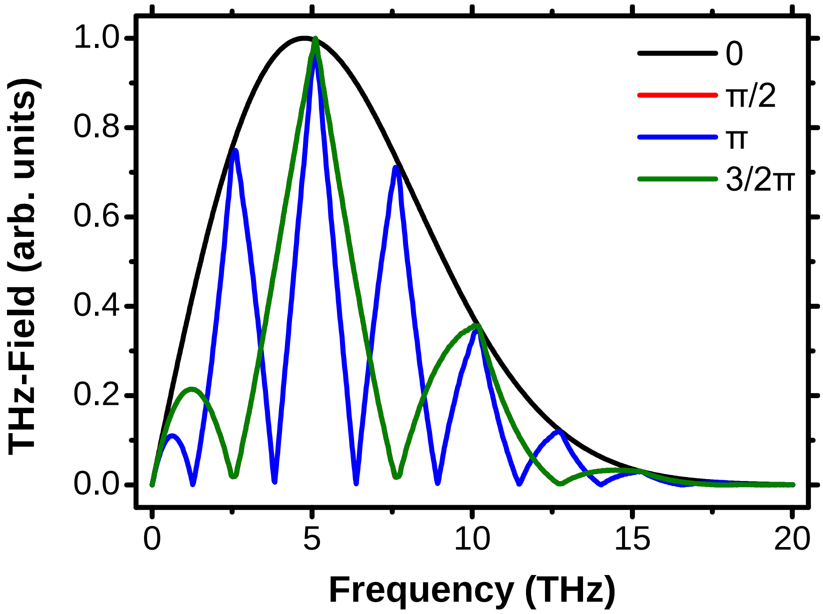

Figure 4.30: Select traces of the real THz field for CEP values of $\phi = 0, \pi/2, \pi, 3/2\pi$ and $\tau = 200\,\text{fs}$. The increased temporal separation introduces additional constrictions to the THz field. The shape of the THz trace depends on the overlap between the real THz field and the transfer function.

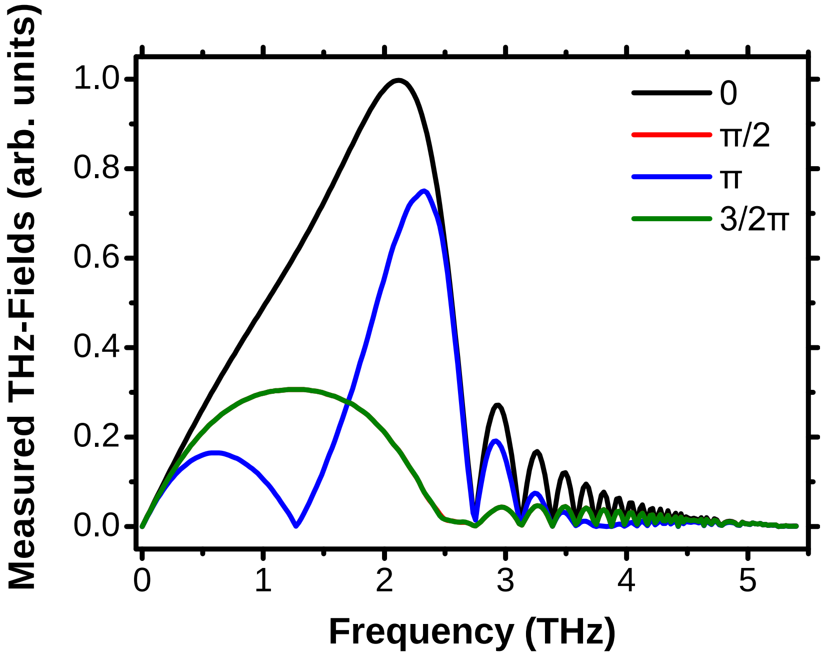

Figure 4.31: Select traces of the measured THz field for CEP values of $\phi = 0, \pi/2, \pi, 3/2\pi$. Electro-optical sampling drastically influences the shape of the measured THz fields, especially in the high frequency range.

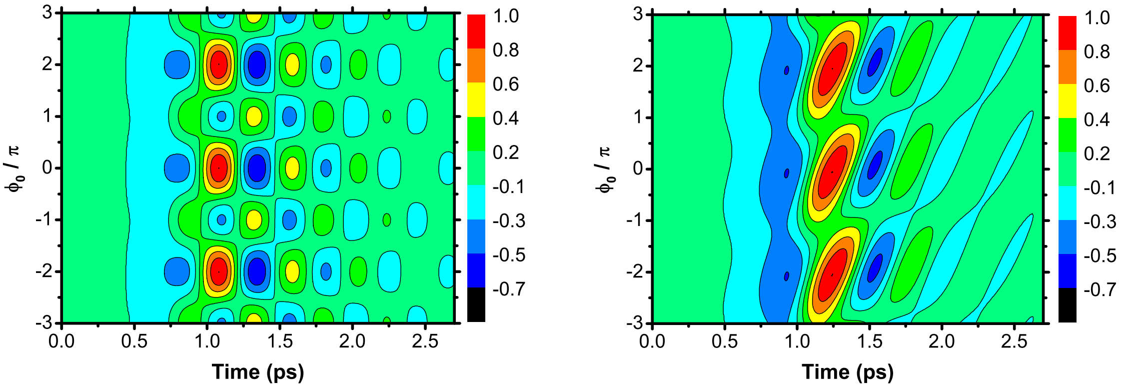

(a) Rectangular phase mask (b) 2-color phase mask

Figure 4.32: Phase dependence of shift currents for the rectangular and the 2-color phase masks set to $\tau = 200\,\mathrm{fs}$ (Model). The model nicely reproduces the experimental findings. The two phase masks produce very distinct THz emission patterns at these temporal separations.

The only distinguishing property is the phase mask, as the current density for GaAs and ZnTe are identical. The rectangular mask produces strongly localized islands of current density, amongst which it oscillates according to the relative phase (Fig. 4.33a), in contrast to the distribution generated by the 2-color mask which is smeared out (Fig. 4.33b). The stacked THz traces correspond nicely to the character of the current density. It is astonishing, but in accordance with

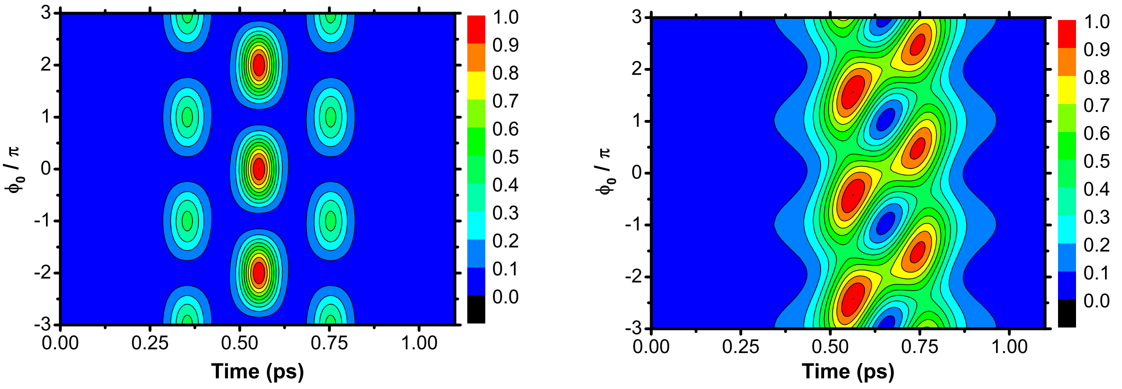

(a) Rectangular phase mask (b) 2-color phase mask

Figure 4.33: Phase dependence of the current density for the rectangular and the 2-color phase masks set to $\tau = 200\,\mathrm{fs}$. The distinct THz emission pattern is a byproduct of these distinct current density distributions. Note the strong structure and symmetry for the rectangular mask and the more fluid shape of the 2-color mask.

the field interference scheme, that the pulse envelope is susceptible to phase changes even for these large time separations.

This concludes the discussion of coherently controlled THz emission through control over the dependency of the relative phase of rectification and shift currents. The last comparison puts the properties of the two masks nicely into perspective. The rectangular mask produces very structured pulse envelopes, while the 2-color mask produces more fluid shapes.

### 4.2.3 Capturing the Essence - The Coherent-Control Equation

The coherent-control equation is derived in this section in accordance with the previously discussed coherent-control experiments. A literal reading of the relationship of equation (2.98) leads to the following link between the susceptibility and the incident electric fields:

$$J(t) \propto E^2(t). \tag{4.1}$$

Appropriate electric fields are given by

$$E_1(t) = A_1(t)\,\mathrm{e}^{-\mathrm{i}\omega_0 t} + \text{c.c.}, \tag{4.2}$$

$$E_2(t) = A_2(t+\delta t)\,\mathrm{e}^{-\mathrm{i}\omega_0 t}\,\mathrm{e}^{-\mathrm{i}\phi_0} + \text{c.c.}. \tag{4.3}$$

Here, the temporal separation is denoted in $A_2(t)$ through inclusion of $\delta t$. The added relative phase is given by the factor $\exp(-\mathrm{i}\phi_0)$ which is the standard way of including a phase in an electric field.

To facilitate legibility, the following abbreviations are introduced

$$E_1(t) = E_{10}(t) + E_{10}^*(t), \tag{4.4}$$

$$E_2(t) = E_{20}(t) + E_{20}^*(t), \tag{4.5}$$

$$E(t) = E_1(t) + E_2(t), \tag{4.6}$$

where the complex conjugate is denoted by the $*$. Squaring equation (4.6) leads to 16 terms, that were already given in their condensed form in equation (2.9). Of interest are only the difference frequency terms, given by

$$E^2 = 2E_{10}E_{20}^* + 2E_{10}^*E_{20}. \tag{4.7}$$

The proportionality is resolved through use of the susceptibility tensor. It is assumed to be a scalar in this straightforward derivation. Additionally, its dispersion is neglected. This leads to

$$\begin{aligned} J &= \sigma_2 E^2 && (4.8) \\ &= 2\sigma_2 \left( E_{10} E^*_{20} + E^*_{10} E_{20} \right) && (4.9) \\ &= 2\sigma_2 \left( A_1 A_2 \, \mathrm{e}^{\mathrm{i}\phi_0} + A_1 A_2 \, \mathrm{e}^{-\mathrm{i}\phi_0} \right) && (4.10) \\ &= 4\sigma_2 A_1 A_2 \cos(\phi_0). && (4.11) \end{aligned}$$

This formula captures the essence of the coherent-control process described here. The magnitude and the direction of the current density are controlled through the relative carrier envelope phase between the two incident pulses. This relationship is the same for both current densities, as the additional time derivative for the calculation of the rectification current does not act on the cosine.

### 4.2.4 One More Thing

The coherent-control equation reveals a yet unexplored degree of freedom. The relative time-dependence of the pulse envelopes is dependent on the value of the relative carrier envelope phase $\phi_0$. In this configuration, the first pulse is pinned to a fixed position, while the time delay of the second pulse is varied. Here, the examined time window is 1.6 ps long, very large compared to the individual pulse lengths. The behavior is exactly the same for the two processes, therefore only the case of GaAs is discussed.

The experimental traces are presented in Fig. 4.34. The relative phase is successively increased by $0.5\pi$ in the panels, beginning with a relative phase of $\phi_0 = 0$ in the upper left panel. The behavior of the THz waveforms is uniform. At small time separations, a single peak is visible that shifts with time. This is similar to the shift observed above, when the relative phase was varied. The main focus of the pulse envelope is determined by the superposition of the electric fields, which shifts with the temporal separation. Apart from that, the main distinguishing features lie in the periphery. The traces generated by a phase of $\phi_0 = 0.5\pi$ and $\phi_0 = 1.5\pi$ are expected to be identical except for a slight time shift, but there are differences. The center is square shaped in the latter case, and the pattern of the accompanying oscillations is distinct.

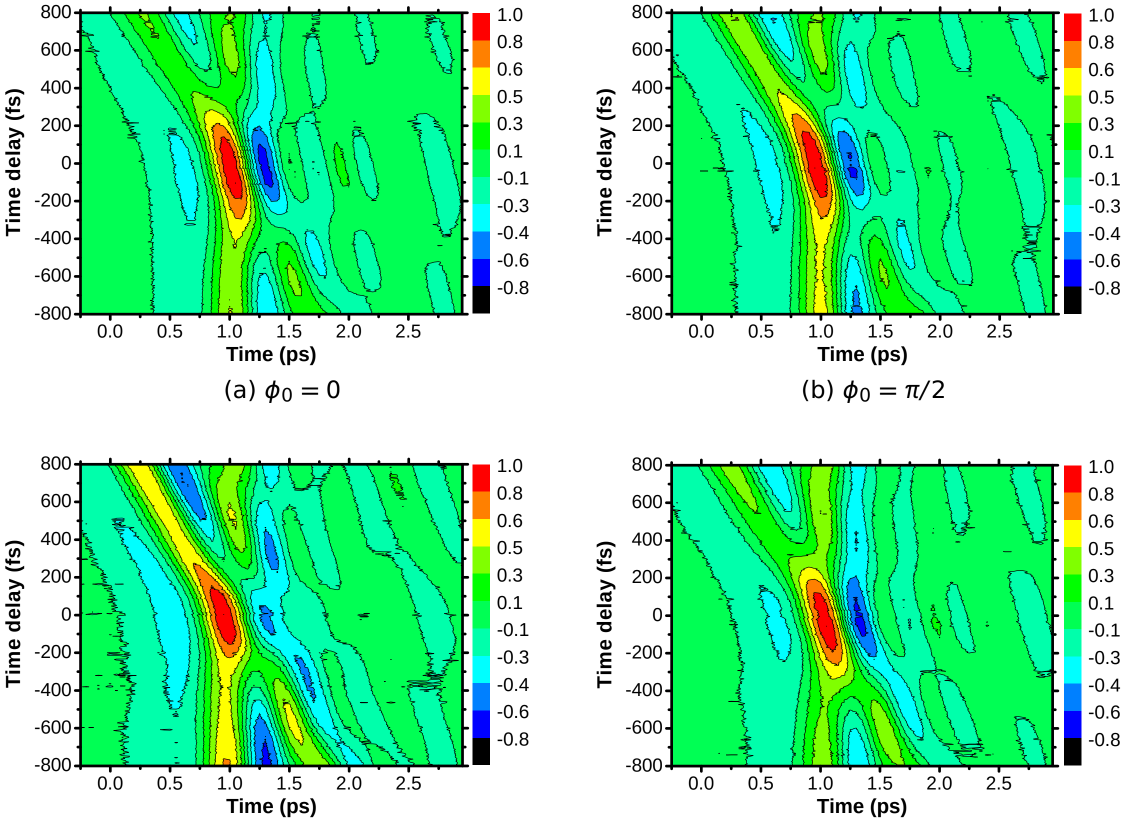

(a) $\phi_0 = 0$

(b) $\phi_0 = \pi/2$

(c) $\phi_0 = \pi$

(d) $\phi_0 = 3/2\pi$

Figure 4.34: Temporal dependence of the shift currents for CEP values of $\phi_0 = 0$, $\pi/2\,\pi\,3/2\pi$ (Experiment). A single peak is visible for small temporal separations that diminishes for larger separations.

The agreement between experiment (Fig. 4.34) and model (Fig. 4.35) is very good. Some features of the theory that are not as pronounced in the experiment, are attributed to the real world conditions that always impede the fidelity of the data. It is reassuring to see that the overall form between the $\phi_0 = 0.5\pi$ and $\phi_0 = 1.5\pi$ is also not symmetrical in the modeled case.

Again, the behavior of the THz traces is explained through the behavior of the underlying current. This is shown in Fig. 4.36. As the current density follows the pulse envelopes directly, the pinned pulse is clearly visible as the vertical stripe visible in all four cases. The variation of the temporal separation generates the diagonal streak. For large delays, a second THz peak becomes visible at around 600 fs. The current densities of the half integer values of $\pi$ are indeed point symmetrical, and thus produce the distinct THz patterns.

The relative carrier envelope phase regulates the relative magnitude between the

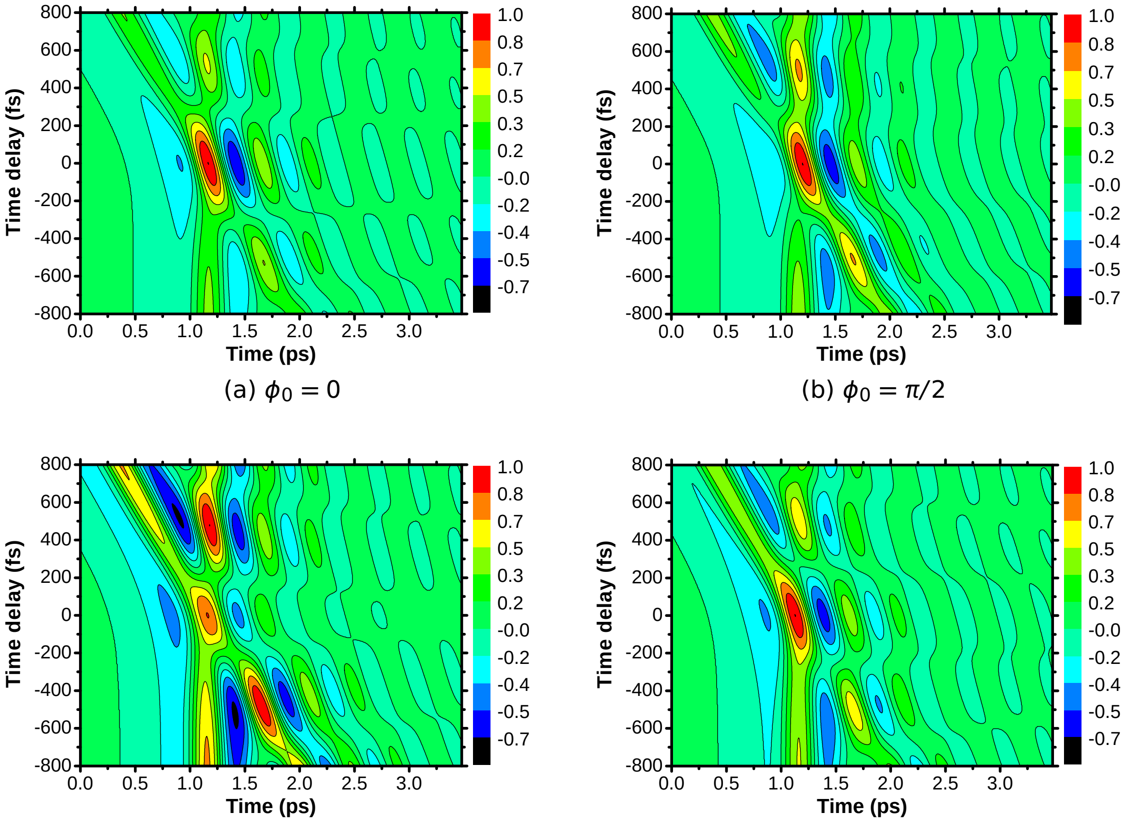

(a) $\phi_0 = 0$

(b) $\phi_0 = \pi/2$

(c) $\phi_0 = \pi$

(d) $\phi_0 = 3/2\pi$

Figure 4.35: Temporal dependence of the shift currents for CEP values of $\phi_0 = 0$, $\pi/2\,\pi\,3/2\pi$ (Model). The agreement between experimental and theoretical data are again very good.

current density peaks, which are equal in the $\phi_0 = \pi$ case. Here, a very distinct anti-crossing behavior is visible, while it is more nuanced in the other cases. For $\phi_0 = 0.5\pi$, the incoming peak dominates at first, but loses that role after crossing the divide between negative and positive delay times. The pinned peak suddenly dominates. In the $\phi_0 = 1.5\pi$ case, this behavior is reversed, first the pinned peak dominates, but concedes it to the moving peak. This is replicated in the THz patterns, where the signature of the pinned peak is clearly visible.

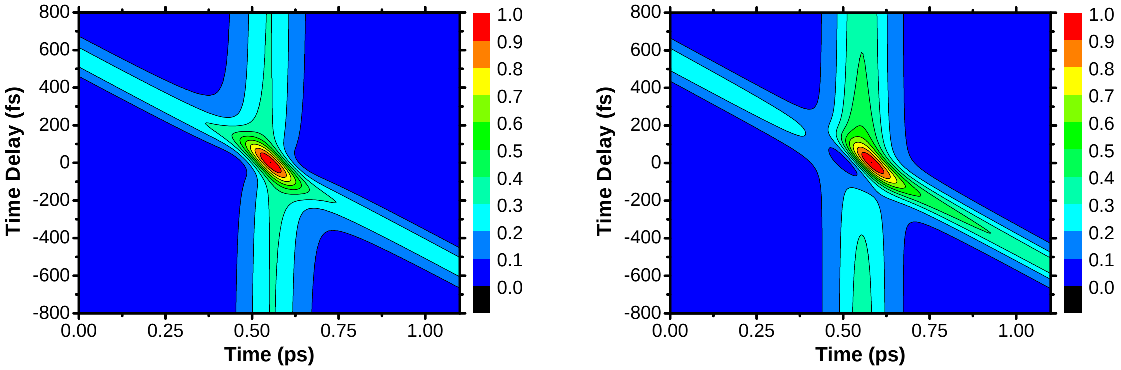

(a) $\phi_0 = 0$

(b) $\phi_0 = \pi/2$

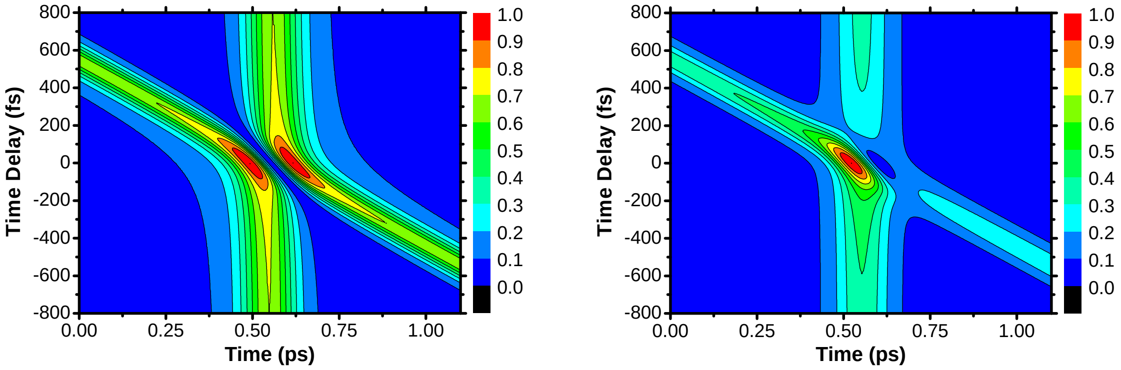

(c) $\phi_0 = \pi$

(d) $\phi_0 = 3/2\pi$

Figure 4.36: Temporal dependence of the current density for CEP values of $\phi_0 = 0$, $\pi/2\,\pi\,3/2\pi$. The motion of the two current density peaks is the same for each of the panels. The relative strength between the two peaks is the determining factor for the behavior and the emitted THz radiation.

### 4.2.5 Conclusions

It was shown, that a straightforward interpretation of the relationships proposed in equations (2.98) & (2.99) leads to a full and complete model of the THz generation process through shift and rectification processes.

It was shown, that by using special phase masks, the absolute phase, i.e., the carrier envelope phase is accessible. Though in order to make it visible at the times scales used here, a second electric field needs to be introduced. The second field enables the coherent-control of shift and rectification currents through regulation of the relative phase between the two phase-stable pulses. The excellent agreement between experiment and model enables a direct look at the behavior of the underlying current.

The importance of the interaction between the real THz field and the electro-optical transfer function has been highlighted. This led to an idea for a framework to create single-cycle and even arbitrary THz pulses, which is going to be discussed in detail in the next chapter.

# 5 Creating Arbitrarily Shaped THz Traces [1]

The rate with which novel THz applications are introduced to the marketplace is increasing steadily. The higher bandwidth of the THz compared to the GHz band make it a favored component of the next generation of network appliances. Microfabrication techniques promise to make it available without crossing into the optical realm [98, 99].

THz radiation is also a very useful light source. Applications include, amongst others, noninvasive imaging [100] and molecular spectroscopy [101], but also for the examination of intraband processes in semiconductors. Examples here include the probe of the buildup of screening in bulk GaAs [102], and the buildup of exciton populations after optical excitation [103, 104].

A wide variety of THz sources apart from the introduced shift and rectification currents are in use. The requirements of the application dictate the appropriate source. The choice might fall on antenna-like devices, which have a very high signal to noise ratio and deliver almost single-cycle THz pulses with limited bandwidth [87]. Or, for higher bandwidth needs, a combination of generation through rectification in ZnTe and detection with GaP is suggested [105].

The need for full control over the shape of the time trace and its accompanying detectable spectrum is apparent. The challenge therefore is clear: Developing a framework, that is capable of efficiently creating arbitrary THz shapes, and/or focuses on the spectral bandwidth.

## 5.1 The Framework

A series of interesting experiments have shown that creating highly structured THz traces is a very active field. To highlight the existing approaches to this

---

[1] Parts of this chapter were published in [86].

challenge, two of the attempts by other groups are presented here.

The first approach uses a specially engineered crystal, in this case a specially designed periodically poled lithium niobate (PPLN) crystal [106]. Here, the alternation of different crystal domains creates a structure that pieces half-cycle THz traces together to create a THz pulse train. This technique has also been demonstrated in periodically inverted GaAs structures [107].

The other approach utilizes a form of pulse shaping. This solution uses a model of the THz generation process. The shape of the impinging optical pulse is optimized with a Gerchberg-Saxton algorithm, which is an iterative phase-retrieval algorithm, to generate the desired shape of the THz trace [108].

Though both of these approaches are viable solutions to the problem, they are both unable to adapt to a change of conditions. This shall be addressed within this framework. The previous chapters established the shape of the pulse envelope as the significant control parameter. It was shown, that the addition of a second phase-stable pulse enhances the pulse shaping capabilities. The two important parameters are the temporal separation, and the relative Carrier Envelope Phase (CEP) between the two pulses. The challenge is to optimize the interplay of the parameters to arrive at the desired shape for the THz trace. An evolutionary algorithm is the suitable tool for this task.

The THz generation through rectification in ZnTe is used as the model system. Two goals are set out to test the feasibility of the setup. The first goal is the suppression of the oscillatory tail of the THz trace. The second goal is the creation of a highly structured THz trace, in this case a waveform consisting of two consecutive single-cycle pulses. The oscillations are linked to a dispersive phonon-polariton that propagates through the crystal [109]. But the extensive modeling of the previous chapter has shown that these explanations are not necessary. The oscillation is fully explainable with the limited bandwidth of the electro-optical sampling of the THz field obtained through the theoretical description in [36, 37]. Both approaches indicate the necessity to structurally shape the THz spectrum beyond 2 THz thereby eliminating the possibility to distinguish the contributions.

The two previously introduced phase masks are also used here, with the important distinction, that the 2-color phase mask is defined differently. This experiment predates the previous one. The relevance of the CEP for pulse envelope shaping was not apparent at that time. It was not at all clear, that it is possible

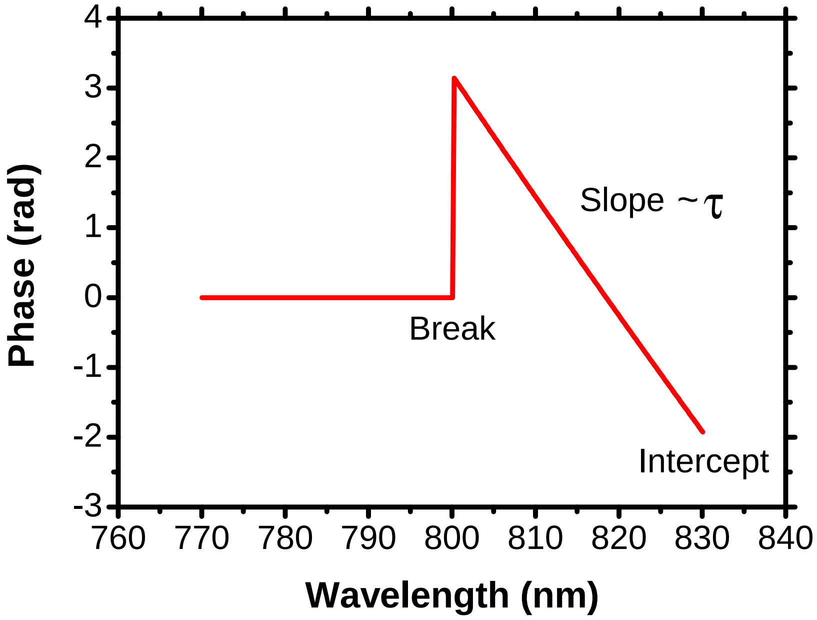

Figure 5.1: Definition of the 2-color mask. The focus was on the time parameter, therefore the line was fixed with the intercept. In hindsight, it would have been wiser to use the offset, as the CEP is the relevant parameter here.

to access the CEP at these time scales with the current setup. Under the assumption, that the oscillations are suppressed by introduction of a second pulse at the right time, the focus lay solely on the time parameter. Fig. 5.1 details the different nomenclature. The break parameter distributes the power between the two pulses, and is set to create a strong first pulse, which is followed by a weaker second pulse to suppress the oscillations. The slope of the line is set directly and pinned with the specified intercept. In hindsight it might have been better to use the offset as the anchor, as it is the relevant parameter.

Apart from this distinction, the degrees of freedom are the same as in the previous experiment. The rectangular phase is defined the same way. Here, the accessible parameters are the temporal separation, the amplitude (which controls the CEP phase) and the phase (which moves the discontinuity at 800 nm to the right or the left) to distribute the power between the two pulses. The evolutionary algorithm is used to find the right combination of parameters efficiently. An algorithm like this excels at exactly this kind of problem. Its operating principles were established in section (3.4). The target trace is created dynamically. The current THz trace is parsed and the oscillatory values are replaced by a constant value determined from the first few data points as indicated by the red line in Fig. 5.2. The sum of squares of the difference between the black and the red

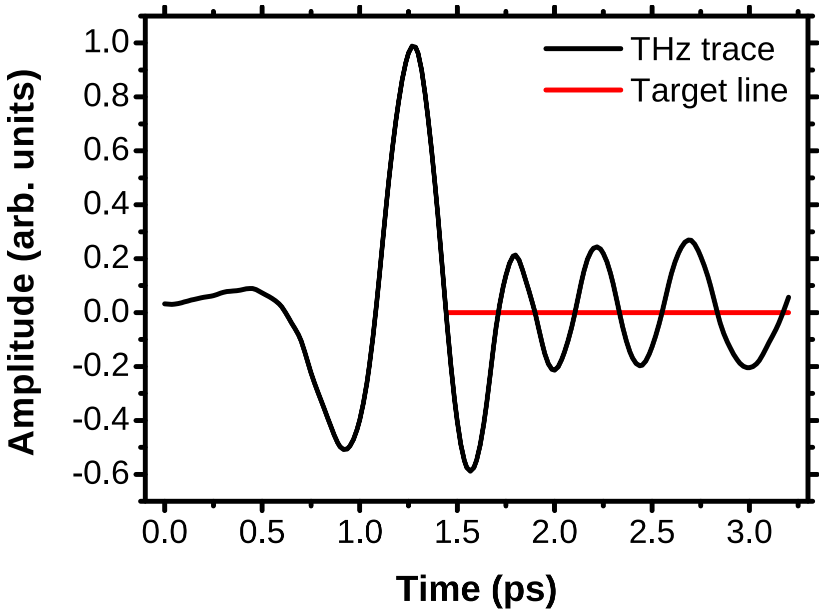

Figure 5.2: The fitness of the THz trace is determined by the sum of squares of the difference between the black and the red line.

line is used as the figure of merit for the algorithm, which from here on is named fitness.

A THz trace is recorded for each individual of the generation. In order to keep the measurement time for each generation to one hour, each generation consists of 49 individuals, which proved to be a sufficiently sized sample. Of these 49, the best seven were selected to act as parents. 35 individuals are bred through recombination and 14 through mutation. These 49 descendants together form the new generation that is to be tested. Swift convergence is achieved through careful selection of the boundaries for the free parameters, which are determined separately. The remaining parameter space is too large for brute force methods. The solution will emerge in a few generations out of the initial random gene pool through algorithmically determined iteration steps.

## 5.2 The Single-Cycle THz Pulse

The outcome of the experiment for a temporal separation of a few tens of fs is presented in Fig. 5.3. In order to make the traces comparable with each other, a special normalization scheme is used. The peak-to-peak amplitude from the first valley to the first peak is adjusted to unity. This enables a direct comparison of the shape and the efficient suppression of the oscillations, even if the overall THz output drops which is due to happen in these long-running experiments. The THz spectrum of the reference shape has a pronounced peak at 2 THz which is attenuated after the optimization, as predicted, see Fig. 5.4.

The fitness of the reference THz trace is used to normalize the data, and together with the normalization scheme for the THz traces enables the direct comparison of the efficacy for the process. Convergence is swift. An initial solution is found after only a few generations, as shown in Fig. 5.5. This is further refined in the next steps, visible in the downward trend of the remainder of the histogram.

It appears that the best results are achieved with the rectangular mask, while the least effective mask is the reversed 2-color mask. This is somewhat unexpected, as the 2-color mask is generally the more versatile choice. It may have been

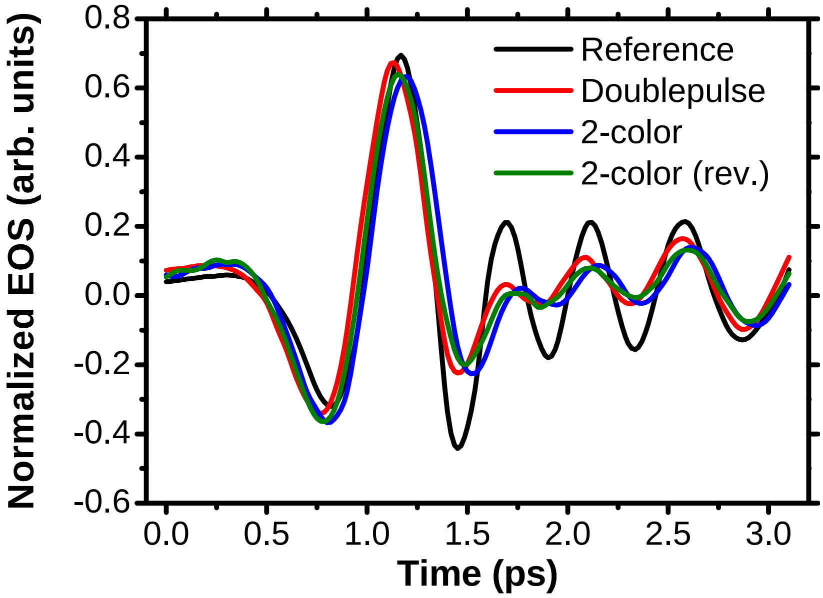

Figure 5.3: Result of the single-cycle THz optimization (time-domain). The optimization only affects the oscillations and leaves the first part of the THz trace unchanged.

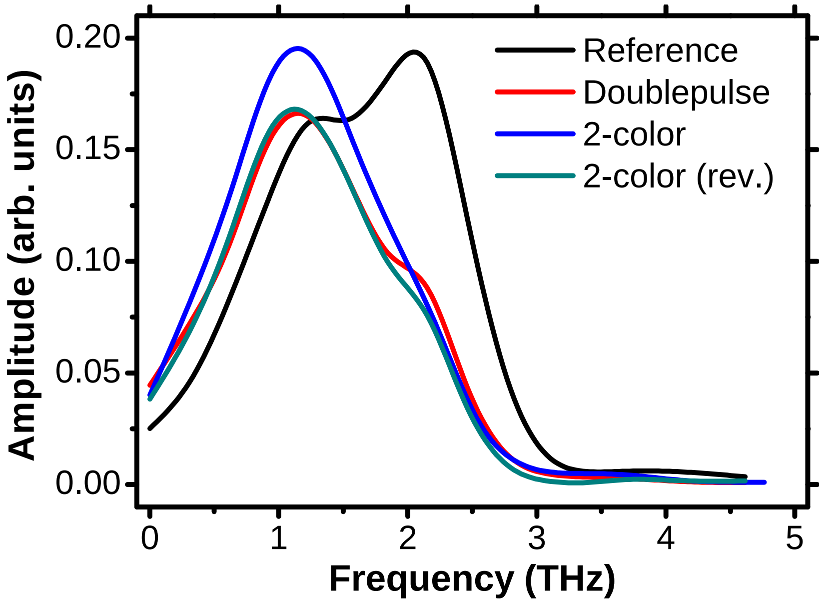

Figure 5.4: Result of the single-cycle THz optimization (frequency-domain). Note that the main change of the spectrum is in the region around 2 THz.

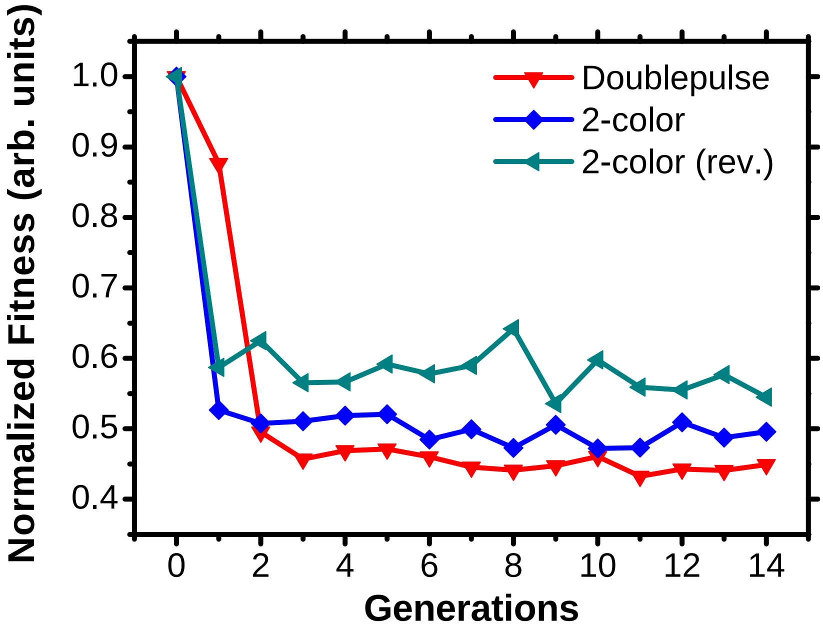

Figure 5.5: Histogram of the single-cycle optimization process. Conversion is swift, the optimal shape is found after a few generations. The rectangular mask seems to be the most efficient mask for this task, which is puzzling, as the 2-color mask is more versatile. Its performance could have been undermined by the awkward definition of the mask.

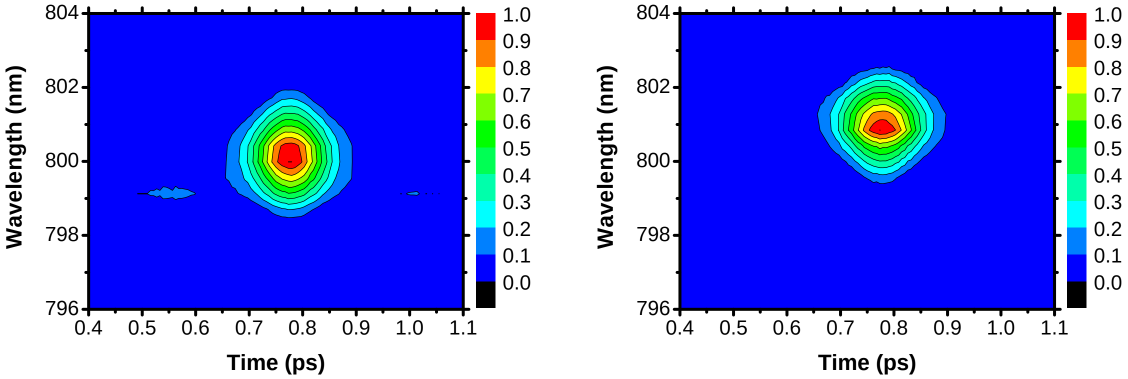

(a) Rectangular phase mask

(b) 2-color phase mask

Figure 5.6: FROG traces of the laser pulses associated with the optimized THz shape. Both pulses reveal their limited bandwidth. Additionally, the color shift of the 2-color mask is visible.

handicapped by the awkward definition of the mask. But, the algorithm finds a suitable solution even under these constraints.

The suppression of the oscillations comes at a cost. The THz amplitude is reduced by about 20%, while the measured reduction of the oscillations is close to 50%. It is remarkable, that the first part of the THz pulse shape remains undisturbed. The spectral shaping has no influence beyond the oscillations. A look at the parameters of the successful individuals indicate that the optimal shape has a CEP phase that is very close to $\pi$, which is not surprising considering the results of the model. It is also sufficient to send a weak second pulse, in order not to lose too much of the signal strength.

A look at the FROG pictures of the best individual for the rectangular (Fig. 5.6a) and the 2-color mask (Fig. 5.6b) reveals the limited bandwidth of the laser pulse itself. The reduction is comparable, and the color shift of the second mask is clearly visible.

## 5.3 The Double-Cycle THz Pulse

This section will explore the feasibility to truly engineer THz waveforms to specification. The goal is to introduce a second THz peak and control its oscillatory behavior. The properties of the 2-color pulse and especially the malleability of its pulse envelope make it a strong candidate.

The shape of the phase mask is straightforwardly deduced from the tasks it must accomplish. The second THz peak is created by delaying a slice of the spectrum by the desired time. The length of the common THz trace is on the order of a few picoseconds, depending on the number of oscillations that are counted. The suppression of the oscillations only extends to the first two or three, which translates to a pulse length of 2 ps. The second THz pulse is set to appear 2 ps after the first main lobe. Two additional pulses need to be introduced to make the phase envelopes shapeable. This requires a mask with three slopes that leads to four pulses in total. The final shape of the phase mask is presented in Fig. 5.7.

The two large spectral slices generate the two main THz peaks. The first and last slope are set to time delays of 200 fs after the first and second peak respectively, in order to adjust the pulse envelope. The time delay of the auxiliary pulses was

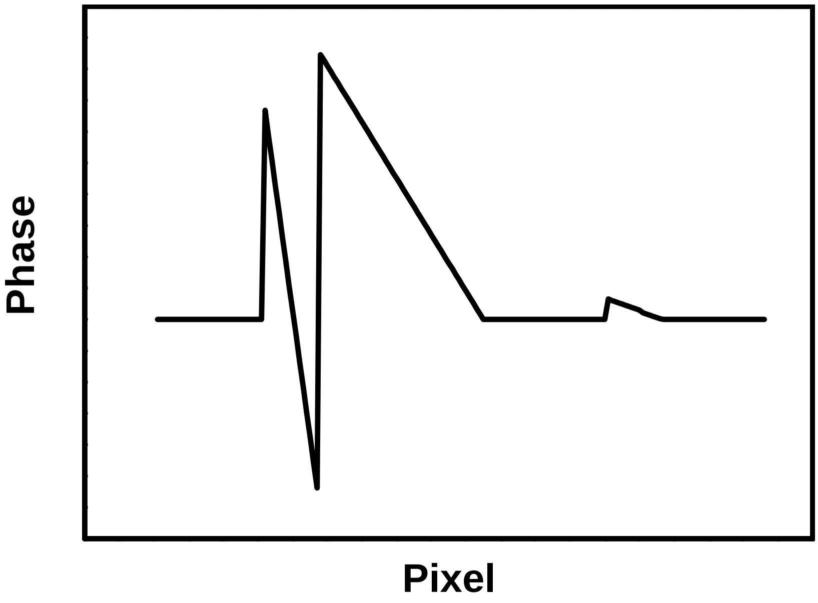

Figure 5.7: Shape of the phase mask used to produce the double-cycle THz pulse. The mask is built to create two pulse-pairs at two different times. The two main spectral slices create the THz pulses, the two auxiliary pulses are needed to control the shape of the final THz double-cycle pulse.

arbitrarily set, as the exact position is only of minor importance. In total, 10 parameters are necessary to generate the mask. Nine control the boundaries of the spectral slices and the slopes. The tenth is used as an offset between the first and second slope, which is a useful extra parameter. Six of the 10 parameters are determined by the algorithm. The outer boundaries and the slope of the second main THz pulse remain fixed. The fitness of the THz trace was determined by splitting the trace at predetermined positions and using the same valuation as above.

The ability of the setup to find a solution by itself is very effectively demonstrated in Fig. 5.8. It takes a few generations for the ideal solution to appear, which is appropriate for the large number of parameters, see Fig. 5.9. A twist was used in this example to facilitate convergence. The size of the first generation was tripled, while at the same time decreasing the number of individuals in a generation to 42. With this measure the initial boundary conditions can be set more generously. All in all this reduces the overall amount of time until a solution is found, as it reduces the amount of preliminary work and could prevent runs without a good solution.

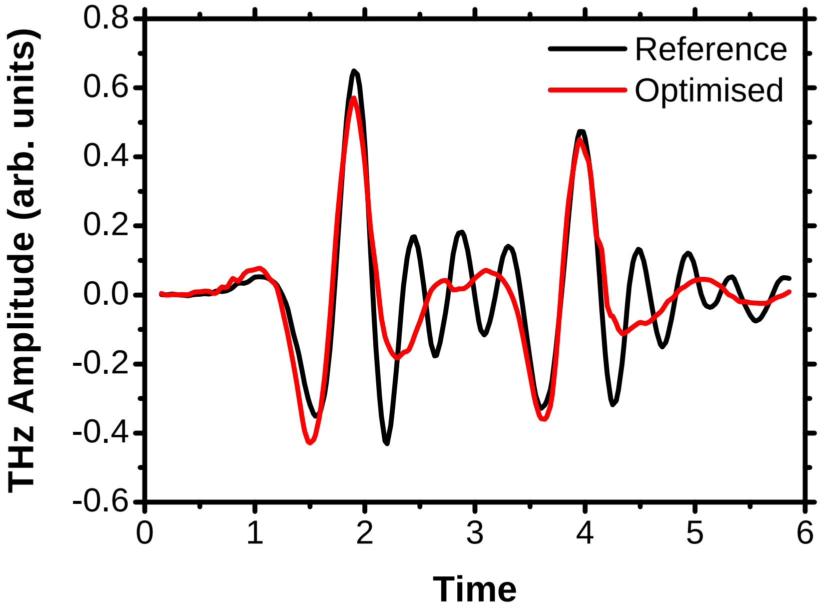

Figure 5.8: Result of the double-cycle optimization. The interaction of the two pulse-pairs creates the desired shape. Again, the first part of the THz trace remains unchanged, while the oscillatory part is shaped.

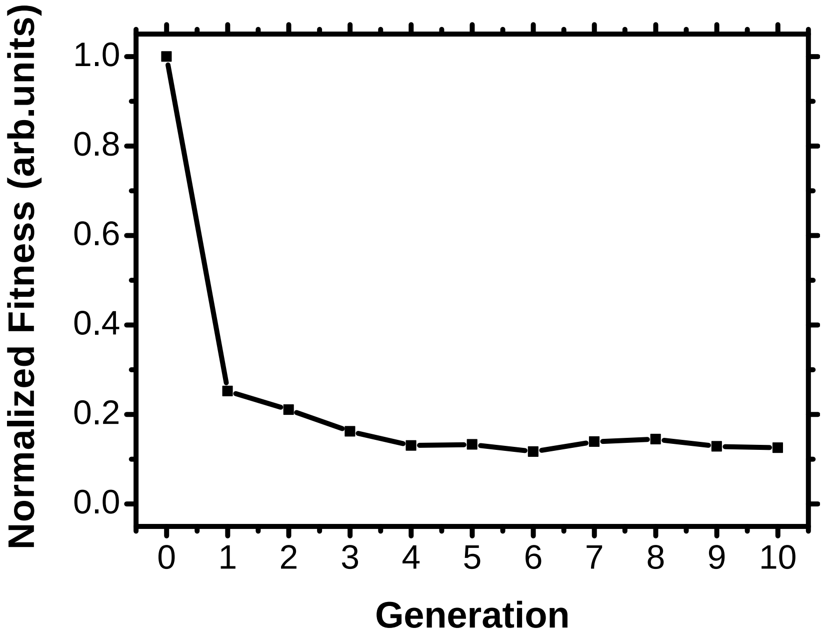

Figure 5.9: Histogram of the double-cycle optimization process. Conversion is swift, the optimized shape is found after a few generations.

## 5.4 Conclusions

These experiments have shown that the feedback-controlled system is fully operational and could prove to be a useful addition to the available arsenal of tools in the laboratory. The creation of the double-cycle pulse demonstrates the versatility of the concept. The degrees of freedom available with the 2-color mask should initially provide enough design possibilities to create fully customized THz traces.

The most important component of the setup is the evolutionary algorithm. It is used here in a straightforward implementation, with a variable step-length. This is sufficient to produce excellent agreement between the target and the specimen. It accomplishes good results even if the underlying process is not understood, as long as it is allowed to access the relevant parameter space. This independence of reason is its greatest strength.

The next steps to improve the efficacy of the method would merge the model of the previous chapter with the evolutionary algorithm. With congruence between the dispersions in the setup and the model this would significantly reduce the amount of time needed to fix the boundaries and could help find solutions without the rigidly defined masks.

# 6 Concluding Remarks

The many strengths of the coherent-control paradigm were described in section 2.2. The interference of two electromagnetic fields reveals a new degree of freedom that influences a measurable quantity. It is an enabling technology that is useful to predict and probe effects that are not directly accessible and hidden behind a visible signature. This is especially true when optimal control techniques are used to experimentally "solve" a Hamiltonian in a trial-and-error approach. All of the pulse properties are usable as levers, either alone or in combination. Some examples include the phase, the carrier envelope phase, the intensity, the polarization, the shape of the pulse envelope, or the temporal separation of pulse trains.

The goal of the presented experiments was to introduce a new coherent-control scheme that uses the relative carrier envelope phase (CEP) between a pulse pair as the control mechanism. A phase-stable pulse pair and direct access to the CEP are provided by a special phase shaping mask that is applied to a liquid crystal mask that is in the center of a 4f pulse shaper setup. Variation of the CEP forces a shift of the second electric field relative to the first (Fig. 4.13), causing dramatic changes of the pulse envelope shape.

The THz emission of shift and rectification currents in GaAs and ZnTe, respectively, are the ideal model system to show this. Their existence is linked to divergences of the optical susceptibility for the limit ($\omega \rightarrow 0$) (section 2.3), and, as $\chi^{(2)}$ processes, they are very sensitive to changes of the pulse envelope. This becomes tangible with equations (2.98) & (2.99) that describe the relation between the mixing of two electric fields and the generation of the currents. Shift currents directly follow the pulse envelope, while rectification currents follow its time derivative. The link between the evolution of the currents and the emitted THz radiation is explained with a straightforward model (section 3.3). In a first step this creates expressions for the real THz trace and spectrum. But the limited bandwidth of the electro-optical sampling (EOS) distorts these in the experiments. A simple model of the EOS process was implemented to make the outputs comparable. Very surprising results were obtained regarding the shape of the THz trace and its associated spectrum.

The results of the experiment are unambiguous and reproducible. The variation of the relative CEP produces an oscillatory pattern of the emitted THz radiation (see, e.g., Fig. 4.14). The model is able to replicate the pattern (Fig. 4.19) and thus enables access to the behavior of the current density (Fig. 4.20). A closer look at the current density for select values of the CEP supplies the explanation (Fig. 4.21). The time separation of this example is set to $\tau = 60fs$ which is smaller than the temporal FWHM of the laser pulse. The second peak is only visible in the current density for nonzero values of the CEP. Its variation thus sets which of the peaks is dominant. This effect is explored for two phase masks (Fig. 4.11 & Fig. 4.12) for two temporal separations ($\tau = 60fs$ & $\tau = 200fs$) to discern additional particularities. Two things stand out. First, the rectangular phase mask generates highly structured current density patterns that are also visible in the THz emission pattern. Second, the malleability of the 2-color phase mask which is highly suitable to shape THz traces.

The generation of completely arbitrary THz traces was the second topic considered in this dissertation. The fundamental goal was to build a self-learning machine that creates THz traces according to specification. The evolutionary algorithm is the vital center of this system. It controls the creation and assessment of the phase masks that control the rectification current generation process (section 3.2). The large oscillations that appear after the main peak are a good model system. The functional ability of the system is demonstrated by morphing the multi-cycle THz trace to a single-cycle shape. The system performs admirably and delivers a solution after only a few generations (Fig. 5.3). The attenuation of the oscillations is attributed to the shaped THz spectrum that loses its dominant peak at 2 THz (Fig. 5.4). This concurs with the findings of section 4.2.2. The introduction of the second pulse causes a constriction in the THz spectrum that influences overlap between the real THz field and the transfer function of the electro-optical sampling process, in turn reducing the oscillations. Emboldened by this result, a second highly-structured THz trace was attempted, which consists of two consecutive single-cycle pulses and is named the double-cycle pulse. The 2-color mask can show its full potential here. A total of four pulses are created and positioned relative to each other (Fig. 5.7). Of the ten parameters that are needed to create the phase mask, six are controlled by the algorithm. This is a real challenge for the system. However, it still solved it in four generations (Fig. 5.8 & Fig. 5.9).

There still are a lot of challenges that should be explored. After having demonstrated the single and the double-cycle THz pulse, the next step is the creation of the half-cycle pulse. It is not clear a priori if and how this could be accomplished. Therefore the clever thing to do is to connect the model and the evolutionary algorithm and get a feel for the required shape of the laser pulse, before using the full setup.

Apart from that, the introduction of polarization shaping capabilities to the setup will be useful. It would be interesting to see, if the coherent-control scheme developed here also functions with cross-polarized beams.

Another idea involves using the amplitude mask to carve out two narrow slices out of the optical spectrum, about 1 nm FWHM and 4 nm apart. The 2-color mask is then used to delay one of the pulses. The emerging pattern has a very interesting feature in the first tens of femtoseconds. The theory group of John Sipe in Toronto is currently trying to replicate this in a model.

But this setup actually needs to be moved to a carrier-envelope-stabilized laser setup. The use of a pulse shaper mask as a CEP shifter has already been shown, but I believe the full potential of this combination remains to be explored [110].

# Bibliography

[1] C. Jördens and M. Koch. “Detection of foreign bodies in chocolate with pulsed terahertz spectroscopy.” Optical Engineering **47**, 037003+ (2008). url: `http://dx.doi.org/10.1117/1.2896597`. See p. 1.

[2] S. Wietzke et al. “Terahertz imaging: a new non-destructive technique for the quality control of plastic weld joints.” Journal of the European Optical Society: Rapid Publications **2**, 07013+ (2007). url: `http://dx.doi.org/10.2971/jeos.2007.07013`. See p. 1.

[3] S. Wietzke et al. “Terahertz time-domain spectroscopy as a tool to monitor the glass transition in polymers.” Optics Express **17**, 19006+ (2009). url: `http://dx.doi.org/10.1364/OE.17.019006`. See p. 1.

[4] N. Krumbholz et al. “Monitoring polymeric compounding processes inline with THz time-domain spectroscopy.” Polymer Testing **28**, 30–35 (2009). url: `http://dx.doi.org/10.1016/j.polymertesting.2008.09.009`. See p. 1.

[5] M. Nagel et al. “Integrated THz technology for label-free genetic diagnostics.” Applied Physics Letters **80**, 154+ (2002). url: `http://dx.doi.org/10.1063/1.1428619`. See p. 1.

[6] R. M. Woodward et al. “Terahertz pulse imaging in reflection geometry of human skin cancer and skin tissue.” Physics in Medicine and Biology **47**, 3853–3863 (2002). url: `http://dx.doi.org/10.1088/0031-9155/47/21/325`. See p. 1.

[7] F. Rutz et al. “Terahertz Quality Control of Polymeric Products.” International Journal of Infrared and Millimeter Waves **27**, 547–556 (2006). url: `http://dx.doi.org/10.1007/s10762-006-9106-7`. See p. 1.

[8] C. Jördens, M. Scheller, B. Breitenstein, D. Selmar, and M. Koch. “Evaluation of leaf water status by means of permittivity at terahertz frequencies.” Journal of Biological Physics **35**, 255–264 (2009). url: `http://dx.doi.org/10.1007/s10867-009-9161-0`. See p. 1.

[9] K. Fukunaga, Y. Ogawa, S. Hayashi, and I. Hosako. “Terahertz spectroscopy for art conservation.” IEICE Electronics Express **4**, 258–263 (2007). url: `http://dx.doi.org/10.1587/elex.4.258`. See p. 1.

[10] T. Kleine-Ostmann, K. Pierz, G. Hein, P. Dawson, and M. Koch. “Audio signal transmission over THz communication channel using semiconductor modulator.” Electronics Letters **40**, 124+ (2004). url: `http://dx.doi.org/10.1049/el:20040106`. See p. 1.

[11] N. Krumbholz et al. “Omnidirectional terahertz mirrors: A key element for future terahertz communication systems.” Applied Physics Letters **88**, 202905+ (2006). url: `http://dx.doi.org/10.1063/1.2205727`. See p. 1.

[12] R. Piesiewicz et al. “Short-Range Ultra-Broadband Terahertz Communications: Concepts and Perspectives.” IEEE Antennas and Propagation Magazine **49**, 24–39 (2007). url: `http://dx.doi.org/10.1109/MAP.2007.4455844`. See p. 1.

[13] R. Piesiewicz, M. Jacob, M. Koch, J. Schoebel, and T. Kürner. “Performance Analysis of Future Multigigabit Wireless Communication Systems at THz Frequencies With Highly Directive Antennas in Realistic Indoor Environments.” IEEE Journal of Selected Topics in Quantum Electronics **14**, 421–430 (2008). url: `http://dx.doi.org/10.1109/JSTQE.2007.910984`. See p. 1.

[14] I. A. Ibraheem, N. Krumbholz, D. Mittleman, and M. Koch. “Low-Dispersive Dielectric Mirrors for Future Wireless Terahertz Communication Systems.” IEEE Microwave and Wireless Components Letters **18**, 67–69 (2008). url: `http://dx.doi.org/10.1109/LMWC.2007.912050`. See p. 1.

[15] K. Kawase, Y. Ogawa, Y. Watanabe, and H. Inoue. “Non-destructive terahertz imaging of illicit drugs using spectral fingerprints.” Opt. Express **11**, 2549–2554 (2003). url: `http://www.opticsinfobase.org/abstract.cfm?id=76830`. See p. 1.

[16] Y. C. Shen et al. “Detection and identification of explosives using terahertz pulsed spectroscopic imaging.” Applied Physics Letters **86**, 241116+ (2005). url: `http://dx.doi.org/10.1063/1.1946192`. See p. 1.

[17] C. Jördens et al. “Fibre-coupled terahertz transceiver head.” Electronics Letters **44**, 1473+ (2008). url: `http://dx.doi.org/10.1049/el:20083017`. See p. 1.

[18] M. C. Kemp et al. “Security applications of terahertz technology.” Ed. by R. J. Hwu and D. L. Woolard. Terahertz for Military and Security Applications **5070**, 44–52 (2003). url: `http://dx.doi.org/10.1117/12.500491`. See p. 1.

[19] A. Semenov, H. Richter, U. Böttger, and H. W. Hübers. “Imaging terahertz radar for security applications.” Ed. by J. O. Jensen, H. L. Cui, D. L. Woolard, and R. J. Hwu. Terahertz for Military and Security Applications VI **6949**, 694902+ (2008). url: `http://dx.doi.org/10.1117/12.778477`. See p. 1.

[20] B. B. Hu and M. C. Nuss. “Imaging with terahertz waves.” Optics Letters **20**, 1716+ (1995). url: `http://dx.doi.org/10.1364/OL.20.001716`. See p. 1.

[21] D. M. Mittleman, S. Hunsche, L. Boivin, and M. C. Nuss. “T-ray tomography.” Optics Letters **22**, 904–906 (1997). url: `http://dx.doi.org/10.1364/OL.22.000904`. See p. 1.

[22] S. Wang, B. Ferguson, D. Abbott, and X. C. Zhang. “T-ray Imaging and Tomography.” Journal of Biological Physics **29**, 247–256 (2003). url: `http://dx.doi.org/10.1023/A:1024457212578`. See p. 1.

[23] B. Ferguson, S. Wang, D. Gray, D. Abbot, and X. C. Zhang. “T-ray computed tomography.” Optics Letters **27**, 1312–1314 (2002). url: `http://dx.doi.org/10.1364/OL.27.001312`. See p. 1.

[24] D. H. Auston, K. P. Cheung, J. A. Valdmanis, and D. A. Kleinman. “Cherenkov Radiation from Femtosecond Optical Pulses in Electro-Optic Media.” Physical Review Letters **53**, 1555–1558 (1984). url: `http://dx.doi.org/10.1103/PhysRevLett.53.1555`. See p. 1.

[25] D. H. Auston and K. P. Cheung. “Coherent time-domain far-infrared spectroscopy.” J. Opt. Soc. Am. B **2**, 606–612 (1985). url: `http://dx.doi.org/10.1364/JOSAB.2.000606`. See p. 1.

[26] R. Köhler et al. “Terahertz semiconductor-heterostructure laser.” Nature **417**, 156–159 (2002). url: `http://dx.doi.org/10.1038/417156a`. See p. 1.

[27] H. Ito, F. Nakajima, T. Furuta, and T. Ishibashi. “Continuous THz-wave generation using antenna-integrated uni-travelling-carrier photodiodes.” Semiconductor Science and Technology **20**, S191–S198 (2005). url: `http://dx.doi.org/10.1088/0268-1242/20/7/008`. See p. 1.

[28] T. Otsuji, M. Hanabe, T. Nishimura, and E. Sano. “A grating-bicoupled plasma-wave photomixer with resonant-cavity enhanced structure.” Opt. Express **14**, 4815–4825 (2006). url: `http://dx.doi.org/10.1364/OE.14.004815`. See p. 1.

[29] A. Sell, A. Leitenstorfer, and R. Huber. “Phase-locked generation and field-resolved detection of widely tunable terahertz pulses with amplitudes exceeding 100 MV/cm.” Opt. Lett. **33**, 2767–2769 (2008). url: `http://dx.doi.org/10.1364/OL.33.002767`. See p. 1.

[30] J. R. Danielson et al. “Interaction of Strong Single-Cycle Terahertz Pulses with Semiconductor Quantum Wells.” Physical Review Letters **99**, 237401+ (2007). url: `http://dx.doi.org/10.1103/PhysRevLett.99.237401`. See p. 1.

[31] G. Gunter et al. “Sub-cycle switch-on of ultrastrong light-matter interaction.” Nature **458**, 178–181 (2009). url: `http://dx.doi.org/10.1038/nature07838`. See p. 1.

[32] M. Bass, P. A. Franken, J. F. Ward, and G. Weinreich. “Optical Rectification.” Physical Review Letters **9**, 446–448 (1962). url: `http://dx.doi.org/10.1103/PhysRevLett.9.446`. See p. 1.

[33] J. B. Khurgin. “Optical rectification and terahertz emission in semiconductors excited above the band gap.” J. Opt. Soc. Am. B **11**, 2492–2501 (1994). url: `http://dx.doi.org/10.1364/JOSAB.11.002492`. See p. 1.

[34] J. B. Khurgin. “Dispersion and anisotropy of optical rectification in zinc blende quantum wells.” J. Opt. Soc. Am. B **13**, 2129–2140 (1996). url: `http://dx.doi.org/10.1364/JOSAB.13.002129`. See pp. 1, 34.

[35] K. Wynne and J. Carey. “An integrated description of terahertz generation through optical rectification, charge transfer, and current surge.” Optics Communications **256**, 400–413 (2005). url: `http://dx.doi.org/10.1016/j.optcom.2005.06.065`. See pp. 1, 51.

[36] J. E. Sipe and A. I. Shkrebtii. “Second-order optical response in semiconductors.” Physical Review B **61**, 5337+ (2000). url: `http://dx.doi.org/10.1103/PhysRevB.61.5337`. See pp. 2, 24, 25, 28, 106.

[37] F. Nastos and J. E. Sipe. “Optical rectification and shift currents in GaAs and GaP response: Below and above the band gap.” Physical Review B **74**, 035201+ (2006). url: `http://dx.doi.org/10.1103/PhysRevB.74.035201`. See pp. 2, 29–31, 106.

[38] T. C. Weinacht, J. Ahn, and P. H. Bucksbaum. “Controlling the shape of a quantum wavefunction.” Nature **397**, 233–235 (1999). url: `http://dx.doi.org/10.1038/16654`. See p. 2.

[39] R. Bartels et al. “Shaped-pulse optimization of coherent emission of high-harmonic soft X-rays.” Nature **406**, 164–166 (2000). url: `http://dx.doi.org/10.1038/35018029`. See p. 2.

[40] B. von Vacano and M. Motzkus. “Time-resolved two color single-beam CARS employing supercontinuum and femtosecond pulse shaping.” Optics Communications **264**, 488–493 (2006). url: `http://dx.doi.org/10.1016/j.optcom.2006.02.065`. See pp. 2, 39.

[41] B. von Vacano, T. Buckup, and M. Motzkus. “Highly sensitive single-beam heterodyne coherent anti-Stokes Raman scattering.” Opt. Lett. **31**, 2495–2497 (2006). url: `http://dx.doi.org/10.1364/OL.31.002495`. See p. 2.

[42] M. Aeschlimann et al. “Adaptive subwavelength control of nano-optical fields.” Nature **446**, 301–304 (2007). url: `http://dx.doi.org/10.1038/nature05595`. See p. 2.

[43] T. Brixner et al. “Quantum Control by Ultrafast Polarization Shaping.” Physical Review Letters **92**, 208301+ (2004). url: `http://dx.doi.org/10.1103/PhysRevLett.92.208301`. See p. 2.

[44] A. M. Weiner. “Femtosecond pulse shaping using spatial light modulators.” Review of Scientific Instruments **71**, 1929–1960 (2000). url: `http://dx.doi.org/10.1063/1.1150614`. See pp. 2, 53.

[45] G. Stobrawa et al. “A new high-resolution femtosecond pulse shaper.” Applied Physics B: Lasers and Optics **72**, 627–630 (2001). url: `http://dx.doi.org/10.1007/s003400100576`. See p. 2.

[46] Y. B. Band. *Light and Matter*. England: Wiley & Sons, 2006. See p. 4.

[47] R. W. Boyd. *Nonlinear Optics*. 3rd. Academic Press, 2008. See pp. 5, 12.

[48] A. Vaupel. “Aufbau eines adaptiven Messsystems zur kohärenten Kontrolle von Terahertzwellenformen am Beispiel eines Single-Cycle-Pulses.” Diplomarbeit. Philipps-Universität Marburg, 2008. See pp. 6, 47.

[49] H. Haug and S. W. Koch. *Quantum Theory of the Optical and Electronc Properties of Semiconductors*. 5th. Singapore: World Scientific, 2009. See pp. 7, 9.

[50] H. M. van Driel and J. E. Sipe. “Ultrafast Phenomena in Semiconductors.” In: ed. by K.-T. Tsen. Springer-Verlag, 2001. Chap. 5: Coherence Control of Photocurrents in Semiconductors, 261–307. See pp. 13, 14, 16.

[51] L. Costa, M. Betz, M. Spasenovic, A. D. Bristow, and H. M. van Driel. “All-optical injection of ballistic electrical currents in unbiased silicon.” Nature Physics **3**, 632–635 (2007). url: `http://dx.doi.org/10.1038/nphys674`. See p. 14.

[52] M. Spasenović, M. Betz, L. Costa, and H. M. van Driel. “All-optical coherent control of electrical currents in centrosymmetric semiconductors.” Physical Review B **77**, 085201+ (2008). url: `http://dx.doi.org/10.1103/PhysRevB.77.085201`. See p. 14.

[53] R. Atanasov, A. Haché, J. L. P. Hughes, H. M. van Driel, and J. E. Sipe. “Coherent Control of Photocurrent Generation in Bulk Semiconductors.” Physical Review Letters **76**, 1703–1706 (1996). url: `http://dx.doi.org/10.1103/PhysRevLett.76.1703`. See pp. 14, 16.

[54] M. J. Stevens et al. “Optical injection and coherent control of a ballistic charge current in GaAs/AlGaAs quantum wells.” Journal of Applied Physics **94**, 4999–5004 (2003). url: `http://dx.doi.org/10.1063/1.1609639`. See pp. 15–17, 19.

[55] A. Haché et al. “Observation of Coherently Controlled Photocurrent in Unbiased, Bulk GaAs.” Physical Review Letters **78**, 306–309 (1997). url: `http://dx.doi.org/10.1103/PhysRevLett.78.306`. See p. 15.

[56] A. Haché, J. E. Sipe, and H. M. van Driel. “Quantum interference control of electrical currents in GaAs.” Quantum Electronics, IEEE Journal of **34**, 1144–1154 (1998). url: `http://dx.doi.org/10.1109/3.687857`. See p. 15.

[57] R. Fiederling et al. “Injection and detection of a spin-polarized current in a light-emitting diode.” Nature **402**, 787–790 (1999). url: `http://dx.doi.org/10.1038/45502`. See p. 18.

[58] Y. Ohno et al. “Electrical spin injection in a ferromagnetic semiconductor heterostructure.” Nature **402**, 790–792 (1999). url: `http://dx.doi.org/10.1038/45509`. See p. 18.

[59] F. Meier and B. P. Zakharchenya. *Optical Orientation (Modern Problems in Condensed Matter Sciences, Vol 8)*. Ed. by F. Meier and B. P. Zakharchenya. Elsevier Science Ltd, 1984. isbn: 0444867414. See p. 18.

[60] M. J. Stevens, A. L. Smirl, R. D. R. Bhat, J. E. Sipe, and H. M. van Driel. "Coherent control of an optically injected ballistic spin-polarized current in bulk GaAs." Journal of Applied Physics **91**, 4382–4386 (2002). url: `http://dx.doi.org/10.1063/1.1456943`. See pp. 18, 19, 22.

[61] R. D. R. Bhat and J. E. Sipe. "Optically Injected Spin Currents in Semiconductors." Physical Review Letters **85**, 5432–5435 (2000). url: `http://dx.doi.org/10.1103/PhysRevLett.85.5432`. See pp. 19, 20.

[62] A. Najmaie, R. D. R. Bhat, and J. E. Sipe. "All-optical injection and control of spin and electrical currents in quantum wells." Physical Review B **68**, 165348+ (2003). url: `http://dx.doi.org/10.1103/PhysRevB.68.165348`. See pp. 19, 20.

[63] J. Hübner et al. "Direct Observation of Optically Injected Spin-Polarized Currents in Semiconductors." Physical Review Letters **90**, 216601+ (2003). url: `http://dx.doi.org/10.1103/PhysRevLett.90.216601`. See pp. 20, 23.

[64] M. J. Stevens et al. "Quantum Interference Control of Ballistic Pure Spin Currents in Semiconductors." Physical Review Letters **90**, 136603+ (2003). url: `http://dx.doi.org/10.1103/PhysRevLett.90.136603`. See pp. 20–22.

[65] H. Zhao, A. L. Smirl, and H. M. van Driel. "Temporally and spatially resolved ballistic pure spin transport." Physical Review B **75**, 075305+ (2007). url: `http://dx.doi.org/10.1103/PhysRevB.75.075305`. See p. 23.

[66] H. Zhao et al. "Injection of ballistic pure spin currents in semiconductors by a single-color linearly polarized beam." Physical Review B **72**, 201302+ (2005). url: `http://dx.doi.org/10.1103/PhysRevB.72.201302`. See p. 23.

[67] J. D. Jackson. *Classical Electrodynamics*. 3rd. John Wiley & Sons, 1999. See p. 24.

[68] N. Laman, A. I. Shkrebtii, J. E. Sipe, and H. M. van Driel. "Quantum interference control of currents in CdSe with a single optical beam." Applied Physics Letters **75**, 2581–2583 (1999). url: `http://dx.doi.org/10.1063/1.125084`. See p. 28.

[69] M. Bieler, K. Pierz, U. Siegner, and P. Dawson. "Shift currents from symmetry reduction and Coulomb effects in (110)-orientated GaAs/$Al_{0.3}Ga_{0.7}As$ quantum wells." Physical Review B **76**, 161304+ (2007). url: `http://dx.doi.org/10.1103/PhysRevB.76.161304`. See pp. 33–35.

[70] M. Bieler, K. Pierz, U. Siegner, and P. Dawson. “Quantum interference currents by excitation of heavy- and light-hole excitons in GaAs/$Al_{0.3}Ga_{0.7}As$ quantum wells.” Physical Review B **73**, 241312+ (2006). url: `http://dx.doi.org/10.1103/PhysRevB.73.241312`. See p. 33.

[71] S. Pfalz et al. “Optical orientation of electron spins in GaAs quantum wells.” Physical Review B **71**, 165305+ (2005). url: `http://dx.doi.org/10.1103/PhysRevB.71.165305`. See p. 33.

[72] M. Bieler. “THz Generation From Resonant Excitation of Semiconductor Nanostructures: Investigation of Second-Order Nonlinear Optical Effects.” IEEE Journal of Selected Topics in Quantum Electronics **14**, 458–469 (2008). url: `http://dx.doi.org/10.1109/JSTQE.2007.910559`. See p. 35.

[73] M. Bieler, K. Pierz, and U. Siegner. “Simultaneous generation of shift and injection currents in (110)-grown GaAs/AlGaAs quantum wells.” Journal of Applied Physics **100**, 083710+ (2006). url: `http://dx.doi.org/10.1063/1.2360380`. See p. 35.

[74] N. Laman, M. Bieler, and H. M. van Driel. “Ultrafast shift and injection currents observed in wurtzite semiconductors via emitted terahertz radiation.” Journal of Applied Physics **98**, 103507+ (2005). url: `http://dx.doi.org/10.1063/1.2131191`. See pp. 35, 36.

[75] D. Côté, J. M. Fraser, M. DeCamp, P. H. Bucksbaum, and H. M. van Driel. “THz emission from coherently controlled photocurrents in GaAs.” Applied Physics Letters **75**, 3959–3961 (1999). url: `http://dx.doi.org/10.1063/1.125531`. See pp. 36, 37.

[76] D. Côté, N. Laman, and H. M. van Driel. “Rectification and shift currents in GaAs.” Applied Physics Letters **80**, 905+ (2002). url: `http://dx.doi.org/10.1063/1.1436530`. See p. 37.

[77] A. E. Siegman. *Lasers*. University Science Books, 1986. See p. 38.

[78] F. Träger, ed. *Springer Handbook of Lasers and Optics*. Springer, 2007. See pp. 38, 40.

[79] S. T. Cundiff and J. Ye. “Colloquium: Femtosecond optical frequency combs.” Reviews of Modern Physics **75**, 325–342 (2003). url: `http://dx.doi.org/10.1103/RevModPhys.75.325`. See pp. 38, 39.

[80] T. Udem, R. Holzwarth, and T. W. Hansch. “Optical frequency metrology.” Nature **416**, 233–237 (2002). url: `http://dx.doi.org/10.1038/416233a`. See p. 39.

[81] R. Trebino. *Frequency-resolved Optical Gating: The Measurement of Ultrashort Laser Pulses*. Springer, 2000. See pp. 42, 54, 55, 71.

[82] T. Grunwald. "Aufbau eines Terahertz-Time-Domain-Spektrometers zur Untersuchung von THz-Absorption durch intraexzitonische Übergänge in (GaIn)As-Quantenfilmen." Diplomarbeit. Philipps-Universität Marburg, 2006. See p. 47.

[83] D. Köhler. "THz-Time-Domain-Spektroskopie an zweidimensionalen Halbleiterstrukturen." Diplomarbeit. Philipps-Universität Marburg, 2007. See p. 47.

[84] T. Jung. "Terahertz-Spektroskopie zur Untersuchung von intraexzitonischen und plasmonischen Übergängen in (GaIn)As/GaAs-Multi-Quantenfilmen." Diplomarbeit. Philipps-Universität Marburg, 2008. See p. 47.

[85] T. Grunwald. "Terahertz-Antwort von zweidimensionalen Ladungsträgersystemen in GaAs-basierten Heterostrukturen." Dissertation. Philipps-Universität Marburg, 2009. See p. 47.

[86] K. K. Kohli, A. Vaupel, S. Chatterjee, and W. W. Rühle. "Adaptive shaping of THz-pulses generated in <110> ZnTe crystals." J. Opt. Soc. Am. B **26**, A74–A78 (2009). url: `http://dx.doi.org/10.1364/JOSAB.26.000A74`. See pp. 48, 105.

[87] A. Dreyhaupt, S. Winnerl, T. Dekorsy, and M. Helm. "High-intensity terahertz radiation from a microstructured large-area photoconductor." Applied Physics Letters **86**, 121114+ (2005). url: `http://dx.doi.org/10.1063/1.1891304`. See pp. 47, 105.

[88] Q. Wu and X. C. Zhang. "7 terahertz broadband GaP electro-optic sensor." Applied Physics Letters **70**, 1784–1786 (1997). url: `http://dx.doi.org/10.1063/1.118691`. See pp. 51, 60.

[89] G. Gallot and D. Grischkowsky. "Electro-optic detection of terahertz radiation." J. Opt. Soc. Am. B **16**, 1204–1212 (1999). url: `http://dx.doi.org/10.1364/JOSAB.16.001204`. See p. 51.

[90] *Technical Documentation - SLM-S640d SLM-320d - V3.* Jenoptik. 2006. See p. 53.

[91] A. Nahata, A. S. Weling, and T. F. Heinz. "A wideband coherent terahertz spectroscopy system using optical rectification and electro-optic sampling." Applied Physics Letters **69**, 2321–2323 (1996). url: `http://dx.doi.org/10.1063/1.117511`. See p. 63.

[92] H. Rabitz, R. de Vivie-Riedle, M. Motzkus, and K. Kompa. “Whither the Future of Controlling Quantum Phenomena?” Science **288**, 824–828 (2000). url: `http://dx.doi.org/10.1126/science.288.5467.824`. See p. 67.

[93] D. Zeidler, S. Frey, K. L. Kompa, and M. Motzkus. “Evolutionary algorithms and their application to optimal control studies.” Physical Review A **64**, 023420+ (2001). url: `http://dx.doi.org/10.1103/PhysRevA.64.023420`. See p. 67.

[94] J. L. Herek, W. Wohlleben, R. J. Cogdell, D. Zeidler, and M. Motzkus. “Quantum control of energy flow in light harvesting.” Nature **417**, 533–535 (2002). url: `http://dx.doi.org/10.1038/417533a`. See p. 67.

[95] H. R. Telle et al. “Carrier-envelope offset phase control: A novel concept for absolute optical frequency measurement and ultrashort pulse generation.” Applied Physics B: Lasers and Optics **69**, 327–332 (1999). url: `http://dx.doi.org/10.1007/s003400050813`. See p. 82.

[96] D. J. Jones et al. “Carrier-Envelope Phase Control of Femtosecond Mode-Locked Lasers and Direct Optical Frequency Synthesis.” Science **288**, 635–639 (2000). url: `http://dx.doi.org/10.1126/science.288.5466.635`. See p. 82.

[97] P. A. Roos et al. “Solid-state carrier-envelope phase stabilization via quantum interference control of injected photocurrents.” Opt. Lett. **30**, 735–737 (2005). url: `http://dx.doi.org/10.1364/OL.30.000735`. See p. 82.

[98] H. O. Moser, B. D. F. Casse, O. Wilhelmi, and B. T. Saw. “Terahertz Response of a Microfabricated Rod–Split-Ring-Resonator Electromagnetic Metamaterial.” Physical Review Letters **94**, 063901+ (2005). url: `http://dx.doi.org/10.1103/PhysRevLett.94.063901`. See p. 105.

[99] H. O. Moser et al. “Free-standing THz electromagneticmetamaterials.” Opt. Express **16**, 13773–13780 (2008). url: `http://dx.doi.org/10.1364/OE.16.013773`. See p. 105.

[100] P. Y. Han, G. C. Cho, and X. C. Zhang. “Time-domain transillumination of biological tissues with terahertz pulses.” Opt. Lett. **25**, 242–244 (2000). url: `http://dx.doi.org/10.1364/OL.25.000242`. See p. 105.

[101] E. Knoesel, M. Bonn, J. Shan, and T. F. Heinz. “Charge Transport and Carrier Dynamics in Liquids Probed by THz Time-Domain Spectroscopy.” Physical Review Letters **86**, 340–343 (2001). url: `http://dx.doi.org/10.1103/PhysRevLett.86.340`. See p. 105.

[102] R. Huber et al. “How many-particle interactions develop after ultrafast excitation of an electron-hole plasma.” Nature **414**, 286–289 (2001). url: `http://dx.doi.org/10.1038/35104522`. See p. 105.

[103] R. Huber et al. “Femtosecond Formation of Coupled Phonon-Plasmon Modes in InP: Ultrabroadband THz Experiment and Quantum Kinetic Theory.” Physical Review Letters **94**, 027401+ (2005). url: `http://dx.doi.org/10.1103/PhysRevLett.94.027401`. See p. 105.

[104] R. A. Kaindl, M. A. Carnahan, D. Hagele, R. Lovenich, and D. S. Chemla. “Ultrafast terahertz probes of transient conducting and insulating phases in an electron-hole gas.” Nature **423**, 734–738 (2003). url: `http://dx.doi.org/10.1038/nature01676`. See p. 105.

[105] T. Tanabe, K. Suto, J. Nishizawa, T. Kimura, and K. Saito. “Frequency-tunable high-power terahertz wave generation from GaP.” Journal of Applied Physics **93**, 4610–4615 (2003). url: `http://dx.doi.org/10.1063/1.1560573`. See p. 105.

[106] Y. S. Lee, N. Amer, and W. C. Hurlbut. “Terahertz pulse shaping via optical rectification in poled lithium niobate.” Applied Physics Letters **82**, 170–172 (2003). url: `http://dx.doi.org/10.1063/1.1535268`. See p. 106.

[107] Y. S. Lee, W. C. Hurlbut, K. L. Vodopyanov, M. M. Fejer, and V. G. Kozlov. “Generation of multicycle terahertz pulses via optical rectification in periodically inverted GaAs structures.” Applied Physics Letters **89**, 181104+ (2006). url: `http://dx.doi.org/10.1063/1.2367661`. See p. 106.

[108] J. Ahn, A. Efimov, R. Averitt, and A. Taylor. “Terahertz waveform synthesis via optical rectification of shaped ultrafast laser pulses.” Opt. Express **11**, 2486–2496 (2003). url: `http://www.opticsinfobase.org/abstract.cfm?id=75199`. See p. 106.

[109] H. J. Bakker, G. C. Cho, H. Kurz, Q. Wu, and X. C. Zhang. “Distortion of terahertz pulses in electro-optic sampling.” J. Opt. Soc. Am. B **15**, 1795–1801 (1998). url: `http://dx.doi.org/10.1364/JOSAB.15.001795`. See p. 106.

[110] M. Kakehata, H. Takada, Y. Kobayashi, and K. Torizuka. “Generation of optical-field controlled high-intensity laser pulses.” Journal of Photochemistry and Photobiology A: Chemistry **182**, 220–224 (2006). url: `http://dx.doi.org/10.1016/j.jphotochem.2006.05.025`. See p. 119.

# Publications

Kapil K. Kohli, Andreas Vaupel, Sangam Chatterjee, and Wolfgang W. Rühle: Adaptive shaping of THz-pulses generated in <110> ZnTe crystals. J. Opt. Soc. Am. B **26**, A74-A78 (2009). doi:10.1364/JOSAB.26.000A74

Additional publications are in preparation.

# Wissenschaftlicher Werdegang

Kapil Kumar Kohli
geboren am 20. März 1979 in Stuttgart

| | |
|---|---|
| 1998 | Abitur am Lise-Meitner-Gymnasium Böblingen |
| 1998 - 2001 | Studium der Soziologie an der Philipps-Universität Marburg (Vordiplom) |
| 2001 - 2003 | Studium der Physik an der Universität Karlsruhe (TH) (Vordiplom) |
| 2003 - 2006 | Studium der Physik an der Philipps-Universität Marburg (Diplom) |
| seit 2006 | Promotion an der Philipps-Universität Marburg, Fachbereich Physik, AG Experimentelle Halbleiterphysik bei Prof. Dr. W.W. Rühle |

# Acknowledgements

First and foremost I am eternally grateful to Prof. Dr. W.W. Rühle who gave me the opportunity to work in his group. I am deeply indebted to my supervisor Sangam Chatterjee. Without his continued support and energy it would have been so much harder and much less fun.

It has been my great pleasure to work with my colleagues. We had some good times, and helped each other when things just did not want to work. I will always fondly remember the heated discussions we had not only about science, but life itself.

A special thank you goes out to my students. Teaching is hard, but your questions always make me smarter.

The support I received from Tiago Buckup from the group of Prof. Dr. Motzkus deserves a special mention. He always had an answer or a tip for the rookie, who sometimes doubted that his pulse shaper actually works as intended.

The fascinating field of shift and rectification currents were brought to our attention by our collaborator Mark Bieler from the PTB in Braunschweig. I still think we deserved that paper.

For an experimental physicist the availability of the mechanical and electronics facilities on-site often proved to be life-savers. A special salute goes out to Rüdiger Rink, who always had a tip for the inclined handyman and his two left hands.

My parents always cared very much about my education and well being. It is only because of them, that I continuously find the determination to finish what I started. I must not forget to mention my brother Karun, life would be so much more boring without him.

And last but not least I need to thank Sonja, who endured my many moods. She is my constant. Now that we are about to complete this adventure, what’s next?

*...so long and thanks for all the gummy bears.*